ELECTRON BACKSCATTER DIFFRACTION OF GOLD NANOPARTICLES

ELECTRON BACKSCATTER DIFFRACTION OF GOLD NANOPARTICLES

By SYEDA RIDA ZAINAB, B. Eng.

A Thesis Submitted to the School of Graduate Studies in Partial Fulfilment of the Requirements for the Degree Master of Applied Science

McMaster University MASTER OF APPLIED SCIENCE (2015) Hamilton, Ontario

(Engineering Physics)

TITLE: Electron Backscatter Diffraction of Gold Nanoparticles

AUTHOR: Syeda Rida Zainab, B.Eng. (McMaster University)

SUPERVISOR: Dr. John S. Preston

Abstract

Electron Backscatter Diffraction (EBSD) is a well-developed technique used to perform quantitative microstructure analysis in the Scanning Electron Microscope (SEM); however, it has not been widely applied towards studying nanostructures. This work focuses on the use and limitations of EBSD in the characterization of Au nanoparticles on an $MgAl_2O_4$ substrate. Samples under investigation are prepared by depositing a thin film of Au on an $MgAl_2O_4$ substrate, and then finally heated in a furnace to induce dewetting and cluster formation.

The challenges of obtaining crystallographic information from nanoparticles using EBSD are qualitatively and quantitatively described through an evaluation of the quality of the diffraction pattern at various locations of the primary electron beam on the nanoparticle. It is determined that for a high quality Electron Backscatter Diffraction Pattern (EBSP), the production of diffracted backscattered electrons travelling towards the detector must be high and the depth of the source point must be low. The top of the nanoparticle, where the local geometry of the system is similar to the geometry of a macroscopically flat sample, is found to produce diffraction patterns of the highest quality. On the other hand, reversed-contrast EBSPs are observed when the beam is positioned near the bottom of the nanoparticle.

In addition, crystallographic information for each individual nanoparticle is gathered using EBSD. Each individual AuNP is observed to be single crystalline. Finally, the complete ensemble of crystalline orientations for individual nanoparticles is then compared to the global averaged crystallinity of the sample, as measured by X-ray diffraction. These results show that EBSD promises to be a powerful and robust technique in the characterization of nanoparticles.

Acknowledgements

Interdependence is at the core of life. No piece of work truly belongs to one individual as it is through the collaboration and unification of many that any work of significance can be produced. It is a gift of life to be so interconnected and interwoven into existence itself. The reason why I was able to accomplish this or make any meaningful contribution at all to this field was due to my support system, both at work and at home. I would like to sincerely thank each and every one who made this work possible.

First of all, I am grateful to my supervisor, Dr. John S. Preston for not only providing me this opportunity, but also for his constant encouragement, motivation and feedback. He gave me the independence and freedom with my work while also giving me direction by pushing me to try certain experiments and always asking questions that I thought I could answer but could not. He found time in his very busy schedule to accommodate me and reminded me the significance of this research whenever needed. I have learned a lot from this experience and it has been a pleasure working under his supervision. I would also like to express my gratitude to Dr. Ayse Turak and Dr. Kathryn Grandfield for providing me with feedback and for serving on my defense committee. I truly appreciate all the kind words and encouragement.

I am also thankful to my team members Dr. Kristoffer Meinander, who I could always rely on for expert opinion and excellent ideas. Additionally, Dr. Gabriel Devenyi, Fatemeh Rezapoor and Pouya Hosseini for their helpful discussions and ideas throughout this work. Tahereh Majdi for training me thoroughly with sample preparation and especially for allowing me to use her reliable samples that were prepared with absolute perfection. Franklyn D'Souza for always being there to bounce off ideas and giving me sound advice regarding software and analysis.

The staff of the Canadian Center for Electron Microscopy (CCEM), especially Dr. Glynis de Silveira for her encouragement when I needed it the most and reminding me the significance of this research. Also, Mr. Chris Butcher for not only training me but also for providing assistance with the instruments and giving me extra time in the evenings. Ms. Marilyn Marlow, at the Engineering Physics department, for her kind and welcoming attitude when answering all my administrative questions. Ms. Milica Zubic for her hard work in providing me with a clean office.

The National Science and Engineering Research Council of Canada Collaborative Research and Training Experience Program in Photovoltaics for funding this work.

Finally, I am forever grateful to my family. I have the strongest and most cohesive support system at home. They truly believe in me and provided me with the right environment, taking care of all other aspects in my life, so that I could focus on my research.

Unaiza Naeem Qureshi, thank you for not only providing insightful feedback and being with me every step of the way but also for encouraging me to pursue research in the first place. You embody 'nothing is impossible' and have pushed me to pursue things against all odds. Thank you for being strong in all the areas in which I am weak. Simply put, this work would not have been possible without your endless support in all aspects of my life. As a friend, you are the absolute best.

My sisters, Ezza Ali, Eisha Ikhtiar, and Huda Syeda, for taking care of me all the times when mom was not around, cooking me delicious dinners, and filling her shoes perfectly. My very accomplished and proud dad, Ali Hussnain Sajid, for all his hard work and sacrifices in bringing me where I am today and providing me with this platform. From him, I have learned to be honest, straightforward, and hardworking, thus, I thank you for being my role model. Finally, my deepest gratitude is for my mom, Zille Huma Ali, who has taken the absolute best care of me. From making a customized breakfast for me every morning, forcing me to carry lunch every day, to making my favourite dinners. Thank you for keeping me grounded, honest, and true in all aspects of life and for being one of my biggest believers.

One needs certain settings, certain conditions, and stability in life to be able to pursue research. And it is my family, my family that embodies interdependence, who has given me all that.

CONTENTS

LIST OF FIGURES

LIST OF TABLES

1. INTRODUCTION

1.1 Overview

With the numerous current applications of nanostructures and the many potential applications in future electronic devices, it is essential to continue to explore the different methods of studying and characterizing nanostructures. For instance, information about the crystal structure of nanostructures will lead to a better understanding of growth mechanisms and properties of materials. Currently, X-ray Diffraction (XRD) [**1**,**2**,**3**,**4**,**5**] and electron diffraction in Transmission Electron Microscopy (TEM) [**3**,**4**,**5**,**6**,**7**,**8**,**9**] are primarily used for studying the crystal structure of nanostructures. However, Electron Backscatter Diffraction (EBSD) has not yet been used in this field. EBSD has a spatial resolution in the range of tens of nanometers [**10**,**11**], which allows analysis of each nanoparticle individually, unlike XRD, which gives the average crystal orientation of the whole sample. TEM, on the other hand, is costly and requires complicated steps for sample preparation [**12**], whereas sample preparation for EBSD is simple [**10**]. So far there have only been two studies reported by Small et al. [**13**,**14**] that have explored the opportunity of using EBSD on nanostructures.

An EBSD system is installed in a Scanning Electron Microscope (SEM). Under vacuum, the primary electron beam is focused on the sample, which is typically placed at an optimal 70^{o} tilt from the horizontal. Electrons of the incident beam may backscatter out of the surface but in the length of the path that the backscattered electrons (BSEs) travel from the primary scattering event to the sample surface, some electrons that are incident on atomic planes satisfy the Bragg diffraction condition. These electrons are channelled differently and produce a variation in intensity which forms a diffraction pattern representing the crystal structure of the excited volume. An EBSD detector consists of a phosphor screen coupled with a charge-coupled device (CCD) camera and placed parallel to the primary beam, facing the point of impact between the beam and the sample [**10**]. When the high energy BSEs strike the phosphor screen of the camera, fluorescence takes place and the image on the screen is captured by the CCD camera.

The pattern created by the diffraction of backscattered electrons is known as the Electron Backscatter Diffraction Pattern (EBSP).

Since EBSD is a near-surface technique, the samples studied through EBSD need to be flat and the tilt angle must be chosen to maximize the production of BSEs while maintaining an acceptable spatial resolution [**10**]. The samples are required to be flat to ensure that a high number of diffracted backscattered electrons reach the detector and produce a high quality EBSP. This is the reason why nanostructures have not been studied through EBSD. The local geometry between the beam and the sample cannot be kept at the optimal 70^{o} tilt due to the varying shapes of nanostructures. Thus this research explores the opportunities and limitations of using EBSD in the analysis of nanostructures. The work is focused on analyzing gold nanoparticles (AuNPs) on spinel ($MgAl_2O_4$) through EBSD.

Gold nanoparticles have applications in many fields, one of which includes providing nucleation sites for the growth of nanowires [**2**,**15**].Nanowires are most commonly grown using the vapour–liquid–solid (VLS) process [**2**], which was first proposed in 1964 by Wagner and Ellis [**16**]. In the VLS mechanism, AuNPs provide a preferential site for the absorption of a vapour which then precipitates out into a 1D nanowire [**3**]. VLS is one of the most common applications of AuNPs and thus determining methods of producing and characterizing AuNPs may, for example, lead to greater control over this process. Other reasons which make AuNPs an appropriate candidate to be studied through EBSD will also become apparent through this work. Rest of Chapter 1 will primarily focus on the diffraction theory required to understand the mechanisms of EBSD. The equipment and methodologies used in this research are discussed in detail in Chapter 2. First part of Chapter 3 explores how EBSD can be in used with AuNPs while the second part focuses on studying multiple AuNP samples and comparing them to results from 2D X-ray Diffraction (2DXRD) analysis. Finally, a summary along with the purposed future work are presented in Chapter 4.

1.2 Theory of Electron Backscatter Diffraction

EBSD is the diffraction of backscattered electrons from a sample in the SEM. The following sections will describe the theoretical aspects of this technique. Although the source of the signal

consists of backscattered electrons, most of the focus will be on the diffraction process since it is the diffraction of these electrons which results in the most interesting aspects of EBSD.

1.2.1 Backscattered Electrons

Backscattered electrons are electrons from the primary beam that escape from the surface after being elastically scattered by the strong electric field of the specimen's nuclei. Even though the most probable scattering angle is small, large changes in direction can occur through multiple scattering events where some primary electrons can turn around and leave the specimen from the surface as backscattered electrons. The fraction of electrons that backscatter and escape the surface is quantified through the backscattering coefficient η [**10**]:

$$\eta = \frac{n_{BSE}}{n_B} = \frac{Number\ of\ backscattered\ electrons}{Total\ number\ of\ incident\ beam\ electrons} \tag{1.1}$$

The backscattering coefficient depends on the material and the angle to the surface at which the beam interacts with the surface of the specimen. For more details on the parameters that effect η and how it is obtained, refer to [**17**].

1.2.2 Diffraction

Diffraction is a wave interference phenomenon. The discussion on diffraction begins by first understanding models that describe X-ray diffraction, followed by electron diffraction in Transmission Electron Microscope (TEM), which then finally leads to the description of the diffraction process in EBSD. X-rays interact weakly with the substrate, unlike electrons, so the X-ray diffraction process is much simpler to understand.

Historically, X-ray diffraction has been used primarily to study crystal structure of materials. Roentgen discovered X-rays in 1895 [**12**], however, the nature of X-rays remained unknown. It was the work of Max von Laue in 1912 [**18**,**19**] and of Bragg and Bragg in 1914 [**20**] that not only confirmed that X-rays were a form of electromagnetic radiation, but also that diffraction of X-rays could be used to study crystal structures. X-ray crystallography remains the most widely

used technique for the investigation of molecular structure [**12**]. X-ray diffraction is thus very well understood. Comparatively, electron diffraction is not as developed nor has it been as widely used as X-rays. Louis de Broglie initiated theoretical work on the wave-like characteristic of electrons in 1925 [**12**]. Since wave interference concepts are similar for X-rays and electrons, theories of electron diffraction in TEM have used the concepts developed in X-ray diffraction. TEMs were first commercialized in 1936, four years after Knoll and Ruska proposed the idea of electron microscopes in 1932 [**12**]. The technique was later improved in the mid-1950s by Hirsch and his colleagues which allowed TEM to be used to study material in more details. Theories on electron diffraction were developed in this time also and have been summarized by Hirsch in 1977 [**21**].

EBSD has been developed relatively recently and was first commercially available in 1986 [**12**]. Explanations of diffraction processes taking place in EBSD have utilized the earlier theories developed for TEM [**10**] and the modified theories of Electron Channelling Pattern (ECP) [**22**]. Thus, the discussion on diffraction in EBSD will begin with first the understanding of X-ray diffraction. Next electron diffraction is studied and the formulations developed for TEM are presented. Finally, this discussion will lead to the description of the physical processes and formation of Electron Backscatter Diffraction Patterns (EBSPs).

1.3 Kinematical Theory of Diffraction

The discussion will begin with the simplest formulations describing the wave interference phenomenon. According to wave theory, waves will interfere constructively when they are in phase as the amplitudes of the waves will add. On the other hand, destructive interference will occur when the waves are out of phase and cancel one another. The kinematical theory of diffraction is the simplest approach to describing this phenomenon in crystals and applies to both X-ray waves and electron wavefunctions. Bragg's law and Laue conditions are both based on this theory.

1.3.1 Bragg's Law

The simplest approach used to describe diffraction is through the Bragg's law proposed by Sir William H. Bragg and his son W. Lawrence Bragg [**20**]. In this approach, atomic planes act as reflectors and the incident plane waves scatter by reflecting off these atomic planes, as shown in Figure 1.1.

For the scattered plane wave (also referred to as reflected plane wave) to remain in phase with the incident plane wave, waves reflecting from adjacent planes must have a path difference of an integral number of wavelengths. From Figure 1.1, it can be seen that the path difference between two adjoining planes $AB + BC$ is equal to $2d \sin\theta_B$. Thus mathematically, Bragg's law can be stated as:

$$n\lambda = 2d \sin\theta_B \tag{1.2}$$

Here n is any integer while λ describes the wavelength of the incident plane wave, d is the spacing between the atomic planes (or reflectors) and finally θ_B is the Bragg angle at which constructive interference takes place. Another completely different approach that leads to the same results is known as the Laue condition.

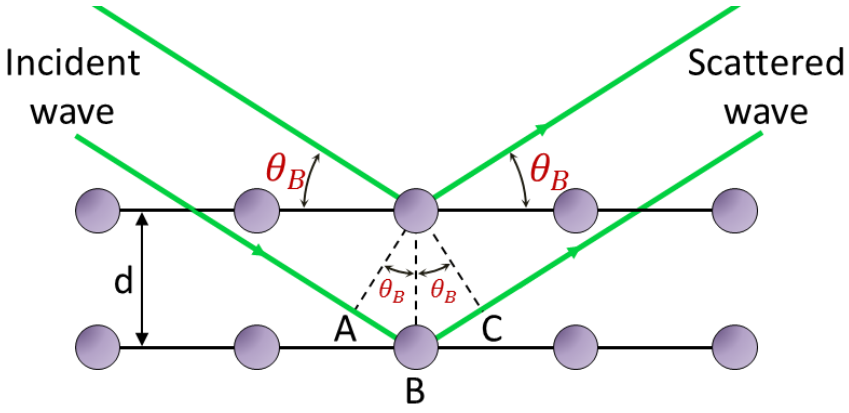

Figure 1.1: Incident wave at $\boldsymbol{\theta_B}$ is scattered at the same angle from a set of atomic planes separated by a distance $\boldsymbol{d}$. The path difference between the two waves is $\boldsymbol{AB + BC}$.

1.3.2 Laue's Conditions

The use of diffraction to study the atomic structure of materials has been credited to von Laue (1913) [**12**]. Laue used the light-optics approach to describe X-ray diffraction. In this formulation, Laue considered scattering of waves by the individual unit cells arranged in a period array. Within the crystal, scatterers placed at the lattice site reradiate the incident radiation in all directions. Diffraction peaks occur when the rays scattered from all the lattice points interfere constructively [**12**]. In Figure 1.2, a plane wave of wavelength λ with wavevector $\boldsymbol{k}$ is incident at an angle θ on scatterers A and B, separated by a distance r. The path difference of the incident wave $\boldsymbol{k}$ and scattered wave $\boldsymbol{k}'$ is given by $\boldsymbol{r} \cdot (\hat{\boldsymbol{u}}' - \hat{\boldsymbol{u}})$.

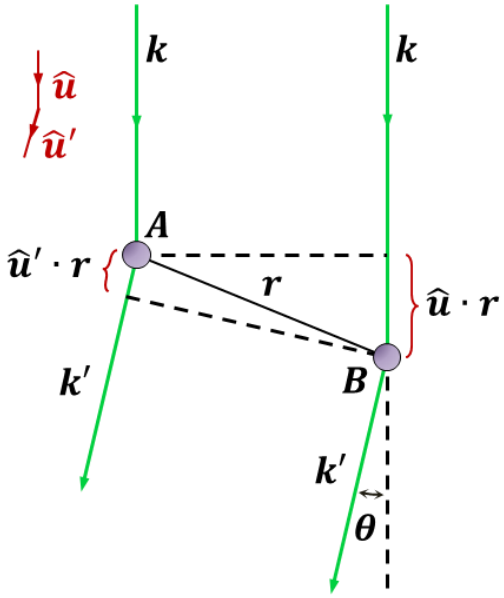

Figure 1.2: Schematic showing the scattering of an incident plane wave k by two atoms with a distance r through angle θ into the plane wave k'. The top left schematic shows unit vectors in the direction of the incident and scattered plane waves. Adapted from [**17**].

For constructive interference to occur, the path difference must be some integral multiple of wavelength.

$$\boldsymbol{r} \cdot (\hat{\boldsymbol{u}}' - \hat{\boldsymbol{u}}) = m\lambda \tag{1.3}$$

This is the first Laue equation, where m is an integer. Wavevectors $\boldsymbol{k} = \frac{1}{\lambda}\hat{u}$ and $\boldsymbol{k}' = \frac{1}{\lambda}\hat{u}'$ allow the above to be rewritten as:

$$\boldsymbol{r} \cdot (\boldsymbol{k}' - \boldsymbol{k}) = m \tag{1.4}$$

This condition can also be written as:

$$e^{2\pi i(\boldsymbol{k}\prime - \boldsymbol{k})\cdot \boldsymbol{r}} = \mathbf{1} \tag{1.5}$$

Let the scattering vector $\Delta\boldsymbol{k} \equiv \boldsymbol{k}' - \boldsymbol{k}$. Lattice vector $\boldsymbol{r}_g$ can be defined as the origin of the unit cell according to the primitive vectors of the crystal lattice $\boldsymbol{a}$, $\boldsymbol{b}$, and $\boldsymbol{c}$ [**17**]:

$$\boldsymbol{r}_g = m\boldsymbol{a} + n\boldsymbol{b} + o\boldsymbol{c} \tag{1.6}$$

where m, n, and o are integers. Similarly reciprocal lattice vector $\boldsymbol{g}_{hkl}$ can be defined according to unit cell translations in reciprocal space $\boldsymbol{a}^*$, $\boldsymbol{b}^*$, and $\boldsymbol{c}^*$.

$$\boldsymbol{g}_{hkl} = h\boldsymbol{a}^* + k\boldsymbol{b}^* + l\boldsymbol{c}^* \tag{1.7}$$

where h, k, and l are integers, or the reciprocal lattice indices and define the plane (hkl). From Equation (1.5), it can be seen that for constructive interference, the scattering vector $\Delta\boldsymbol{k}$ must be a reciprocal space vector $\boldsymbol{g}$, that is $\Delta\boldsymbol{k} = \boldsymbol{g}$. This is the condition for Laue diffraction. In addition, knowing that $\boldsymbol{g} \cdot \boldsymbol{r}_g = N$, where N is an integer, the Laue condition can be described as:

$$\Delta\boldsymbol{k} \cdot \boldsymbol{r}_g = N \tag{1.8}$$

From this, Laue equations for a three-dimensional distribution of atoms can be written as:

$$\Delta\boldsymbol{k} \cdot \boldsymbol{a} = h \tag{1.9}$$

$$\Delta\boldsymbol{k} \cdot \boldsymbol{b} = k \tag{1.10}$$

$$\Delta\boldsymbol{k} \cdot \boldsymbol{c} = l \tag{1.11}$$

When all three Laue equations are satisfied simultaneously a diffracted beam is produced.

1.3.3 Equivalence of Bragg and Laue

Laue equations describe the physical process of diffraction taking place inside a crystal, Bragg's law, on the other hand, does not correspond to the actual situation. Instead it is useful in

producing a physical picture of the constructive interference phenomena because the diffracting planes appear to behave as reflectors for the incident beam. To justify the use of Bragg's law, here a simplified proof will be presented to show that it can be derived from the Laue equations.

From Figure 1.3, it can be seen that:

$$|\Delta \boldsymbol{k}| = \frac{2 \sin \theta_B}{\lambda} \tag{1.12}$$

Also, it can be recognized that the magnitude of reciprocal space vector is given by:

$$|\boldsymbol{g}| = \frac{1}{d_{hkl}} \tag{1.13}$$

For diffraction to occur, as mentioned earlier, $\Delta \boldsymbol{k} = \boldsymbol{g}$. Thus Bragg's law can be deduced from this:

$$\frac{2 \sin \theta_B}{\lambda} = \frac{1}{d_{hkl}} \tag{1.14}$$

$$2 d_{hkl} \sin \theta_B = \lambda \tag{1.15}$$

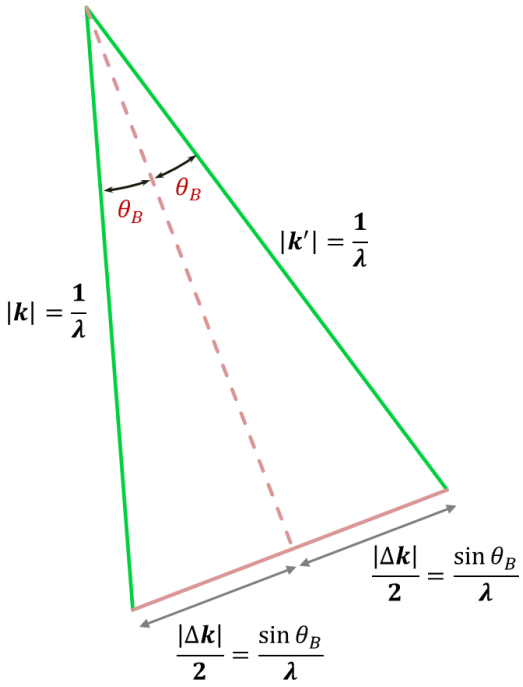

Figure 1.3: Schematic showing the geometrical relationship between the incident wave k, the Bragg diffracted wave k' and the scattering vector Δk, modified from [**12**].

1.3.4 Kinematical Theory of Diffraction

From Bragg and Laue equations, it was concluded that the diffracted waves interfere constructively when $\Delta \boldsymbol{k} = \boldsymbol{g}$, which is commonly known as the Bragg condition. Bragg's law or the Laue conditions explained here are based on the kinematical theory of diffraction.

The general kinematical theory will be presented here which is valid as long as the first Born approximation is valid [**23**]. To summarize the approximation, it assumes that the incident wave is only scattered once by the material. Thus it is valid as long as this criterion is met, that is either the scattering is weak or the material is very thin.

In this theory, the incident electron wavevector $\boldsymbol{k}$ with direction $\hat{\boldsymbol{u}}$ is elastically scattered by the atoms through an angle θ with scattering amplitude $f(\theta)$ (for details on $f(\theta)$, refer to [**17**,**23**]) into a direction $\hat{\boldsymbol{u}}'$ with wavevector $\boldsymbol{k}'$. Since this is an elastic process, the magnitude of the wavevectors remains the same, that is $|\boldsymbol{k}| = |\boldsymbol{k}'| = 1/\lambda$. With atoms separated by a distance $\boldsymbol{r}$, as shown in Figure 1.2, the scattered waves will have a path difference of $\Delta = (\hat{\boldsymbol{u}}' - \hat{\boldsymbol{u}}) \cdot \boldsymbol{r}$ resulting in a phase shift φ such that:

$$\varphi = \frac{2\pi}{\lambda}\Delta = \frac{2\pi}{\lambda}(\hat{\boldsymbol{u}}' - \hat{\boldsymbol{u}}) \cdot \boldsymbol{r} = 2\pi(\boldsymbol{k}' - \boldsymbol{k}) \cdot \boldsymbol{r} \tag{1.16}$$

The amplitude of a beam scattered by a unit cell is given by [**17**]:

$$\psi_{cell} = \psi_{0_{cell}} \sum_{k} f_k(\theta) e^{2\pi i(\boldsymbol{k}\prime - \boldsymbol{k}) \cdot (\boldsymbol{r}_k)} \tag{1.17}$$

where ψ_0 is the amplitude of the incident wave and $\boldsymbol{r}_k$ defines the position of each atom $(k = 1, \dots, n)$ in the unit cell [**24**]. To determine the wave amplitude in the direction $\boldsymbol{k}'$, sum over all the unit cells in the sample, with the assumption that the crystal forms a parallelepiped with $N = N_1 N_2 N_3$ unit cells [**17**]:

$$\psi = \psi_0 \sum_{m=1}^{N_1} \sum_{n=1}^{N_2} \sum_{o=1}^{N_3} \sum_{k=1}^{n} f_k(\theta) e^{2\pi i(\boldsymbol{k}\prime - \boldsymbol{k}) \cdot (\boldsymbol{r}_g + \boldsymbol{r}_k)} \tag{1.18}$$

where $\boldsymbol{r}_g$ was defined earlier in Equation (1.6) as the origin of the unit cell and $f_k(\theta)$ represents the elastic scattering amplitude of the *k*th atom at the position $(\boldsymbol{r}_g + \boldsymbol{r}_k)$. Setting the amplitude of the incident wave $\psi_0 = 1$, the summation can be rewritten as:

$$\psi = \sum_{k=1}^{n} f_k(\theta) e^{2\pi i(\boldsymbol{k\prime}-\boldsymbol{k})\cdot(\boldsymbol{r}_k)} \times \sum_{m=1}^{N_1}\sum_{n=1}^{N_2}\sum_{o=1}^{N_3} e^{2\pi i(\boldsymbol{k\prime}-\boldsymbol{k})\cdot(\boldsymbol{r}_g)} = F \times G \tag{1.19}$$

The two terms here represent the structure amplitude *F* and the lattice amplitude *G* [**17**]. While the structure amplitude depends on the type of the atom ($f_k(\theta)$) and the position of the atom ($\boldsymbol{r}_k$) inside the unit cell, the lattice amplitude, on the other hand, depends only on the shape of the crystal as it is a summation over all unit cells ($\boldsymbol{r}_g$) [**24**]. The waves will interfere constructively if the arguments in the exponential terms of the lattice amplitude are all integer multiples of 2π so that the amplitudes will sum [**17**]. This produces the same Laue conditions discussed in Section 1.3.2 [**17**].

The initial discussion on Bragg and Laue has been limited to only explaining the basic geometry (and not the intensities) of diffraction and is true only for a perfect, infinite crystal in which no inelastic scattering takes place. For a perfect, finite crystal, deviations from the Bragg condition will result in non-zero intensities due to partially destructive interference. This is the reason why the kinematical theory of diffraction is discussed in more detail here.

An excitation error $\boldsymbol{s}$ needs to be introduced to demonstrate how the intensity varies. It is a reciprocal space vector that measures the deviation from the exact Bragg condition, such that $\Delta\boldsymbol{k} = \boldsymbol{k}' - \boldsymbol{k} = \boldsymbol{g} + \boldsymbol{s}$, where $\boldsymbol{s} = 0$ corresponds to the exact Bragg condition. For a single crystal film, where only two beams are considered: the direct beam and the diffracted beam, the intensity of the Bragg diffracted spot can be expressed as [**23**,**25**]:

$$I_g = \left(\frac{\pi t}{\xi_g}\right)^2 \frac{\sin^2(\pi t s)}{(\pi t s)^2} \tag{1.20}$$

where I_g is the kinematical intensity of the Bragg diffraction spot, t is the thickness of a single crystal film, s is excitation error, and $\xi_g \equiv \frac{\pi V}{\lambda F_g}$ is a characteristic length called the excitation

distance defined in [**12**,**17**]. Refer to [**17**] for exact details on the derivation of the intensity. This expression is presented here to show that intensity oscillates with thickness t, for $s \neq 0$. It is now important to discuss the differences between X-rays and electrons and demonstrate how the kinematical theory breaks down.

1.3.5 Electron Interactions vs. X-ray Interactions

Just like X-rays, electrons diffract from a set of planes in the crystalline material resulting in constructive and destructive interference. Since electrons are charged particles, they interact much more strongly with matter. These incoming negatively charged particles are scattered by both the electrons and the nuclei of the material [**12**]. Even though the scattering mechanisms are very different, the theory developed earlier for X-rays can also be applied similarly to electron diffraction, as it is a purely geometrical construct [**12**]. In fact, in TEM, for a thin sample, the diffraction of electrons can be described in the exact method described above.

Since the kinematical theory of diffraction assumes that the incident beam is scattered only once by the material, it is valid if the incident wave is scattered weakly by the material or if the material is thin. Since X-rays are weakly scattered, this approximation is highly valid for X-ray diffraction and can readily be used quantitatively. It is also valid for electron diffraction in very thin crystals where the path of electrons is too short for multiple scattering (Refer to [**23**] for details on the range of thicknesses).

Given the fact that electrons and atoms have strong Coulomb interactions, kinematical theory is often only qualitative. This is because, generally, an electron beam that has been Bragg diffracted once by a plane of atoms is in an ideal orientation to be diffracted again by the same set of planes [**12**]. Since the beam can be diffracted again and again, this is termed dynamical diffraction. The probability of a beam diffracting again and again increases as the thickness of the specimen increases. Thus in a TEM, as the thickness increases, the kinematical theory can no longer predict the results of a diffraction pattern. The geometry of the pattern can still be described from the kinematical theory, however, the intensities cannot. Instead, the dynamical theory of diffraction is used. It is also because of this that the intensities from electron

diffraction experiments cannot be analysed as easily as the intensities from X-ray diffraction [**12**].

1.3.6 Breakdown of Kinematical Theory of Diffraction

Kinematical approximation is valid as long as the intensity of the diffracted beam is much less than the intensity of the incident beam, that is $I_g \ll I_0$. Consequently, it breaks down for thicker samples as the probability of multiple scattering increases. It is evident from Equation (1.20) that at the exact Bragg position when $s = 0$, $I_g \propto t^2$. As thickness increases, I_g approaches I_0 and kinematical theory is no longer valid.

Clearly a theory which considers multiple scattering within the specimen and the dynamical interaction between the scattered waves must be developed [**21**]. In fact, just as Bragg's and Laue's equations cannot incorporate factors such as the deviation parameter s, it was imperative to consider the more general kinematical theory of diffraction. Similarly, there are some physical processes such as absorption that cannot be included in the kinematical theory, and thus an improved theory, the dynamical theory of diffraction, needs to be formulated.

1.4 Dynamical Theory of Diffraction

Although kinematical theory is a valid approximation for the geometry of diffraction patterns, it generally provides an invalid description of intensities from diffraction of electrons. For EBSD, purely geometrical relations can easily be obtained from Bragg's law [**10**]; however, a complete model of the physical processes that describes the observed geometry and intensities is the dynamical theory of diffraction, which accounts for the multiple elastic and inelastic scattering of the electron beam.

Multiple methods have been proposed for the formulation of the dynamical theory of electron diffraction (refer to [**12**,**23**,**26**] for details). The approach that is described here is the one that was initially proposed by Bethe [**27**] since calculations from this method simulate the observed EBSD patterns very closely [**28**]. These methods were initially used to quantitatively describe

electron diffraction in TEM [**26**], however, later it will be shown how this framework can also be applied towards describing Kikuchi patterns in EBSD [**10**,**28**].

1.4.1 Bloch-wave Formulation

To begin, a wave equation that describes the behaviour of an electron inside a crystal is required. To derive this, it needs to be determined how an incident plane wave that satisfies the boundary condition at interface will be transformed into a wave-field $\Psi(\boldsymbol{r})$ having the same periodicity as the crystal [**17**]. Bethe's approach of obtaining this is to use the Schrodinger's equation with the wavefunction $\Psi(\boldsymbol{r})$ modulated according to Bloch's theorem [**29**]. Schrodinger's equation for an electron with wavefunction $\Psi(\boldsymbol{r})$ within the real crystal potential $V(\boldsymbol{r})$ is:

$$\nabla^2\Psi(\boldsymbol{r}) + \frac{8\pi^2 m|e|}{h^2}[E + V(\boldsymbol{r})]\Psi(\boldsymbol{r}) = 0 \tag{1.21}$$

where m is the relativistic mass of an electron, e is elementary charge of electron, h is plank's constant, E is accelerating potential of the incident electron, and $V(\boldsymbol{r})$ is the real crystal potential. The crystal potential is positive as the incident electrons are attracted to the atoms. Given that the crystal potential $V(\boldsymbol{r})$ follows the same periodicity as the crystal, it can be expanded as a Fourier series over all lattice points $\boldsymbol{h}$:

$$V(\boldsymbol{r}) = \sum_{-\infty}^{\infty} V_h e^{2\pi i\, \boldsymbol{h}\cdot\boldsymbol{r}} \tag{1.22}$$

The Fourier coefficients are given by $V_h = F_h/\Omega$, where F_h is the structure amplitude (defined in section 1.3.4) and Ω is the volume of the unit cell [**26**].

The Bloch wave method can be used to directly solve the time-independent Schrödinger equation. The wavefunction must have the same periodicity as the crystal, thus it may be represented as a linear superposition of Bloch waves $\psi^{(j)}$ with excitation amplitudes $\epsilon^{(j)}$ [**17**]:

$$\Psi(\boldsymbol{r}) = \sum_j \epsilon^{(j)}\psi^{(j)}(\boldsymbol{r}) \tag{1.23}$$

$$\Psi(\boldsymbol{r}) = \sum_j \epsilon^{(j)} \sum_g C_g^{(j)} \, e^{2\pi i \, (\boldsymbol{k}^{(j)} + \boldsymbol{g}) \cdot \boldsymbol{r}} \cdot e^{-2\pi \, \boldsymbol{q}^{(j)} \cdot \boldsymbol{r}} \tag{1.24}$$

where $C_g^{(j)}$ is the Bloch wave coefficient of the *j*th Bloch wave and represents the amplitude of the plane waves with wavevectors $\boldsymbol{k}^{(j)} + \boldsymbol{g}$. The last exponential term in Equation (1.24) is a damping term with the absorption term $\boldsymbol{q}^{(j)}$ representing the exponential dampening of the wave amplitudes [**17**]. Thus each Bloch wave is exponentially attenuated as it propagates through the crystal, as physically expected [**25**]. For now the crystal is assumed to be non-absorbing and this term will be dropped. Summing over indices j and g describes a sum over an infinite number of reciprocal lattice points, however, in practice, only a limited number *n* of strongly excited beams (*n*-beams) will be taken into account [**17**].

To collect the constants, two new quantities can be defined [**17**]. First is the modified potential $U(\boldsymbol{r})$, whose Fourier coefficients are related to the Fourier coefficients of the crystal potential such that:

$$U_h = \frac{2m|e|}{h^2} V_h \tag{1.25}$$

The second quantity K is the magnitude of the mean electron wavevector inside the crystal corrected for the mean crystal potential:

$$\boldsymbol{K}^2 = \frac{2m|e|}{h^2}(E + V_0) \tag{1.26}$$

Once the periodic potential in Equation (1.22), the Bloch wavefunction $\Psi(\boldsymbol{r})$ from Equation (1.24) (neglecting the last absorption term), and the two quantities defined above in Equations (1.25) and (1.26), are substituted into the Schrödinger's Equation (1.19), result is the following expression [**17**]:

$$\sum_g \left\{ \left[\boldsymbol{K}^2 - \left(\boldsymbol{k}^{(j)} + \boldsymbol{g} \right)^2 \right] C_g^{(j)} + \sum_{h \neq g} U_{g-h} C_h^{(j)} \right\} e^{2\pi i \, (\boldsymbol{k}^{(j)} + \boldsymbol{g}) \cdot \boldsymbol{r}} = 0 \tag{1.27}$$

Since the coefficient of the exponential must equal zero, this leads to the set of fundamental equations of dynamical theory:

$$\left[\boldsymbol{K}^2 - \left(\boldsymbol{k}^{(j)} + \boldsymbol{g}\right)^2\right] C_g^{(j)} + \sum_{h \neq g} U_{g-h} C_h^{(j)} = 0 \tag{1.28}$$

For every reflection $\boldsymbol{g}$, there will be one such equation [**25**]. This equation will produce an exact solution if an infinite number of $\boldsymbol{g}$ reflections are considered. Since only a finite number of reflections can be chosen practically, the outcome will be an approximate solution [**25**]. In the common two-beam approximation, two beams are considered leading to two dispersion equations and two Bloch wave solutions. Similarly, in the n-beam case, where n reflection (or beams) are considered, there will be n such equations, resulting in n number of electron wavevectors $\boldsymbol{k}^{(j)}$ corresponding to n different Bloch wave solutions.

Generally, to determine the solutions, $\boldsymbol{k}^{(j)}$can be rewritten as an eigenvalue problem for a set number of beams (*n*-beams), resulting in eigenvectors $C_g^{(j)}$. Excitation amplitudes $\epsilon^{(j)}$ are obtained from boundary conditions [**26**]. The details of how to set this as an eigenvalue problem can be found in [**24**,**30**]. Once these values are determined, the Bloch wavefunction in Equation (1.24), which describes the behaviour of an electron inside the crystal for a given direction $\boldsymbol{K}$ and accelerating potential E, is known. Therefore it can be used to determine the diffraction pattern on the detector, which is a sum of all the Bloch waves emanating from the sample [**30**].

1.4.2 Two-Beam Approximation and Anomalous Absorption

The first approximation of the dynamical theory is the two beam case where the wavefunction inside the crystal is described as a general sum of two Bloch waves. The two beams that are considered are the forward-scattered beam with wavevector $\boldsymbol{k}$ and the diffracted beam with wavevector $\boldsymbol{k} + \boldsymbol{g}$. Consider a simple cubic crystal structure where the origin of $\boldsymbol{r}$ at the center of symmetry is chosen to be an atomic site. Assume that the Bragg condition is satisfied exactly such that $s = 0$ and $|\boldsymbol{k}| = |\boldsymbol{k} + \boldsymbol{g}|$. The reciprocal space vector $\boldsymbol{g}$ is considered parallel to the tangential component of incident wavevector $\boldsymbol{k}$ and perpendicular to the depth $\boldsymbol{z}$. Due to these symmetrical conditions, equal amplitudes from the forward and diffracted beams contribute to the Bloch waves at the Bragg condition [**12**,**23**].

The two beam approximation can generally be used when Equation (1.24) can be terminated at the second term, such that [**25**]:

$$\psi^{(j)}\left(\boldsymbol{k}^{(j)},\boldsymbol{r}\right) = C_0 e^{2\pi i\, \boldsymbol{k}^{(j)}\cdot \boldsymbol{r}} + C_g e^{2\pi i\, (\boldsymbol{k}^{(j)}+\boldsymbol{g})\cdot \boldsymbol{r}} \tag{1.29}$$

Taking into consideration the conditions mentioned above, the dispersion relation in Equation (1.28) can be used to determine the coefficients (Refer to [**24**] for detailed derivations) and the two beams can be described by the following wavefunctions [**21**]:

$$\begin{aligned}\psi^{(1)}\left(\boldsymbol{k}^{(1)},\boldsymbol{r}\right) &= \frac{1}{\sqrt{2}}\left(e^{2\pi i\, \boldsymbol{k}^{(1)}\cdot \boldsymbol{r}} + e^{2\pi i\, (\boldsymbol{k}^{(1)}+\boldsymbol{g})\cdot \boldsymbol{r}}\right)\\ &= \sqrt{2}\cos(\pi \boldsymbol{g}\cdot\boldsymbol{r})\, e^{2\pi i\, (\boldsymbol{k}^{(1)}+\frac{1}{2}\boldsymbol{g})\cdot \boldsymbol{r}}\end{aligned} \tag{1.30}$$

$$\begin{aligned}\psi^{(2)}\left(\boldsymbol{k}^{(2)},\boldsymbol{r}\right) &= \frac{1}{\sqrt{2}}\left(e^{2\pi i\, \boldsymbol{k}^{(2)}\cdot \boldsymbol{r}} - e^{2\pi i\, (\boldsymbol{k}^{(2)}+\boldsymbol{g})\cdot \boldsymbol{r}}\right)\\ &= i\sqrt{2}\sin(\pi \boldsymbol{g}\cdot\boldsymbol{r})\, e^{2\pi i\, (\boldsymbol{k}^{(2)}+\frac{1}{2}\boldsymbol{g})\cdot \boldsymbol{r}}\end{aligned} \tag{1.31}$$

Thus the probability density of each Bloch wave can be described as [**17**]:

$$\left|\psi^{(1)}(\boldsymbol{r})\right|^2 \propto \cos^2(\pi \boldsymbol{g}\cdot\boldsymbol{r}) = \cos^2\left(\frac{\pi x}{d_{hkl}}\right) \tag{1.32}$$

$$\left|\psi^{(2)}(\boldsymbol{r})\right|^2 \propto \sin^2(\pi \boldsymbol{g}\cdot\boldsymbol{r}) = \sin^2\left(\frac{\pi x}{d_{hkl}}\right) \tag{1.33}$$

where x is a coordinate parallel to $\boldsymbol{g}$ and normal to $\boldsymbol{z}$. From this formulation, a schematic is constructed plotting the intensities $\left|\psi^{(1)}\right|^2$ and $\left|\psi^{(2)}\right|^2$ at the Bragg position of Bloch wave 1 and Bloch wave 2 respectively as a function of distance across atomic planes [**21**].

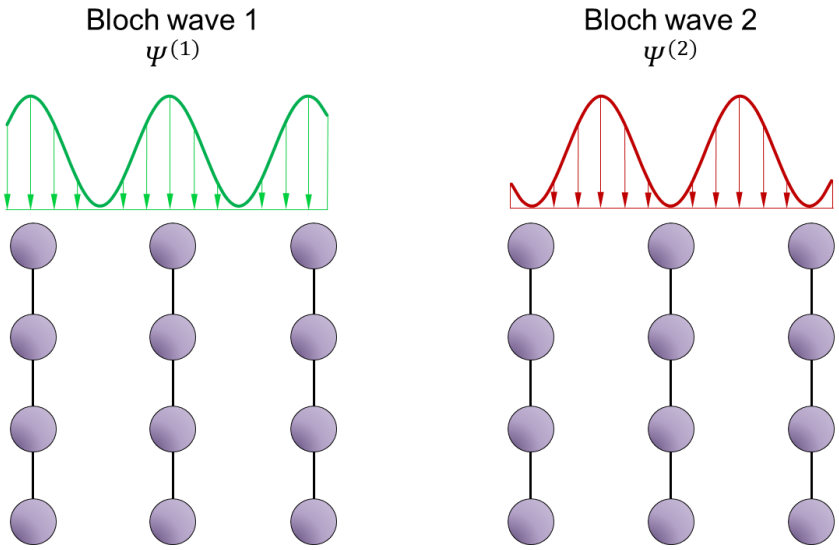

Figure 1.4: Probability densities of Bloch wave 1 and Block wave 2 at the Bragg condition. Maximum of Bloch wave 1 is at the ion cores while the maximum of Bloch wave 2 is concentrated between the ion cores.

A few conclusions on the properties of the two Bloch waves can be drawn from the two-beam dynamical theory with diffraction condition $s = 0$. The total energy and periodicity of the two Bloch waves are the same, as expected [**23**]. Both of the waves have a period of d_{hkl} but a phase shift of $d_{hkl}/2$ with respect to each other. At the lattice planes where x/d_{hkl} is an integer, the electron density is modulated such that Bloch wave 1 exhibits maxima while Bloch wave 2 is at its minima [**23**]. At the midpoint between the atomic planes, electron density in Bloch wave 1 is at its minima while Bloch wave 2 is now at its maxima. Since the electron density of Bloch wave 1 is highest at the ion cores, it has a lower potential energy, a higher kinetic energy, and a larger wavevector than Bloch wave 2 [**23**]. Also since it is concentrated near the atoms where there is a higher probability of a scattering event, it is reasonable to conclude that it will be scattered more than Bloch wave 2. Consequently, over the thickness of the crystal, Bloch wave 1 will also be absorbed (attenuated) more strongly than Bloch wave 2, whose electron density is highest in the interstitial regions between the ion cores and hence interacts weakly with the electrons in the crystal [**23**]. A phenomenological method of describing this effect is by the inclusion of the absorption parameter $\boldsymbol{q}^{(j)}$ in the damping exponential term [**17**], introduced in Equation (1.24). Details of this procedure are found in [**21**,**17**].

1.5 Electron Backscatter Diffraction Pattern

1.5.1 Formation of Kikuchi Lines

All the equations and theory developed thus far describe only coherent elastic scattering of electrons for a perfect non-absorbing crystal. This is the case for a thin sample of constant thickness in TEM. To summarize, the incident electron plane wave enters from the top of the sample and part of this wave is scattered coherently by all the atoms in the interaction volume. This implies that the waves from the scattering centers all have a perfectly known fixed phase relationship with respect to the incident beam and thus with respect to each other. Due to the wave-like behaviour of electrons, constructive and destructive interference will take place between the different scatterers. From Laue conditions it was determined that diffracted spots with some intensity I_g will be observed whenever $\Delta \boldsymbol{k} = \boldsymbol{g}$. The more complete dynamical theory of diffraction presented above takes into account multiple scattering and the dynamical coupling of the waves through the Bloch wave model; however, it is based on the assumption that the scattering event is coherent.

In reality however, not all the scattering will be coherent and some electrons will undergo random phase changes. For example, the incoming fast electrons are interacting with thermally vibrating atoms in a crystal. Due to thermal vibration, the atoms will be slightly displaced from their time-averaged site [**23**]. Although these electrons may be scattered elastically by the atoms, the random thermal displacements alters the phase relationship. This causes intensity of the Bragg diffracted spots to decrease and instead a continuous intensity is spread randomly in a broad range of k-space [**23**]. If this type of incoherent scattering took place, on average, homogeneously throughout the crystal, it would produce a continuous background [**10**]. This phenomenon becomes more apparent as the thickness of the sample increases due to a higher number of incoherent elastic and inelastic scattering events. Since incoherent scattering produces a diffuse background in the diffraction pattern [**23**], for thicker samples, the intensity distribution of the diffraction pattern will contain diffraction spots on a high continuous background. More interestingly, some of the incoherently scattered electrons may undergo Bragg diffraction, and thus cause the intensity of the diffuse background to be modulated. This

process produces sets of straight lines of higher or lower intensity on the diffraction pattern. These lines are known as Kikuchi lines named after Seishi Kikuchi who first observed them in 1928 [**31**]. Therefore coherent scattering, such as from thin samples in TEM, results in well-defined spots on the diffraction pattern, whereas thicker samples in TEM produce a diffraction pattern that consists of Bragg diffracted spots from coherent scattering and a modulated diffuse background from Bragg diffraction of incoherently scattered electrons.

This discussion finally leads to the formation of Kikuchi patterns in EBSD, which has the same geometry as the Kikuchi lines observed in TEM but a distinct intensity distribution. In the SEM, the primary electron beam is a plane wave that impinges on a crystalline sample from infinity. This beam diffracts and produces a modified distribution of incoming electrons, which will not be discussed further as it has minimal effects on the final EBSP [**30**]. Incoming electrons then interact with the atoms in the crystal and some will backscatter. This production of backscattered electrons is an incoherent process, that is, the scattered beam has lost its phase relationship with the incident beam as well as all other scattered beams. Inside the sample, there are now a large number of electrons travelling in all directions. This distribution of electrons is also known as diffusely scattered electrons. It can be assumed at this point that the atoms which cause the electrons to backscatter are a diverging source of electrons inside the crystal (discussed later, see Figure 1.5). These backscattered electrons arrive at the crystal planes from all directions. Since some will arrive at the Bragg angle to the planes, they will undergo diffraction as they propagate through the crystal and exit the specimen back from the surface. The diffraction pattern on the EBSD detector, which is a florescent screen monitoring the spatial distribution of scattered electrons, will be a continuous background from backscattered electrons that is modulated according to the atomic arrangement in the crystal due to diffraction. Spots are not observable as electrons scattering coherently with respect to the beam are negligible [**28**].

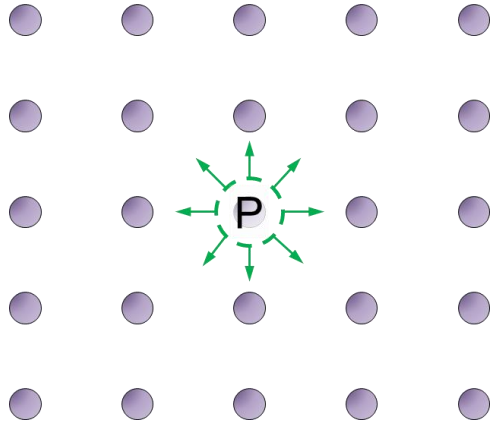

Figure 1.5: Atom which causes the electrons to backscatter is assumed to be diverging source point of electrons, labeled as P, adapted from [**28**]

As mentioned earlier, none of the equations or the theory formulated above takes into account the incoherent interactions, when in fact EBSD is the diffraction of incoherent backscattered electrons. Thus theory of EBSD should include a combination of coherent and incoherent scattering with multiple elastic and inelastic events. However, the exact treatment which includes all these conditions is the most complicated problem in electron diffraction [**28**,**32**], and will not be discussed here. Instead, it can be shown that with a few justifiable assumptions, the dynamical theory of diffraction formulated for TEM can be applied in exactly the same manner to describe the dynamical diffraction from incoherent scattering in EBSD [**28**]. This can be used to describe the major features of intensity contrast.

If it is assumed that all the intensity from the electron beam is incoherently scattered for all the crystal atoms and emitted isotropically in all direction, any theory that describes diffraction of a single plane wave by a crystal can be used to calculate EBSPs [**28**]. It will be described below how this assumption allows EBSPs to be calculated using the same theories described above for TEM. However in this description, the exact details of scattering are ignored, especially the fact that incoherently and inelastically scattered electrons are not distributed isotropically, but are dominantly scattered in the forward direction [**28**].

When formulating a method of describing EBSD, as mentioned earlier, the location where the backscattering event takes place can be thought of as an independent source of electrons emitting divergent electron waves from within the crystal (Figure 1.5) [**28**,**33**]. Thus the incident plane wave has been transformed into individual spherical waves emanating from scattering

centers at source point P. Since probability of a backscattering event is highest at the location of the nuclei, the source P is located at the atomic positions. This spherical wave has no phase relationship to the incident plane wave or spherical waves from other scattering centers. Due to this incoherency, interference effects between these waves will not take place. A single spherical wave, however, by definition is perfectly coherent with itself meaning that it will diffract as it propagates through the crystal [**28**]. The goal here is to determine how this diffraction process leads to the contrast in EBSPs.

Since the formulation presented earlier for TEM is for plane waves, instead of inspecting how the spherical wave is diffracting, a spherical wave can be treated as a superposition of infinite plane waves going into source P from all directions (Figure 1.6). Now the problem has been transformed from a single plane wave incident on the crystalline sample to an infinite number of planes waves going into P. Two more simplifications can be made at this point.

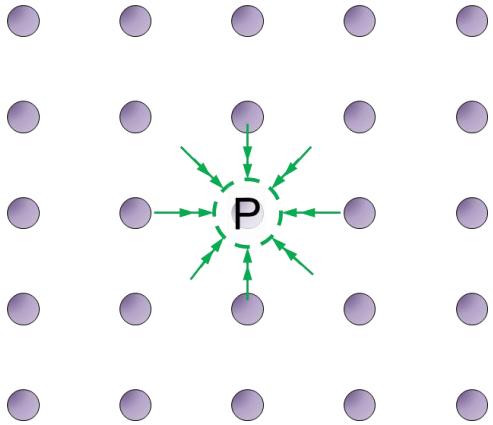

Figure 1.6: The spherical wave emanating from point P has been replaced by a superposition of plane waves going into P from all directions, adapted from [**28**].

In an EBSD experiment, the electron is essentially detected at an infinite distance away from the sample as compared to the distance between the scatterers. Point D on this detector can be assumed to be produced by a plane wave travelling towards D. Thus, instead of determining the intensity of all the plane waves going into P, only the total intensity that is finally ending up in the plane wave component that is travelling towards D needs to be determined [**28**]. To determine out of all the plane waves going into P, which finally end up as a component of plane wave travelling towards D is still not a simple task. A second simplification can be made at this point through the reciprocity theorem. This theorem, as shown in Figure 1.7 simply states that

determining the intensity at point D on the detector caused by scattering from point P is equivalent of determining intensity at point P caused by scattering from point D [**10**,**34**]. Therefore, the reciprocity theorem can be used to follow the plane wave arriving at point D on the detector and trace it backwards to the source point P, and then calculate how this single plane wave from D is scattered by the atoms of the sample until it reaches point P.

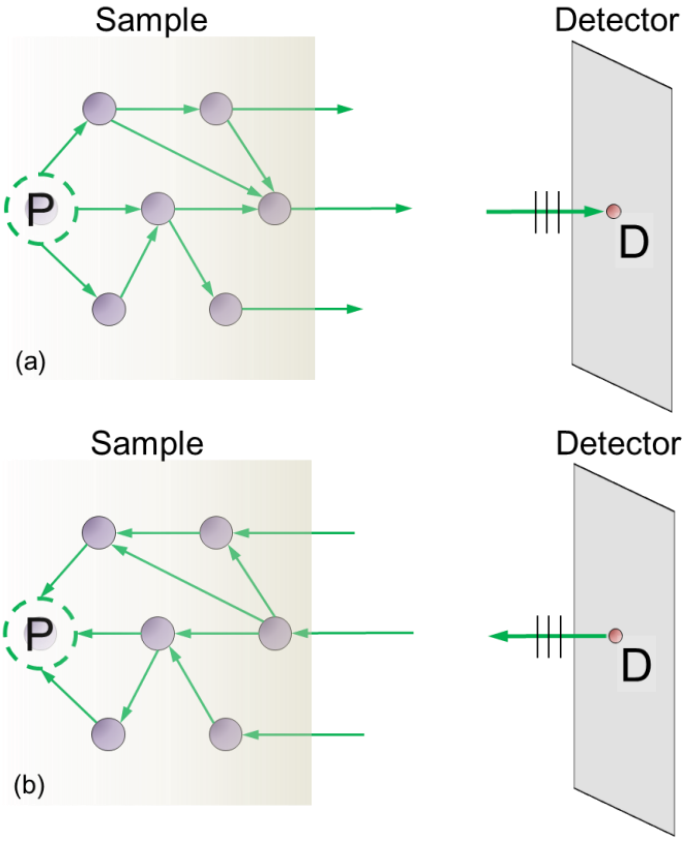

Figure 1.7: Schematic representing the Reciprocity Theorem; plane waves scattering from point P in the sample produce intensity at point D on the detector (a) which is equivalent to intensity produced at point P with plane waves scattering from D (b). Adopted from [**10**].

The goal of this section was to describe how EBSD can be related to TEM. From the assumptions and theorem described above, it can be concluded that the time-reversed path of EBSD is a plane wave impinging on a crystalline sample from infinity (from point D on detector to point P in the sample), which is exactly the same situation as diffraction in TEM, where a single plane wave (electron beam) is impinging the crystal [**28**]. Consequently, the theoretical framework used to describe dynamical diffraction in TEM can be used to describe EBSD patterns also, with

the only major difference that in TEM, the relevant thickness is the thickness of the sample, whereas in EBSD, the plane wave needs to be evaluated at the thickness of the emitter at point P (the shaded region of the sample from the surface to point P of Figure 1.7). Another factor to note is that backscatter electrons have a reflection-like geometry, so while TEM is monitoring the transmitted electrons, EBSD is monitoring the reflected electrons, which results in opposing intensities. The theory of reciprocity also links EBSD to a technique known as electron channelling pattern (ECP), where the total number of backscattered electrons is monitored as a function of the incidence angle of an electron beam. Conclusions and calculations on EBSD have also been drawn from previous studies of ECP by the dynamical theory [**10**].

1.5.2 Geometry of EBSP

An EBSP consists of bright intersecting bands on a continuous background, as shown in Figure 1.8. Each bright band is produced by a set of crystalline planes inside the sample. The schematics in this section will show that width of the bands is related to the d-spacing of the planes that produced the bands, and the angle between the bands represents the angles between the planes.

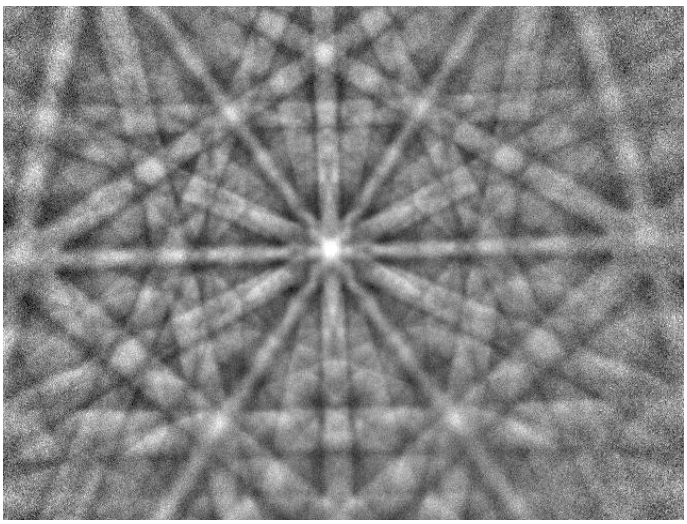

Figure 1.8: EBSP from an AuNP

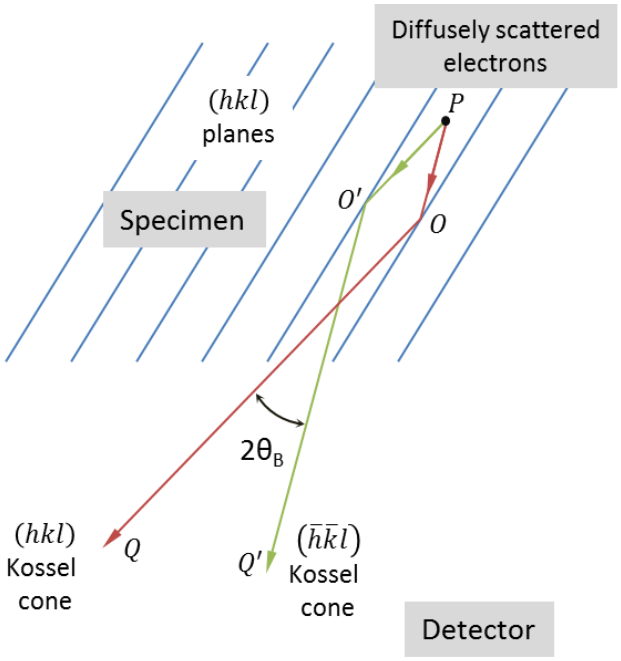

Figure 1.9: Geometrical schematic of Kikuchi Lines. Diffusely scattered electrons from source point P arriving at Bragg angle to the plane diffract creating a pair of Kossel cones for each set of planes which appear as Kikuchi lines on the diffraction pattern. Adapted from [**12**]

From Figure 1.9, the scattering centers from where the spherical wave originates is labeled as the source point P. The source point emits waves in every direction, which results in a continuous background in the EBSP. Some of the waves emitted from P will interact with a lattice plane at the Bragg angle, θ_B, and will consequently diffract away from the plane at the same angle. In Figure 1.9, the wave in direction PO arrives at Bragg angle to the crystal plane and diffracts in the direction OQ, while PO' similarly arrives at Bragg angle and diffracts in the direction of O'Q'. Thus intensity in these two directions will be different (modulated) as compared to the rest of the continuous background. In three dimensions, as described in [**12**], cones of diffracted electrons are produced instead of beams since there is a range of incident $\boldsymbol{k}$-vectors as opposed to a single incident $\boldsymbol{k}$-vector. Taking into consideration all the vectors at θ_B, a pair of cones, called Kossel cones, is formed from each set of planes. When the pair of cones with a small semi-angle intersects with the detector plane, it appears as a pair of parallel lines, called the Kikuchi lines. The Kikuchi lines together bound the region referred to as the Kikuchi band.

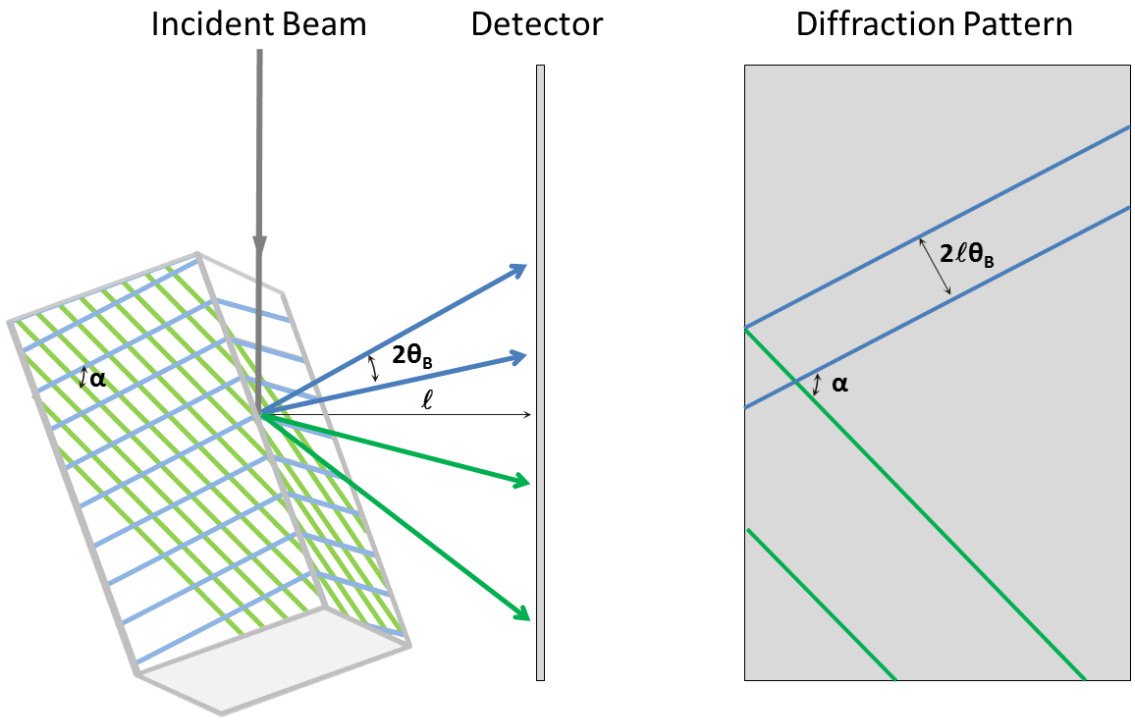

Figure 1.10: An electron beam impinges on a sample where two sets of diffracting planes are shown in grey. Each set of planes produces a pair of Kossel cones which are projected onto the detector as Kikuchi lines. The Kikuchi lines from the Kikuchi band whose width relates to the d-spacing of the diffracting planes. The angle between the diffracting planes is conserved.

The diffracted cones are separated by $2\theta_B$, as illustrated in Figure 1.9. In Figure 1.10, which illustrates the situation for two sets of lattice planes, it can be seen that the Kikuchi bands will have a width of approximately $2l\theta_B$ where l is the distance between the source of the diffraction point and the detector. Since θ_B is inversely related to d-spacing of the planes from Bragg's law in Equation (1.2), crystal planes with a larger d-spacing will produce narrower Kikuchi bands. From Figure 1.10, it is also apparent that the angle between the Kikuchi bands (α) is directly related to the interplanar angles of the diffracting planes. Since the width of the bands is related to the d-spacing of the planes and the angles between the bands is the same as the angles between the planes, the geometry of the EBSP is exactly related to the geometry of the crystal structure of the sample. From measuring these two parameters of the EBSP, the orientation of the crystal can be determined.

1.5.3 Intensities of EBSP

From Bragg's condition and earlier arguments, the diffraction pattern is expected to have two bright Kikuchi lines for each crystal plane superimposed on a diffuse background. As apparent from the EBSP in Figure 1.8, Kikuchi bands are characterized by two dark Kikuchi lines with a region of high intensity in the middle. Each band corresponds to a set of crystal planes in the sample and the intersection of bands corresponds to the zone axis. These intensities are nearly opposite of what is predicted from Bragg's law. Instead, intensity of Kikuchi bands can be obtained from the dynamical theory. Arguments by Reimer in [**17**] show that at least three beams need to be considered to obtain the correct intensity distribution of an excess band. However, here the two beam approximation of the dynamical theory, according to Winkelmann in [**10**] will be used to describe, only qualitatively, the intensities of EBSP. As described in Section 1.4.2, propagation of the incident electron wavefunction within the crystal is approximated as the sum of two Bloch waves; the incident wave and the diffracted wave. The resulting Bloch wave 1 and Bloch wave 2 at Bragg position were plotted in Figure 1.4. This method has been used to describe intensity distribution in ECP [**22**] and can be similarly used to explain the basic intensity distribution of EBSP [**10**].

Each of these two beams are scattered as they propagate through the lattice, however, amplitude and scattering coefficient of each wave is different. Both the amplitude and scattering coefficient vary according to diffraction conditions [**11**]. As described in Section 1.4.2, the scattering coefficient of Bloch waves is also dependent on the position of Bloch wave maxima with respect to the position of atoms in the lattice [**11**]. Since the probability of backscattering is highest at the atomic sites and electrons in Bloch wave 1 have a higher probability to be found at the lattice planes, it is clear that they will backscatter more strongly than electrons in Bloch wave 2. At Bragg position when $\theta = \theta_B$ or $s = 0$, it has been shown in Section 1.4.2 that both of the waves are excited with equal amplitude and contribute equally to the total wavefunction [**22**]. For angles smaller than the Bragg angle, $\theta < \theta_B$ and $s < 0$, the intensity of Bloch wave 1 is higher than the intensity of Bloch wave 2 [**35**] whereas for angles larger than Bragg angle, $\theta > \theta_B$ or equivalently $s > 0$, Bloch wave 2 is preferentially excited (Refer to [**25**] for detailed derivations). Since the intensity of EBSP is a function of the sum of Bloch wave 1 and Bloch wave

2 [**11**], the angular range between $-\theta_B$ and $+\theta_B$ will have an increased intensity due to enhanced backscattering [**35**], which results in a bright band with an angular width of $2\theta_B$ as shown in Figure 1.11. Just outside of this range, where $s > 0$, electrons in Bloch wave 2 whose probability density mostly lies in the interstitial regions, channel into the crystal more efficiently [**22**]. Since this reduces the probability of electrons being backscattered, the intensity in this region is lower, corresponding to the edges of a Kikuchi band in Figure 1.11. Another method of understanding this intensity distribution is from the reflection-like geometry of backscattered electrons. At the atomic planes, electrons are backscattered forming a bright band while the electrons between the atomic planes channel into the crystal and result in the dark edges. The overall result is a modulation of the backscattered electrons coming off the sample, where incident angles $\theta < \theta_B$ would result in a higher intensity than the background, producing a bright Kikuchi band. This band is bounded by dark edges as the intensity is lower than the background for $\theta > \theta_B$.

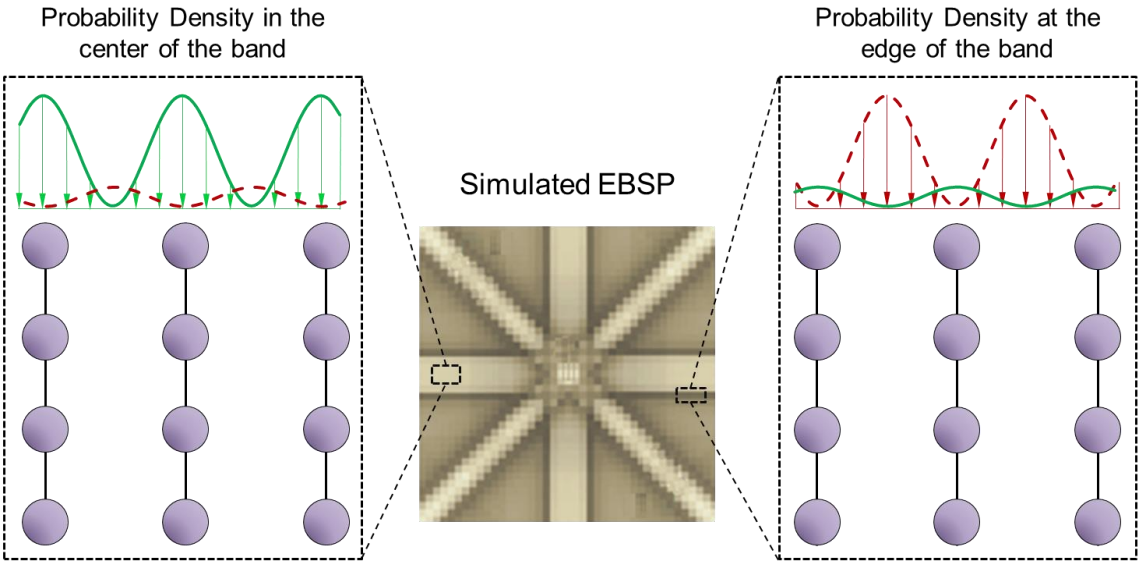

Figure 1.11: The probability density of electrons in Bloch wave 1 (green solid curve) and Bloch wave 2 (red broken curve) at the center and at the edge of the Kikuchi band. At the center, Bloch wave 1 is preferentially excited producing a high intensity in the center, while at the edge, Bloch wave 2 is excited which results in a dark edge.

Once again, Figure 1.11 shows that high intensity in the middle of the Kikuchi bands is due to the fact that the probability density is concentrated mainly at the atomic planes and low intensity at

the edge is a result of probability density being mostly between the atomic planes [**10**]. Details on other contrast features of EBSPs can be found in [**10**,**17**,**26**].

1.5.4 Contrast Reversal

Contrast reversal has been observed in EBSD experiments, albeit rarely since BSEs from small depths dominate [**28**]. Due to the nature of the work presented here, signal from large depths will be observed often, producing reversed contrast EBSPs as shown in Figure 1.12, and thus the mechanisms which produce such a phenomenon are discussed here.

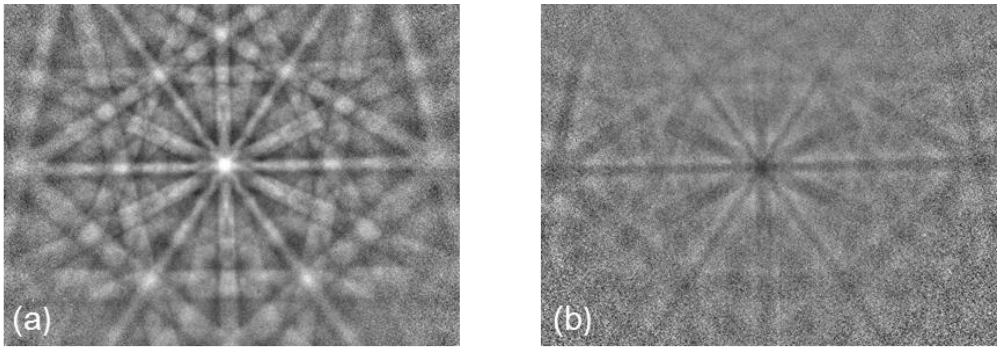

Figure 1.12: (a) Diffraction pattern from Au showing the expected contrast of bright bands with dark edges, whereas (b) shows the same pattern with reversed contrast – it has dark bands with bright edges.

Zaefferer [**36**] uses only the kinematical intensities for simulating EBSPs and even from large depths, the simulations do not predict reversed contrast. Winkelmann et al. [**28**,**37**], on the other hand, uses dynamical simulations that show evidence of reversed contrast Kikuchi bands for large depths. Alam et al. [**38**] first reported reversed contrast EBSPs through changing the incidence angle of the primary beam, effectively allowing the incident beam to penetrate deeper into the sample. A similar experiment is repeated by Winkelmann et al. where the incidence angle is varied and the compared to simulated EBSPs to study the depth distribution of BSEs in more detail [**37**]. Since dynamical simulations can predict the details of contrast reversal [**37**], concepts from dynamical diffraction of electrons will be used to qualitatively describe the processes that produce contrast reversal in EBSPs.

To describe how contrast reversal occurs, consider again the two-beam approximation described in Section 1.4.2, where wavefunction inside the crystal is described as a general sum of two

Bloch waves. This approximation was also used to describe the intensities of EBSPs earlier in Section 1.5.3, and can be used again in a similar fashion to describe the intensity changes in EBSPs from this experiment.

The diffraction pattern on the detector is a sum of all the Bloch waves emanating from the sample. In this method, it is approximated that the superposition of only Bloch wave 1 and Bloch wave 2 forms this diffraction pattern. While the probability density of Bloch wave 1 is at its maximum at the atomic sites, Bloch wave 2 exhibits maxima between the atomic planes. High intensities are expected when the probability density strongly overlaps the locations where scattered electrons are created [**10**]. This gives rise to the bright bands from Bloch wave 1 with dark edges due to Bloch wave 2.

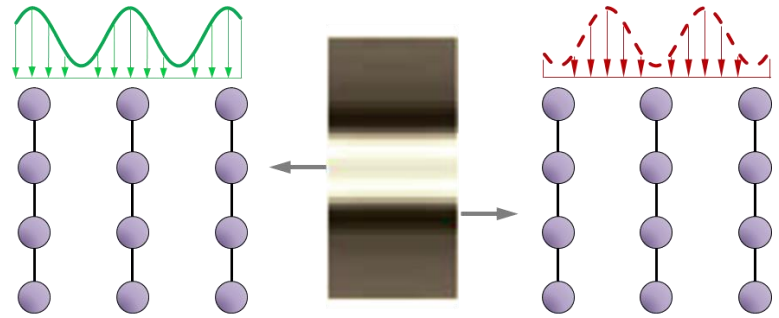

(a) Shallow Backscattering

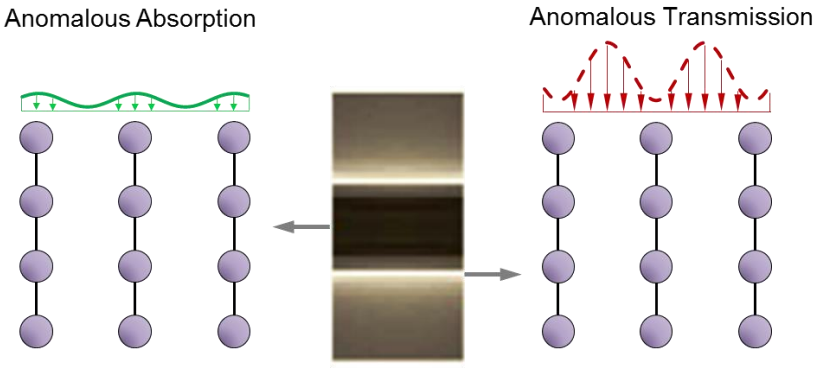

(b) Deep Backscattering

Figure 1.13: Intensity Distribution of Bloch wave 1 and Bloch wave 2 inside the crystal. Shallow backscattering (a) produces bright bands from Bloch wave 1 with dark edges from Bloch wave 2. At high depths (b) contrast reversal is seen due to anomalous absorption of Bloch wave 1 (modified from [**10**]).

Since Bloch wave 1 has maximum intensity at the atomic planes, meaning that electrons in Bloch wave 1 are more likely to be in the vicinity of the atoms, these electrons will be absorbed more strongly due to the to the high probability of scattering at the atomic sites. Whereas Bloch wave 2, with maxima between atomic planes, will encounter a much lower probability of scattering. Consequently, with increasing thickness, the intensity of Bloch wave 1 will reduce increasingly while the intensity of Bloch wave 2 will not reduce as significantly. This difference in the attenuation factor of the Bloch waves is known as anomalous absorption. It was earlier introduced as the absorption parameter ***q(j)*** in Equation (1.24) for Bloch waves in Section 1.4.1. Thus anomalous absorption can be incorporated mathematically through assigning a unique ***q(j)*** to each Bloch wave. It is this phenomenon of anomalous absorption that gives rise to the reversed contrast Kikuchi bands as described in Figure 1.13.

At Bragg position, $s = 0$, both of the waves are excited with equal amplitude. Negative deviations from this condition, $s < 0$, result in highly excited Bloch wave 1 producing the bright bands in EBSP (Figure 1.13a). However, due to anomalous absorption, these are more strongly absorbed also, and with higher thicknesses it results in the dark deficit bands seen in reversed contrast EBSPs (Figure 1.13b) [**10**]. Positive deviations from the Bragg condition, $s > 0$, cause Bloch wave 2 to be highly excited, which channel into the lattice more efficiently and produce the dark edges in Figure 1.13a. Since Bloch wave 2 is weakly absorbed over greater depths, it will survive the scattering by propagating between the atomic planes and thus will not be attenuated as much as Bloch wave 1, producing bright edges on the reversed contrast EBSP in Figure 1.13b.

Another simple method of describing this phenomenon is to realize the difference in contrast expected from a reflection-like geometry and transmission geometry. When the source is close to the surface, the electrons on the detector are produced from the reflection-like geometry of backscattered electrons. The areas that result in the highest production of backscattered or reflected electrons will have the highest intensity on the EBSP. As mentioned earlier, this obviously occurs at the atomic planes. At other locations, probability of backscattering is low, and thus electrons will channel into the crystal. On the other hand, when the source is created deep within the sample, the detector perceives a transmission-like geometry. The diffraction pattern from the source has to travel through the sample thickness before reaching the detector. The locations which result in highest amount of scattering will now result in the lowest

intensities since these electrons will be scattered away before reaching the detector. Evidently, this will once again occur at the atomic planes. On the other hands, electrons that are not scattered away are of Bloch wave 2, which will channel between the planes and reach the detector. Therefore, when the source of backscattered electrons is deep within the sample, the anomalous absorption of Bloch wave 1 produces the dark bands of the reversed contrast EBSP (Figure 1.12b) while the anomalous transmission of Bloch wave 2 produces the bright edges.

2. EQUIPMENT AND METHODOLOGIES

2.1 Sample Preparation

The main sample that is used for the experiments in this work consists of crystalline gold nanoparticles (AuNPs) on single crystal spinel ($MgAl_2O_4$). Samples are prepared by first dicing and cleaning the substrate. A thin film of gold is then deposited onto the clean substrates and annealed at high temperatures. The details of the experiment, such as the thickness of the gold film and the annealing temperatures are all chosen based on the pervious results reported by Majdi [**1**]

The substrate consists of a polished single crystal (111) $MgAl_2O_4$ from MTI corporation. Using a MicroAce Series 3 dicing saw, the sample is diced to a size of 6mm by 10mm. To clean the sample, it is first rinsed with isopropanol. Each side of the sample is then wiped with a clean lens paper and positioned in a sample holder. The sample holder is placed in a beaker of isopropanol, which is placed in a sonicator for 40 min. The sample holder is then removed and placed in a beaker of methanol and sonicated for another 40 min. Finally, this step is repeated in a beaker of acetone and sonicated for 90 min. The exact details of the cleaning procedure are found in [**1**].The samples are removed and inspected through an Optical microscope (Olympus BX-61) to ensure a clean surface.

Once the $MgAl_2O_4$ substrate has been diced and cleaned, GATAN PECS Model 682 ion beam coating/etching system is used to sputter 10nm of gold on it. The details of the experimental settings used for this procedure can be found in [**1**]. The sample is then placed under an inert Argon atmosphere in a Lindberg Hevi-Duty quartz tube furnace for annealing. Once again, refer [**1**] for the exact details of the annealing system. The sample is heated to 1110°C in 1.5 hours and kept at this temperature for another 1.5 hours. It is then cooled to 956°C in 0.5 hours and kept at this constant temperature for another 2 hours. The furnace is then turned off and the sample is left to cool to 30°C for 14 hours. SEM image of the sample produced from this method is shown in Figure 2.1 at a 70° tilt.

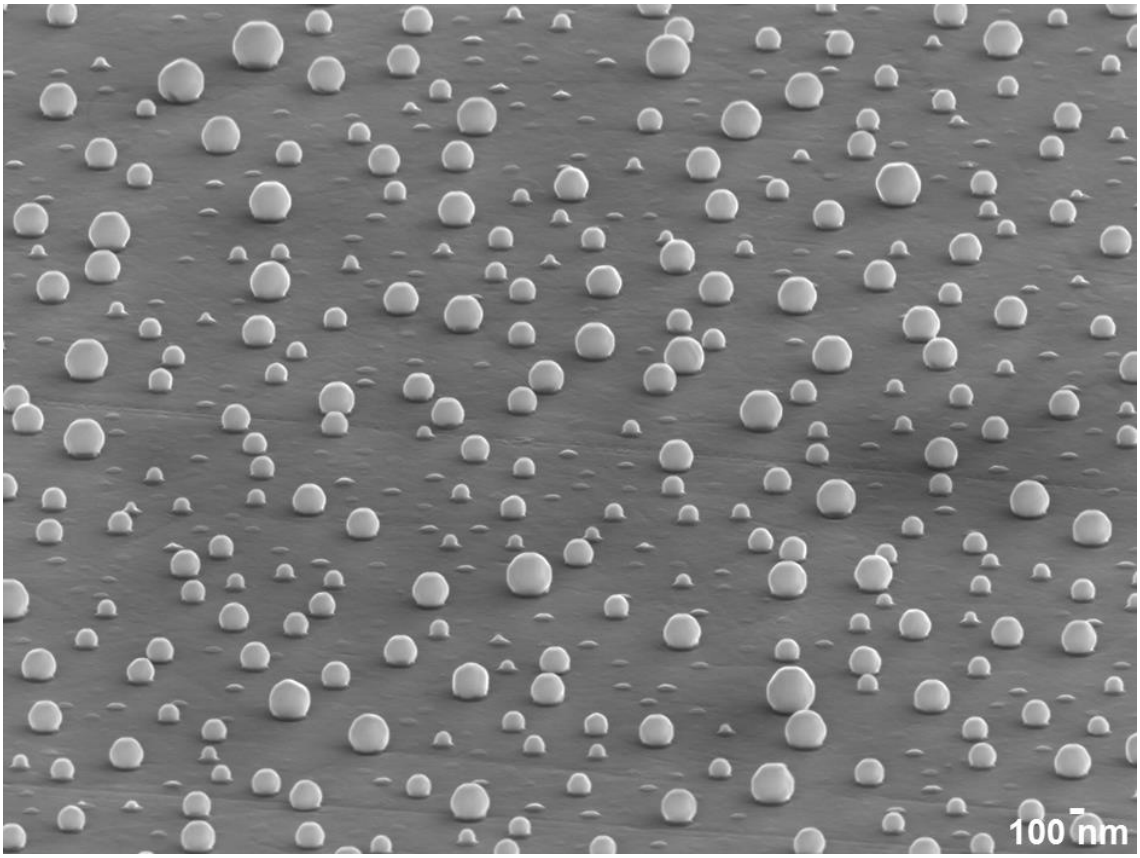

Figure 2.1: SEM image at 70° tilt of the primary sample used in this study where AuNPs form faceted polyhedron on the spinel substrate.

The sample prepared from this method with the particular heating profile described above is the primary subject of this work and will be the default sample in all the experiments. The only other sample studied in one of the experiments is an AuNP sample that is annealed at lower temperatures and will be referred as the 'low temperature sample' to distinguish it from the primary sample. This sample uses the exact method described above, except the final annealing step has been modified. This sample is a low temperature sample that is heated to 645°C in 35 minutes and then left to cool back to room temperature. Due to the low temperature, the nanoparticles do not form clear facets or intricate Au-$MgAl_2O_4$ nanostructures [**1**], instead remain as dewetted gold nanostructures, as shown in Figure 2.2.

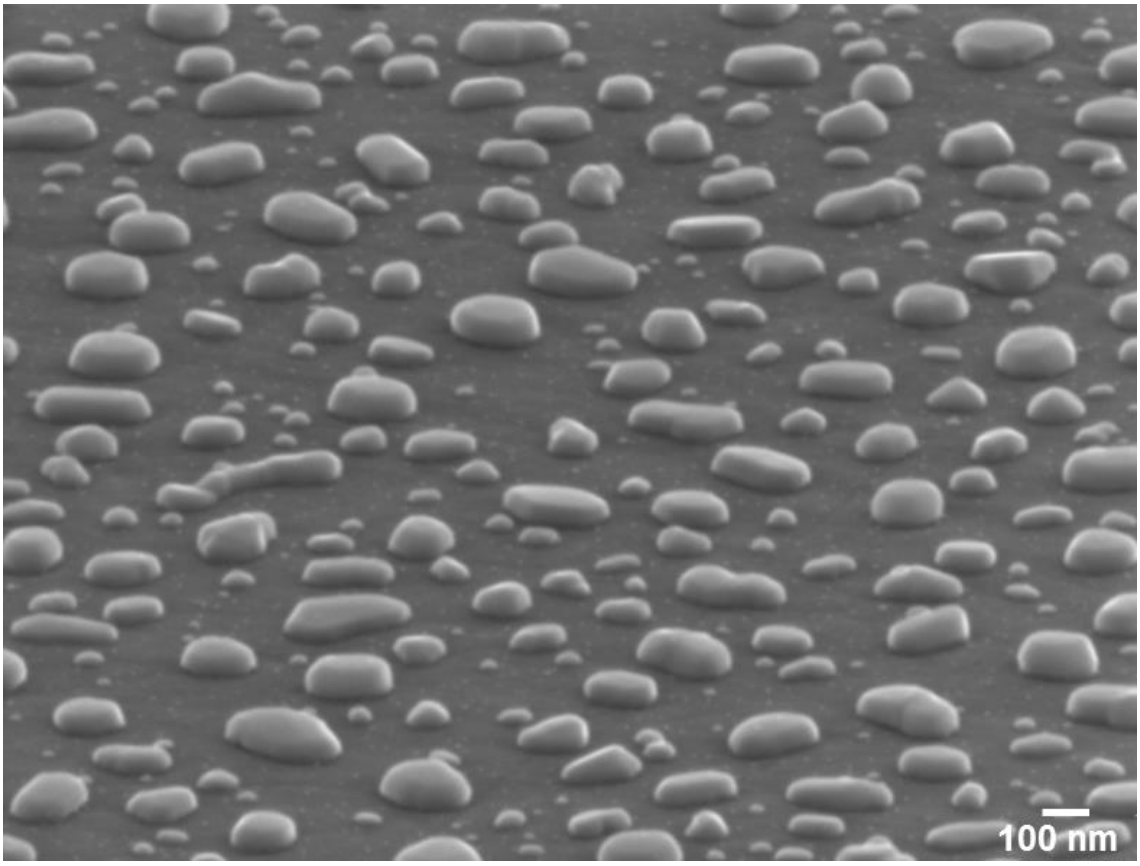

Figure 2.2: SEM image at 70° tilt of the low temperature sample where the AuNPs have not formed the well faceted polyhedrons instead remain in a drop-like shape.

Since the substrate is non-conductive, all the samples are coated with a thin conductive coating layer through GATAN PECS Model 682 ion beam coating/etching system. As EBSD is a near-surface technique, even a thin coating will degrade the quality of the EBSPs. For this reason, a thin coating of carbon is applied since the low Z number of carbon will have minimal effect on the EBSD signal produced by the sample [**39**]. The sample is mounted on a sample holder for SEM through application of silver paste on all four edges of the sample. This step not only keeps the sample glued to the holder but it to also further alleviates charging effects by grounding the sample through the conductive silver paste.

2.2 Equipment for EBSD

An EBSD system requires the following components:

- SEM
- EBSD Detector
- Software

2.2.1 Scanning Electron Microscope (SEM)

The EBSD system is installed in a scanning electron microscope. Schematic of the major components of SEM is shown in Figure 2.3 along with an image of the JOEL JSM-7000F FEGSEM (JEOL Ltd., Tokyo, Japan) used for the experiments in this paper. Major components of an SEM include [**40**]:

- Electron gun used to produce electrons. Field emission gun is used for high performance in EBSD.
- Electron optics to focus the incident primary electron beam on the specimen.
- Sample chamber, stage and stage control to mount and manipulate the specimen under vacuum. The stage can move in x, y, and z direction, rotate about z and tilt from 0^{o} to 75^{o} about x.
- Detector to capture relevant signals, including the secondary electron detector to image the sample while an EBSD detector is required to capture the diffraction patterns.
- Electronic components; which include hardware to control the beam and the stage and software that allows user to control, monitor, and obtain relevant data.

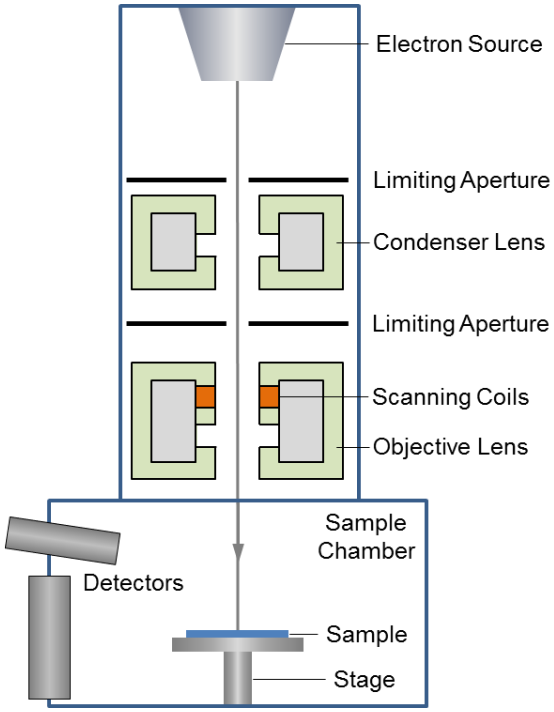

Figure 2.3: Principal Components of the Scanning Electron Microscope (SEM).

As mentioned above, for all the experimental results presented here, JEOL JSM-7000F in the Canadian Center for Electron Microscopy (CCEM) at McMaster University is used. It is equipped with a field emission gun which offers both, a high resolution and long-term stability of the beam current, and thus performance-wise, is the optimal choice for EBSD experiments [**10**]. To minimize contamination and excessive scattering, a clean vacuum in the specimen chamber is provided. For the EBSD system, SEM also contains an interface to mount the detector onto the relevant SEM port. This port is located at normal direction to x-axis of the stage and can accommodate for the EBSD detector. Finally, the SEM computer interface is fast and proficient to achieve high speed digital beam scans, flat imaging, and dynamic focusing [**10**].

2.2.2 EBSD Detector

The detector for EBSD consists of a phosphor screen coupled with a charge coupled device (CCD) detector. The detector is mounted on a retractable stage, where the insertion and retraction is controlled through a handset [**41**]. This enables the detector to be positioned accurately and

retracted when not in use. The nose section of the detector has a transparent phosphor screen which is fluoresced by electrons to form the diffraction pattern [**42**].

The detector equipped in the JEOL 7000F is a NordlysNano system (Oxford Instruments, Oxfordshire, United Kingdom). The rectangular phosphor screen is directly coupled to a sensitive CCD detector through a tapered fiber optic bundle, producing high resolution images (1344x1024 pixels). Finally, vacuum seals are required to guarantee a clean vacuum. The image acquired from the detector is the only source of information used for EBSD analysis, thus special attention is given to the detector to ensure high sensitivity, speed, and image quality [**10**].

2.2.3 Software

A computer is required for communication control of the SEM beam and stage and also for acquisition and analysis of EBSPs. With the Nordlys detector, a firewire (IEEE 1394) is used to transfer diffraction patterns to the computer [**41**]. The software controls the digital beam scan and mechanical stage scan, needed especially for automated EBSD, while also controlling the modes of SEM operation, and finally for collecting, processing, and analyzing diffraction patterns through an indexing software [**10**]. AZtec 2.4 (Oxford Instruments) is used for acquisition and analysis along with Channel 5 software (HKL Technology, Habro, Denmark) is used to create pole figures.

2.3 Experimental Setup for EBSD

An EBSD system is installed in a SEM. Under vacuum, the primary electron beam is focused on the sample, which is placed at an optimal 70^{o} tilt from the horizontal. Since backscattered electrons are high energy electrons that travel in straight lines, the EBSD detector is placed parallel to the primary beam, facing the point of impact between the beam and sample. When the high energy backscattered electrons strike the phosphor screen of the detector, fluorescence takes place, and the image on the screen is captured by a charge-coupling device (CCD). The signal from CCD is digitized and sent to a computer that is connected to the system. This setup is shown in Figure 2.4 and Figure 2.5.

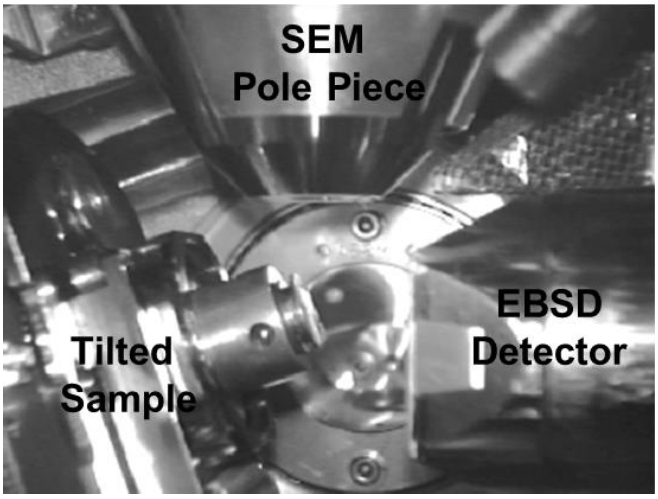

Figure 2.4: Image from inside the SEM chamber displaying the principal components of an EBSD system

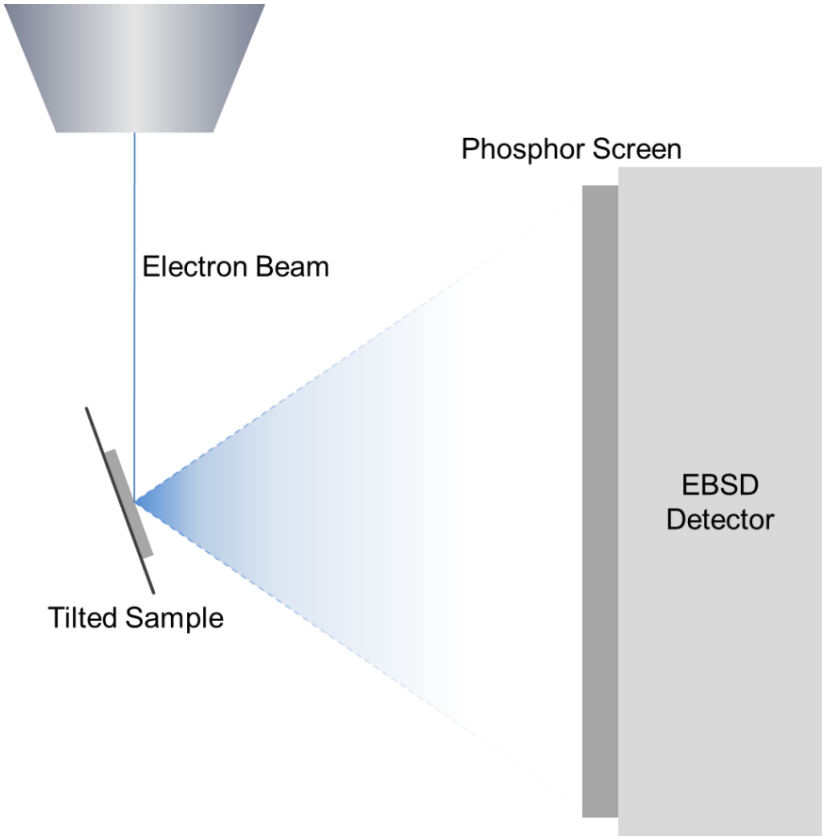

Figure 2.5: Schematic displaying the experimental setup

2.3.1 SEM Configuration

The quality of an EBSD experiment can be improved by determining optimal parameters for the particular sample that is under investigation. To obtain high spatial resolution, it is essential that the geometry of the system is well calibrated while optimizing the electron beam. The three important components of the geometry of the system that affect the spatial resolution and pattern quality of EBSD are: a) Specimen Tilt, b) Working Distance, and c) Specimen-to-screen distance, shown in Figure 2.6.

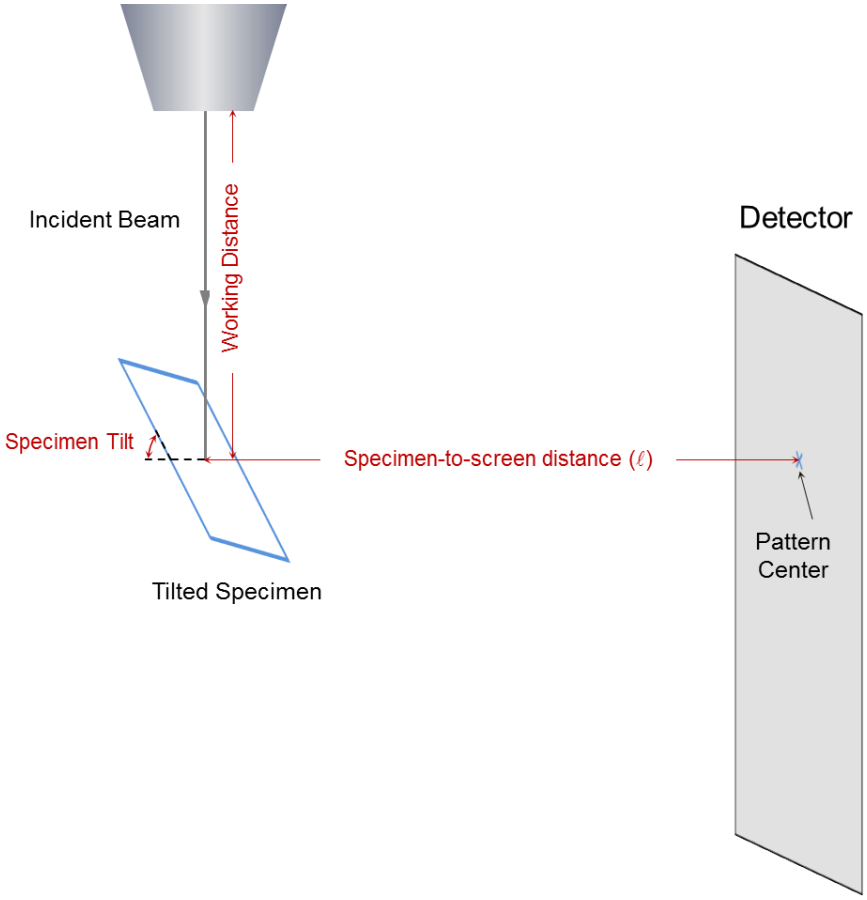

Figure 2.6: Schematic of the experimental setup of EBSD highlighting the three main components that determine the geometry of the system.

The modulation of backscattered electrons due to diffraction is superimposed on the angular distribution of backscattered electrons from the specimen. As shown in Figure 2.7, this angular distribution approximately follows a cosine function which is highly peaked approximately

around the specular reflection of the incident beam [**13**]. As the tilt angle of the specimen increases, the signal on the phosphor screen increases since the path length of backscattered electrons in the specimen decreases. Shallow angles to the beam allow a maximum number of incident primary electrons to scatter and escape from surface with minimal energy loss [**43**]. Patterns can efficiently be acquired anywhere from 60^{o} to 80^{o}, but lower angles lead to a significantly weaker diffraction patterns since the beam penetrates deeper and the number of backscattered electrons escaping the surface decreases. As the tilt angle is increased, the number of backscattered electrons escaping in the direction of the detector also increases, however, at high angles, the spatial resolution decreases rapidly as the beam elongates at grazing angles. Thus EBSD experiments are performed at an optimal angle of 70^{o} to obtain a good balance between quality of EBSP and spatial resolution [**10**].

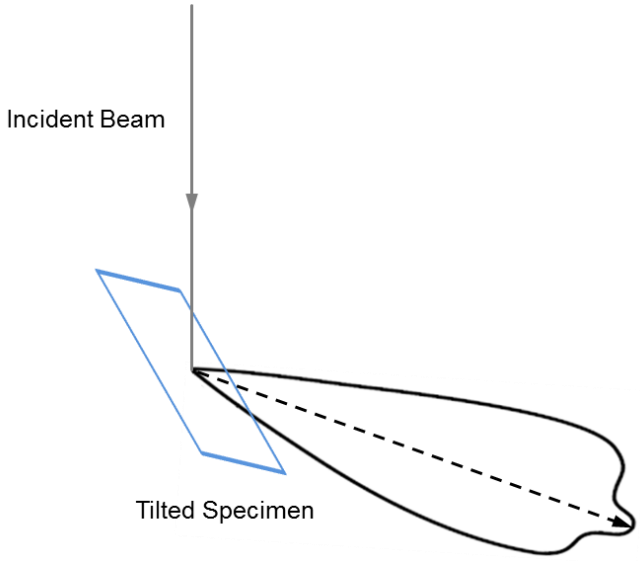

Figure 2.7: Angular distribution of backscattered electrons is peaked approximately around the specular reflection of the incident beam. Adapted from [**13**].

The working distance, highlighted in Figure 2.6, is the distance between the bottom of the SEM column and the sample. It is set such that the pattern center (point on the sample that is closest to the phosphor screen) is located about one third from the top of the phosphor screen resulting in uniform illumination across the screen. The specimen-to-screen distance measures the distance between the sample and the EBSD detector as illustrated in Figure 2.6. It is limited by the geometry of the system, and usually fixed in an EBSD system. JEOL 7000F at CCEM is

calibrated to be used at a working distance of 18.4 mm and a specimen-to-screen distance of 15 mm for a tilt of 70^{o}. All three parameters are set according to the geometry of the SEM and it was verified that these settings are optimal for EBSD experiments of AuNP samples.

The other parameters of the SEM that need to be considered are the probe current and accelerating voltage of the beam. The current required for EBSD needs to be high enough to generate a high quality signal on the detector. A high quality diffraction pattern will have increased contrast while the acquisition time of the detector can remain low, allowing for high speed experiments. However, this may lead to sample damage and charging effects, which will degrade the quality of the pattern and may produce misleading results. Probe currents in the range of 5 nA – 10 nA are generally considered optimal for EBSD experiments [**41**]. Finally, another critical parameter for EBSD experiments is the accelerating voltage of the beam, which should be in the range of 10 keV to 30 keV [**10**]. A high voltage is needed to produce a high signal to noise ratio for EBSP. High energy beam results in a brighter EBSP and increased efficiency of the phosphor screen. Furthermore, surface conditions will not have a strong influence on the quality of the pattern since high energy electron beam will penetrate deeper into the surface. In addition, due to the Bragg relation, if low accelerating voltage is used, Kikuchi bands will broaden and overlap, making the pattern difficult to index. However, a high energy beam leads to a large interaction volume, consequently decreasing the spatial resolution. It can also damage the sample, as is the case with AuNPs, and worsen charging effects. Therefore, the optimal voltage should be chosen based on how these factors affect the sample [**41**].

Once the sample is prepared, it is mounted onto the sample holder and placed in the SEM chamber. After high vacuum is achieved, the sample is imaged from the secondary electron detector. The probe current that produces a high quality of EBSP while also avoiding any charging is determined through experimentation. The accelerating voltage is varied from 10kV to 20kV and the optimal condition for AuNPs is determined to be 15 keV. The sample is tilted to 70°, working distance is set at 18.4 mm, and the EBSD detector is inserted to the pre-set value which results in a specimen-to-screen distance of 15 mm. These parameters provide a high contrast EBSP for the AuNP samples.

2.3.2 Automated Indexing

Whereas the instrumentation of EBSD and collection of patterns is relatively simple, processing data from EBSP is much more complicated. The method used to perform EBSD experiments on AuNP is an interactive semi-automated method. The user selects the location of the beam for the collection of EBSP while the indexing is performed automatically through the computer software. The indexing software, AZtec, collects, processes, and analyzes the diffraction patterns. For such automated indexing, the EBSD detector has to be calibrated for the appropriate geometry of the system. Once the detector has been calibrated, the beam is positioned on the area of interest and an EBSP is obtained. The image is processed through a background correction routine and adjusted for contrast. For automated indexing, EBSD software then performs a Hough transform to the pattern to determine the widths and angles between the Kikuchi bands. This data is compared to a simulated diffraction pattern and a solution is determined when this simulated pattern matches the actual pattern.

Calibration

The geometry of the system must be known for the software to index the patterns accurately. As displayed in Figure 2.6, sample-to-screen distance is the distance between the interaction volume from where the signal originates and the pattern center, where pattern center is the point on the phosphor screen that is closest to the interaction volume. Once these projection parameters of the pattern are accurately calibrated [**44**], it can be saved and loaded for use later. Calibration for the Nordlys detector at CCEM was performed when the system was installed by measuring the pattern of a cleaved Si crystal and comparing it to a known pattern. This allows the system to accurately calibrate the position of the pattern center and the specimen-to-screen distance. The data from calibration is saved in the software and will be loaded automatically of an experiment.

Background Correction

An EBSP consists of Kikuchi bands superimposed on a strong continuous background as described in Section 1.5. This causes the signal to noise ratio of EBSP to be very poor as shown in

Figure 2.8a. By removing the background Figure 2.8b, a high quality of EBSP is produced, as displayed in Figure 2.8c.

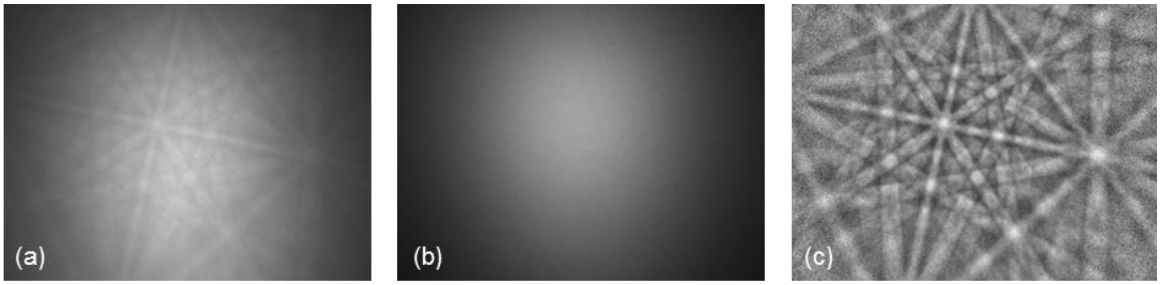

Figure 2.8: Processed EBSP in (c) produced by removing background (b) from the raw EBSP in (a)

The AZtec software allows for both dynamic and static correction methods which can be applied individually or simultaneously depending on which method produces the highest quality of processed EBSP. The dynamic method of background correction calculates the background automatically from the raw EBSP. The static method, on the other hand, requires an independent raw image which contains only the diffuse background noise, such as the one shown in Figure 2.8b. One method of obtaining this raw background image is to scan the beam in an amorphous part of the sample, which in the case of AuNPs is the silver paste at the edges of the sample. Although there are other methods which can be used, such as averaging many grains or heavy defocussing of the electron beam, for AuNP samples, silver paste was experimentally determined to be the easiest and quickest method of obtaining raw background images of sufficient quality. If the operating parameters, such as probe current or accelerating voltage, have been altered or a new sample has been placed for experimentation, the raw background image needs to be collected again [**45**]. Once the background image has been collected, it is electronically divided from the diffraction pattern, the result of which is shown in Figure 2.8c. Other pre-processing steps can also take place before the EBSP is stored for analysis, such as contrast adjustments, gain, and binning. The goal of these steps varies from experiment to experiment but the aim from these parameters is to optimize the EBSP for the given experiment.

Hough Transform

To index an EBSP, the computer needs to be able to measure the width and position of the Kikuchi bands. The diffraction pattern, however, consists of a high background noise and the lines that need to be detected are discontinuous. The human eye is capable of easily picking out features such as the Kikuchi bands even if the image is noisy. This task is not simple for the computer, however. From the minor differences in local contrast, the computer cannot easily detect all the lines that form the Kikuchi bands. For detection of lines that form the Kikuchi band, in 1992 [**45**], Krieger Lassen [**46**] proposed the use of Hough transform on EBSPs. Hough transform is used to facilitate the detection of simple shapes in an image [**10**]. This is currently the most common automated method used for detecting bands on an EBSP.

Cartesian coordinates x_i and y_i in image space are mapped into polar coordinates ρ and θ in Hough space. This transformation is shown in Figure 2.9 and is performed through:

$$\rho = x_i \cos\theta + y_i \sin\theta$$

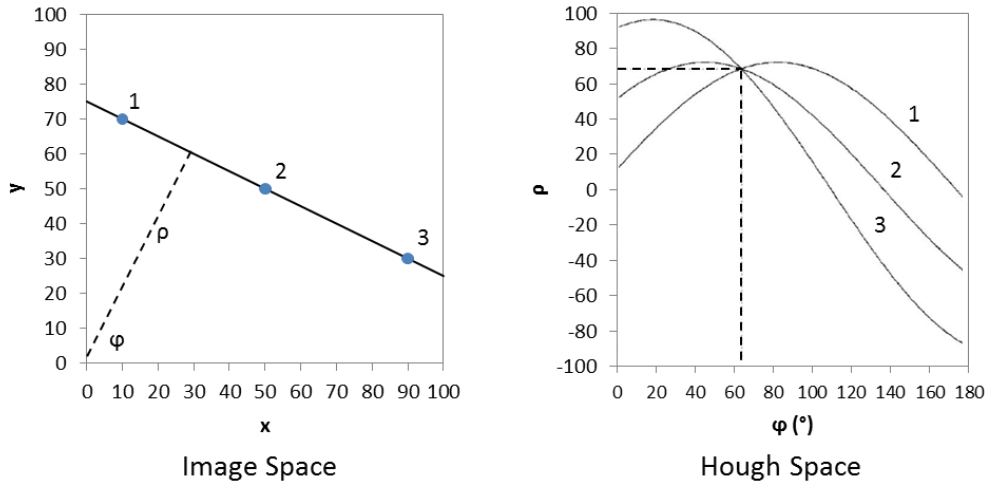

Figure 2.9: Points 1, 2, and 3 in x-y space have been transformed to curves in Hough space while a line in x-y space transforms to a point in Hough space. Adapted from [**47**].

A line in image space can be characterized by its perpendicular distance ρ from the origin and the angle θ between ρ and the x-axis. Accordingly, a line in image space transforms to a point (ρ, θ) in Hough space. A point (x_i, y_i) in image space satisfies all lines going through that point and thus satisfies a set of ρ and θ values which form a sinusoidal curve in Hough space. Consequently, sinusoids from points that are collinear in image space intersect at the parameter

(ρ, θ) of the line that connects them, as shown in Figure 2.9. A grey-tone weighted Hough transform is applied to the EBSD patterns where each pixel of intensity $I(x_i, y_i)$ on the diffraction pattern is mapped to a sinusoidal curve in Hough space with the accumulative intensity $I(\rho, \theta)$.

All the pixels in an EBSP that are collinear will produce a peak in Hough space. Points that are collinear and of high intensity, such as the points on a Kikuchi band, will result in a high intensity peak in Hough space as the intensities of all the pixels will accumulate. Due to the finite width of the Kikuchi bands, peaks in Hough space have a characteristic butterfly-like shape. From this transformation, a Kikuchi band is transformed to a point whose intensity is proportional to the intensity of the band and the shape of the peak is proportional to the width of the band. Now the computer has to simply identify the location of these peaks in Hough space.

Since the peaks in Hough space have a butterfly-like shape, a butterfly filter can be applied to facilitate the detection of peak in the Hough transformed EBSP. After the peaks have been determined, they are sorted from highest intensity to the lowest and the top peaks are used for orientation calculations [**45**] described in Section 2.4.

Indexing

Indexing a diffraction pattern refers to determining a solution for the crystal structure that corresponds to the EBSP. It is the final step in the automated process. The position of the band, width of the band and the relative intensity of each band in EBSP is determined through the Hough transform by identifying the position of the peak, shape of the peak, and the intensity of each peak in Hough space, respectively. From this information, a table which contains widths of the bands and angles between them is compiled. The experimental data is then compared to values stored in a lookup table, known as the match unit. Match unit is produced through the kinematical electron diffraction model [**41**] and contains calculated crystallographic parameters [**10**]. These parameters include indices of Bragg-diffracting lattice planes, interplanar spacing, interplanar angles, and finally the intensity of the reflector [**42**]. The bands are sorted according to their intensities as described above. Indexing is then determined from comparing the measured angles between the bands and widths of the band with theoretical interplanar angles and interplanar spacings in the match unit [**42**]. A solution is determined when a match is found.

The simulated EBSP of the solution is then overlaid the experimental EPSP for comparison, as shown in Figure 2.10. Refer to [**10**] for the detailed algorithms involved in indexing EBSP.

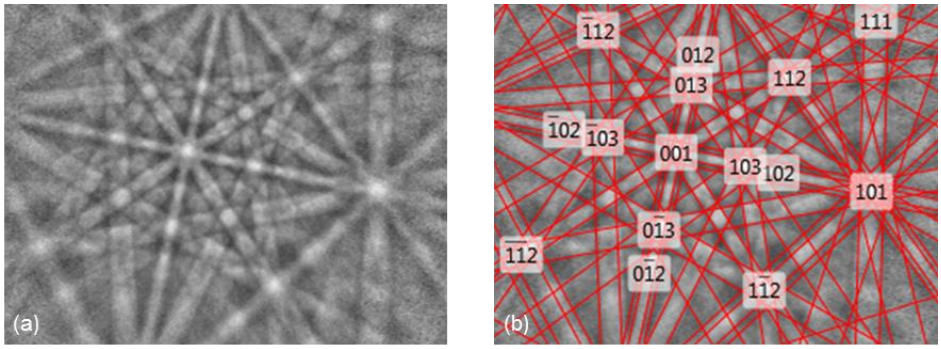

Figure 2.10: (a) Processed EBS that is indexed through the Hough transform. The overlaid solution is shown in (b).

The process of automated indexing is summarized in the schematic diagram in Figure 33. This process can be anywhere from 0.1 to 1 second in length, depending on the various parameters of the experiment [**10**]. Thus far, steps 1 to 5 of Figure 2.11 have been covered, while the final step, step 6, will be discussed in Section 2.4.

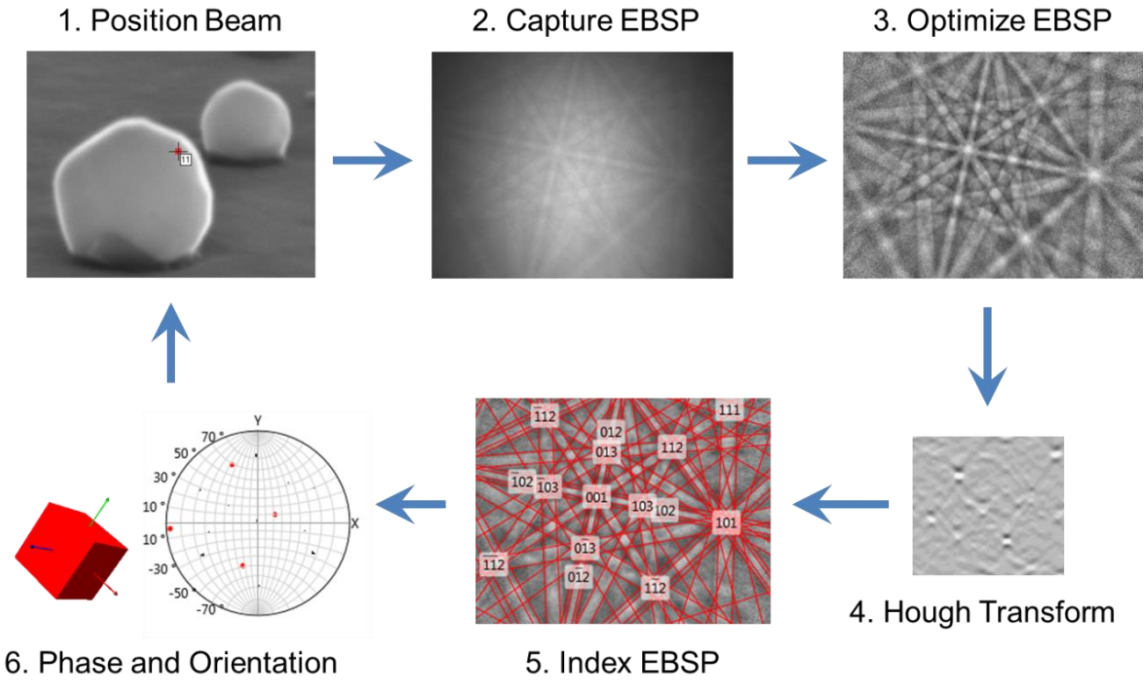

Figure 2.11: Major steps in the algorithm of automatic EBSD experiments, adapted from [**42**]

At times, if the quality of EBSP is low, misindexing may occur, where the EBSP is indexed with an incorrect solution, or the experimental data does not match the data in the match unit and results in a zero-solution. For example, at a grain boundary an overlapping pattern from the multiple grains would be produced, resulting in a poor quality EBSP. Two or more phases whose crystallographic structure is indistinguishable may also lead to misindexing [**41**]. In this case, information from other sources, such as Energy Dispersive Spectroscopy (EDS) or backscattered electron images (BEI), is needed to analyze the phases [**41**]. For grain boundaries, however, if the signal from one grain is stronger than the other, the software is able to deconvolve the overlapping pattern [**42**].

2.4 Data Analysis

The data acquired from an EBSD experiment includes the position on the sample, phase and orientation at each position, quality of the diffraction pattern, and the confidence fit of the pattern. The software outputs all of this raw data but also has the capability of constructing maps and pole figures to present this data.

2.4.1 Raw Data from EBSD

When an EBSP is indexed, its phase, XY position on the sample, orientation, goodness of fit, and pattern quality are recorded. The phase and the XY position are self-explanatory and listed in the outputs. The sections below will cover how the orientation of the crystal is given, the mean angular deviation, which measures the goodness of fit, and finally EBSP quality factors Band Contrast (BC) and Band Slope (BS).

Orientation

The orientation of the crystal indexed from the EBSP is given using the Euler angle convention. Three Euler angles, ϕ_1, Φ, and ϕ_2, are used to describe the rotations needed to transform the crystal from one orientation to another. ϕ_1 is a rotation about the z-axis, followed by Φ, which is a rotation about the rotated x-axis, and finally ϕ_2, which is a rotation about the z-axis. The schematic in Figure 2.12 illustrates the Euler angle convention used in EBSD experiments.

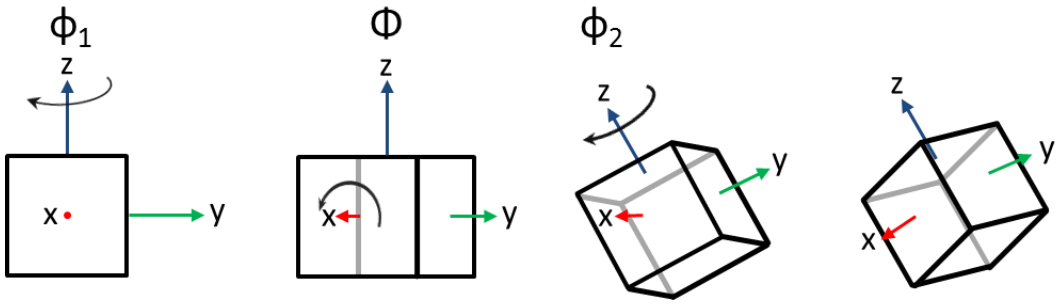

Figure 2.12: The three Euler angles used in the Euler angle convention. Adapted from [**41**]

Mean Angular Deviation

When the peaks on the Hough transformed EBSP are identified, they are compared with the peaks stored in the lookup table. The closest fit is used to simulate the Kikuchi bands and identified as the solution. The deviation between the experimental EBSP and the simulated EBSP is given by the Mean Angular Deviation (MAD). Lower MAD values indicate a better fit thus the solution that produces the lowest MAD is chosen as the correct one. For the experiments conducted in this work, only solutions that produced MAD of less than 1° were accepted. If the MAD was greater than 1°, the simulated EBSP was not accepted as the correct solution to the actual EBSP.

Band Contrast

Band Contrast (BC) measures the quality of the EBSP by quantifying the average intensity of the Kikuchi bands relative to the overall intensity of the EBSP. BC is scaled from 0 to 255 representing minimum to maximum contrast difference. That is, if the bands have a high intensity with respect to the overall intensity of the EBSP, the EBSP is of high quality and the BC would be a high value representing a high contrast. If the intensity of the bands is close to the overall intensity of the EBSP, the EBSP would be of poor quality due to its low contrast and would result in a low BC value.

Band Slope

Band slope (BS) is an image quality factor that describes the maximum intensity gradient at the margins of the Kikuchi bands in the pattern [**42**]. It is scaled on a 0 to 255 range describing a low

to high maximum contrast difference. A high quality EBSP has sharper Kikuchi bands which would produce a high BS value [**42**]. Since many factors can contribute to the variation in BC and BS values, such as defects inside a crystal, or even experimental conditions, these values are used only to determine the relative change in pattern quality.

2.4.2 Representation of Data through Pole Figures

As described above, in addition to the solution of the diffraction pattern given in Euler angles, other parameters, such as the pattern misfit (MAD) and patter quality factors (BC and BS), are also obtained from the experiment. All of these parameters can be used to gain more information on the crystal structure through various maps and figures. One of the methods used to represent the orientations of the sample is through the use of pole figures.

Pole figures are used to display the three dimensional orientation of the crystal in a two dimensional schematic. The goal is to transform the orientation of a single crystal, as shown by the cube in Figure 2.13a to a 2D pole figure. The first illustration in Figure 2.13a shows how the six {100} plane normals would project onto a sphere. The point where the normal of a plane intersects with this sphere is called a pole [**48**]. Figure 2.13b demonstrates the projection of the poles from this sphere onto a circle. Finally, in Figure 2.13c, the pole figure that represents the three dimensional crystallographic direction of a single crystal is shown. This process can be repeated with the orientations of other grains in the sample and all plotted on one pole figure to demonstrate the orientations or preferred direction in the sample [**41**]. For more details on pole figures of other methods of presenting the data refer to [**10**,**41**,**45**].

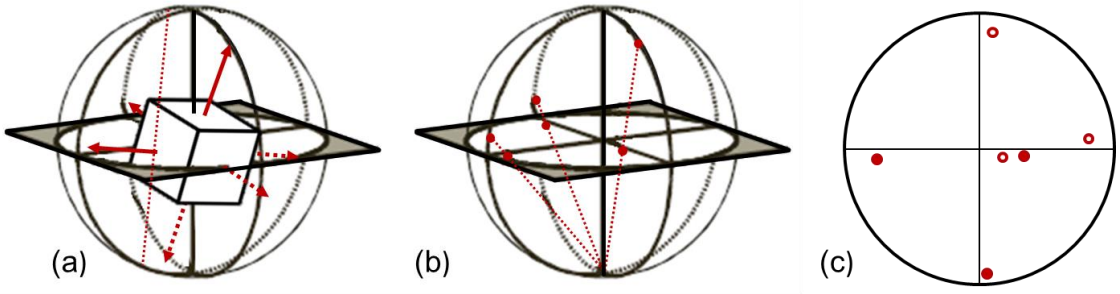

Figure 2.13: The projection of crystallographic plane onto a sphere (a), then onto a circle (b), to construct a pole figure (c). Modified from [**41**]

3. RESULTS

3.1 Location of the Beam

When conducting an EBSD experiment of nanostructures, the first major concern is to obtain a high quality of EBSP. The diffraction pattern can be indexed if the quality of the image is high enough for the computer to automatically detect the Kikuchi bands.

There are a few things that need to be taken into account once the sample has been prepared appropriately. First of all, it is important that there is a direct path between the interaction volume where the backscattered electrons are produced and the EBSD detector. If the nanostructures are too close and a direct path is not present, the diffracted backscattered electrons may not reach the detector, or the blocking object may cast a shadow on the detector. Even if the electrons reach the detector, the diffraction pattern may not be representative of the particular nanostructure where the beam strikes. For the gold nanoparticle (AuNP) samples studied in these experiments, since the nanoparticles are spread apart, this was rarely the case. For demonstration, the beam is positioned on the substrate such that an AuNP blocks a direct path to the detector in Figure 3.1a. Consequently, the lower half of the EBSP in Figure 3.1b has a distorted signal overlapped on the diffraction pattern from spinel. Thus the beam should always be positioned such that there are no obstructions in the direct path to the detector.

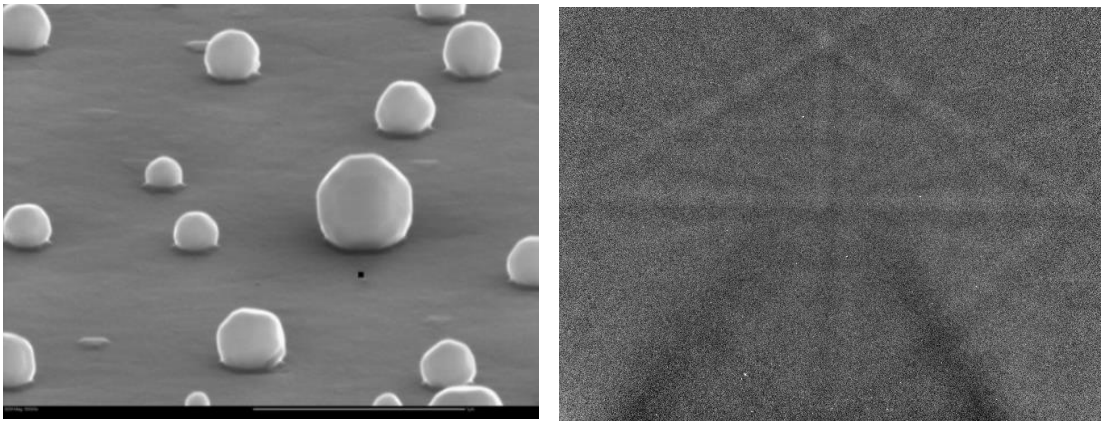

Figure 3.1: AuNP is blocking the signal from the substrate, thereby casting a shadow on the detector

Factors that affect the quality of the pattern generally include surface conditions, grains, and defects [**49**]. It will be shown in Section 3.2.1 that these well shaped nanoparticles are found to be single crystalline, thus for now it is assumed that the pattern quality will not be affected due to overlapping grains or defects. In this part of the experiment, the quality of the diffraction pattern, that is its intensity and contrast, will be studied in detail and the reason for variations will be discussed.

From experimentation it is observed that the quality of the diffraction pattern varies substantially depending on the location where the beam strikes the nanoparticle. To evaluate the change in quality of the diffraction pattern, the electron beam is directed at various points on the nanoparticle. All of this analysis, including the measurement, are performed at a 70° tilt and labelled accordingly. This is chosen as the reference since all the SEM images and EBSD measurements are performed at a 70° tilt (refer to Section 2.3.1 for details on the tilt angle). A nanoparticle that measures 280 nm from its top edge to the point of contact with the substrate at a 70° tilt is approximated as a sphere with a diameter of 280 nm. This sphere is shown in Figure 3.2 where the coordinate system for the experiment and the analysis is also shown. The x- and y-axis are the horizontal and vertical axes, respectively, on the nanoparticle, as shown in Figure 3.2b. The z-direction is labelled according to the beam, where the beam originates from the positive z-direction and propagates in the negative z-direction towards the nanoparticle.

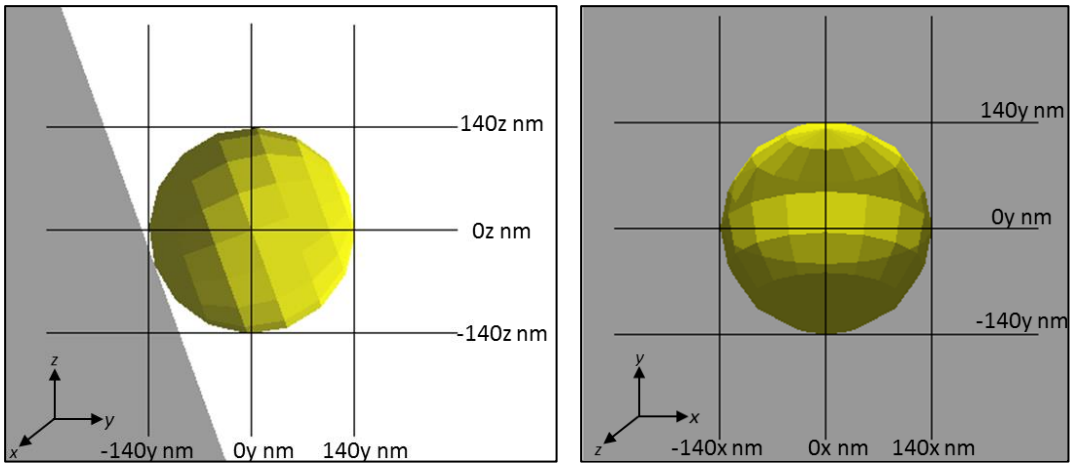

Figure 3.2: The coordinate system followed for the analysis where the beam impacts from z at the chosen x- and y- locations on the nanoparticle.

3.1.1 Scans along the y-axis

The center of the nanoparticle is labelled as 0 nm, the top edge as 140 nm and the bottom as -140 nm as shown in Figure 3.2. For this experiment, the beam is directed at several locations along the y-axis while the x-direction is kept constant at the center where x = 0nm. SEM image from this experiment is shown in Figure 3.3. EBSPs are obtained at the following locations:

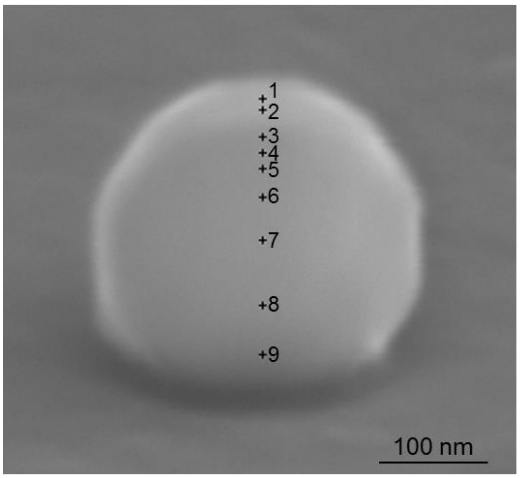

1. y = 130 nm ± 5 nm
2. y = 120 nm ± 5 nm
3. y = 95 nm ± 5nm
4. y = 80 nm ± 5nm
5. y = 65 nm ± 5nm
6. y = 40 nm ± 5nm
7. y = 0 nm ± 5nm
8. y = -60 nm ± 5nm
9. y = -105 nm ± 5nm

Figure 3.3: SEM at 70° tilt of a 280nm AuNP with all the locations for the y-scan marked on the nanoparticle. On the right, the locations are labeled according to the coordinate system described in Figure 3.2.

First three points are near the top of the nanoparticle, the next three points are probing the middle of the nanoparticle, and finally there are three points chosen in the bottom range[1]. These points are selected as they represent locations where noticeable changes take place in the EBSP over an AuNP. The beam resolution depends on the interaction volume which depends on the energy of the beam and the Z number of the sample. It is also dependent on the size of the beam spot which differs according to the SEM setup. The goal is not to calculate the beam resolution but to determine the accuracy of the position of the beam. The ±5 nm error in beam position was determined experimentally by probing the beam near the edges of the nanoparticle

[1] Top of the nanoparticle refers to the top most edge of the nanoparticle as imaged by the SEM at a 70° tilt. This edge is also the closest edge to the detector. The bottom edge is the edge that is in contact with the substrate and the farthest from the detector.

[2] The vertical streaks present in the EBSPs arise from the automated background correcting algorithm of

and within ±5 nm of the edge, it was observed that the diffraction pattern of Au is not clearly visible.

Figure 3.4 below displays the unprocessed and processed EBSPs from the first three locations of the nanoparticle. The top three EBSPs are raw patterns that have not been corrected for background. Directly below each raw EBSP is the corresponding processed EBSP which employs automatic and static background correction (refer to Section 2.3.2 for details on background correction methods). Figure 3.5 and Figure 3.6 are displaying EBSPs from the middle and bottom of the AuNP. The image quality factors Band Contrast (BC) and Band Slope (BS) are labelled at the bottom of each processed EBSP. As already described in Section 2.4.1, BC and BS are image quality factors where BC quantifies the contrast difference between the bands and the background and BS value indicates the sharpness of the bands, both on a scale of 0 to 255. A high quality pattern would have both high BC and BS values. Since many factors such as experimental setup and crystalline structure of the sample cause variations in these parameters [**10**], they are only displayed here to provide a relative comparison of pattern quality from one EBSP to another.

The change in pattern quality can be observed through visual inspection and quantitatively compared through the relative BC and BS values. Overall, it can be seen that the geometry of the pattern, which includes the width of the bands and the angles between the bands, remains the same. The geometrical features are related to the atomic arrangement inside the nanoparticle, and will be discussed in more detail in Section 3.2. Quality of the EBSP pattern is greatest in the top range (Figure 3.4), and generally decreases as the beam is moved lower. At y = 65 nm, shown in Figure 3.5b, a very interesting phenomenon takes place. Geometrically, EBSP has the same features as the ones preceding it. However, the intensity distribution is very different. The top of the EBSP contains the same diffraction pattern features as all the previous EBSPs, however, the bottom half of the EBSP has an intensity distribution that is opposite of what is expected; it contains dark bands with bright edges. In fact, regions with the highest intensities now have the lowest intensities. This is known as contrast reversal and has been observed in TEM, but uncommon in EBSD. As it can be seen, all the subsequent EBSPs from lower locations have reversed contrast. Contrast reversal was discussed in detail in Section 1.5.4.

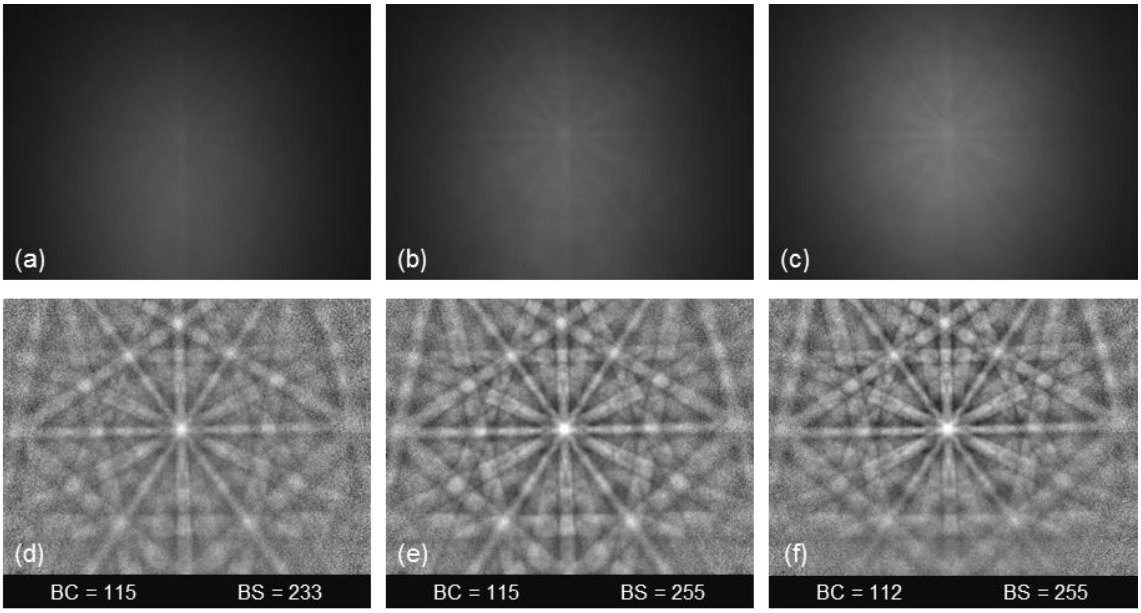

Figure 3.4: Raw and processed EBSPs with beam positioned near the top of the AuNP. Raw EBSPs at a) y = 130nm, b) y = 120nm, and c) y = 95nm with corresponding processed EBSPs shown in d), e), and f)

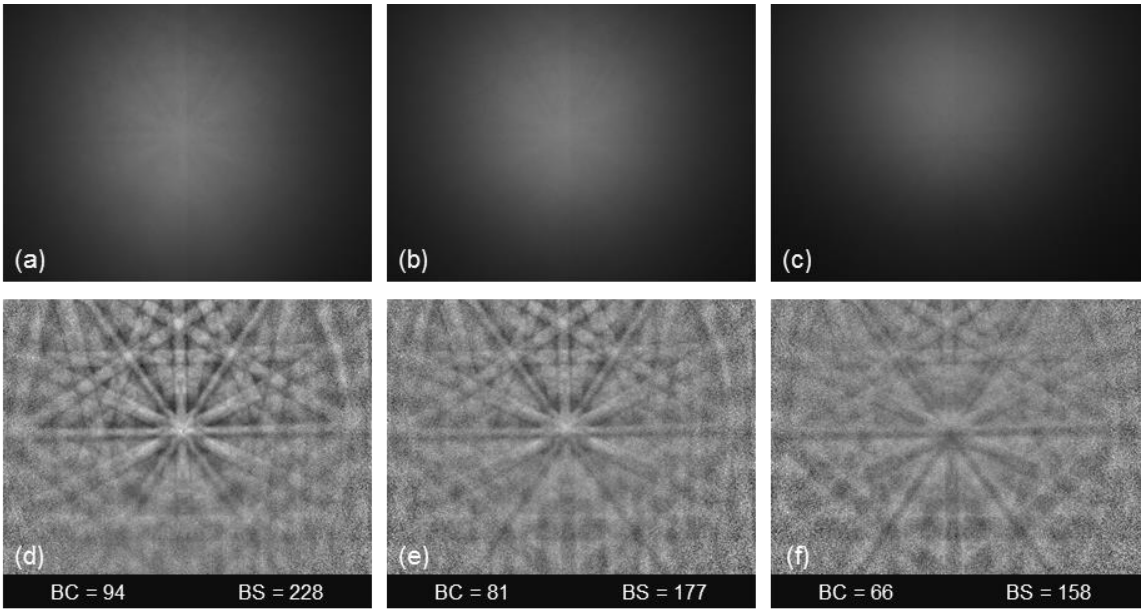

Figure 3.5: EBSPs when the beam is in the mid-range. Raw EBSPs at a) y = 80nm, b) y = 65nm, and c) y = 40nm and corresponding processed EBSPs shown respectively in d), e), and f)

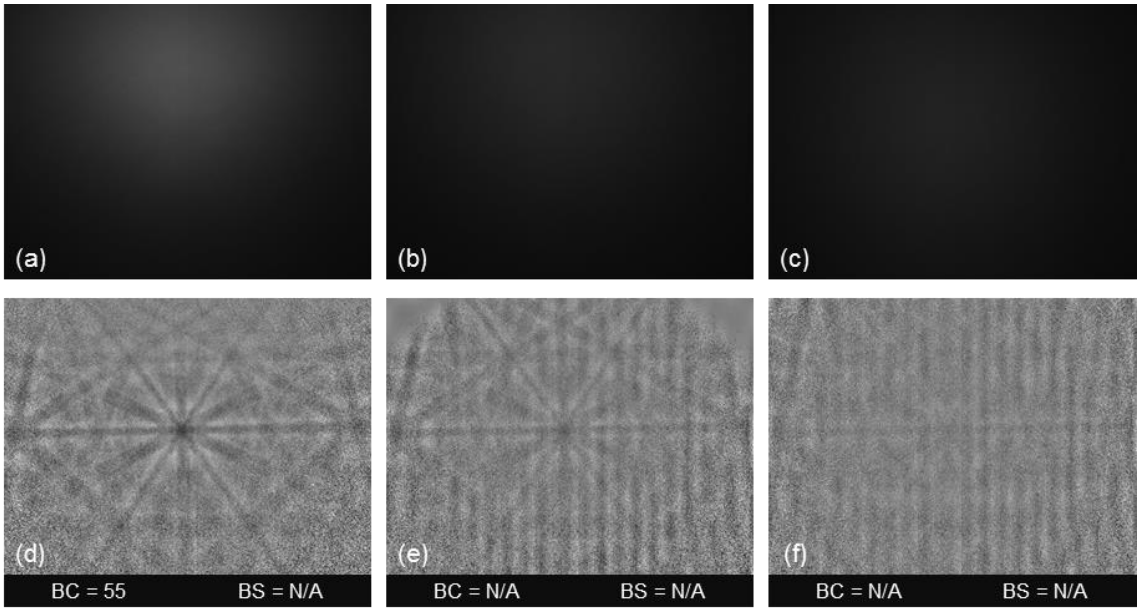

Figure 3.6: EBSPs from the bottom range of the nanoparticle. Raw EBSPs obtained at a) y = 0nm, b) y = -60nm, c) y = -105nm and d), e), and f) display the corresponding EBSPs respectively[2]

The reason behind the change in quality of EBSP must be related to the number of electrons reaching the detector. This intensity is especially comparable in raw EBSPs. It was discussed in Section 2.3.1 that the angular distribution of backscattered electrons is highly peaked in the forward direction approximately around the specular reflection of the incident beam [**13**]. The change in angular distribution according to this geometrical approximation is shown schematically in Figure 3.7 with the incident beam near the top, middle, and bottom of the nanoparticle. The points are not exactly in the middle and bottom since unique features are actually apparent at these approximate locations.

As it can be seen that the peak will approximately be just below the center of the detector when the incident beam is near the top of the nanoparticle, which is apparent by the intensity distribution of raw EBSPs in Figure 3.4. When the beam is probing the middle range of the nanoparticle, as seen in Figure 3.7, the peak of backscattered electrons will be just above the center of the detector. Raw EBSPs in Figure 3.5 also have peak intensity slightly above the center

[2] The vertical streaks present in the EBSPs arise from the automated background correcting algorithm of AZtec software

as expected. Finally, with the incident beam near the bottom of the nanoparticle, the local geometry between the beam and the nanoparticle is such that electrons are highly backscattered towards the substrate and thus raw EBSPs in Figure 3.6 have very low intensity.

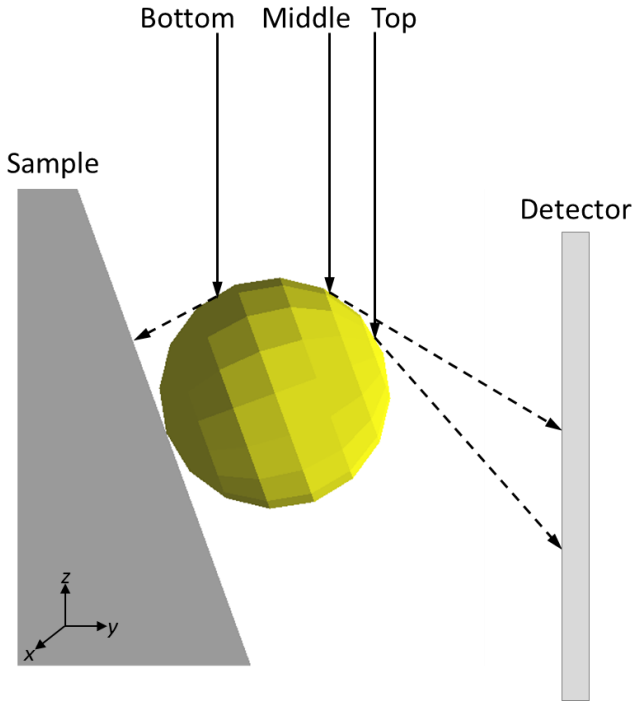

Figure 3.7: Schematic showing the approximate peak of backscattered electrons for the beam roughly positioned near the top, middle, and bottom of the nanoparticle.

To investigate further the reasons behind the changes in intensity and contrast of EBSP, electron interaction with the AuNP can be simulated through Monte Carlo simulations in CASINO. CASINO software calculates and displays trajectories that the electrons follow once the beam impacts the nanoparticle. Not only does it provide a visual representation of the interaction volume and angular distribution of scattered electrons, the data can be extracted for a set number of simulated electrons. The data contains all the details of the trajectories such as the position, directional vector, and energy of the electron, along with the collision type, scattering coefficients, and the energy distribution. From this data, if the position and directional vector of electrons are exported to a spreadsheet, it can be further analyzed to determine the angular distribution of scattered electrons. In other words, this information can be used to determine the percent of electrons that are in the solid angle of the detector and potentially contributing to

the final signal on the EBSP. Analysis of this data can be used to compare the amount of scattered electrons expected from each location of the beam. The location of the beam is referred to as 'scan point' in CASINO. The analysis primarily focuses on three scan points from the experiment: one from the top range, at y = 120 nm, one near the middle range at y = 65 nm and one from the bottom range at y = -60 nm. All of the points are located in the center along the x-axis, where x = 0nm. These points represent interesting and unique features and are sufficient to describe the trends and processes that take place over the entire y-range. Scan points, as selected in CASINO, are shown in Figure 3.8 below while the schematic displaying the setup in shown in Figure 3.9. Once the simulation runs, the image and the data can be readily exported. Running the simulation at these points produces the results shown in Figure 3.10. In these figures, 200 trajectories are displayed from the three scan points.

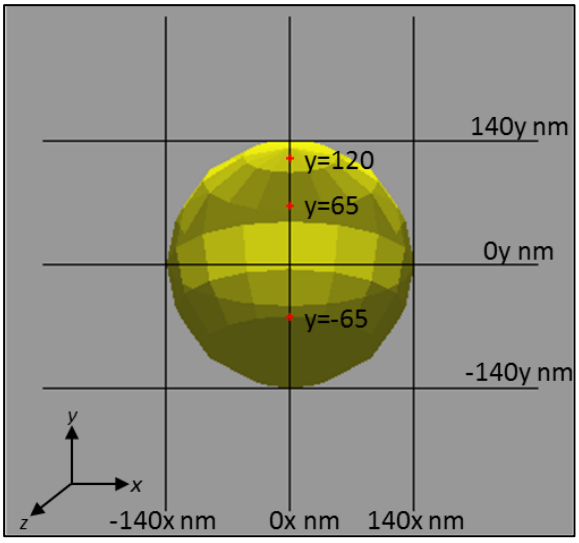

Figure 3.8: Scan points chosen on CASINO to match the location of the beam in the experiment. The points are located at the center (y = 0) and the x-coordinate of each point is labeled accordingly.

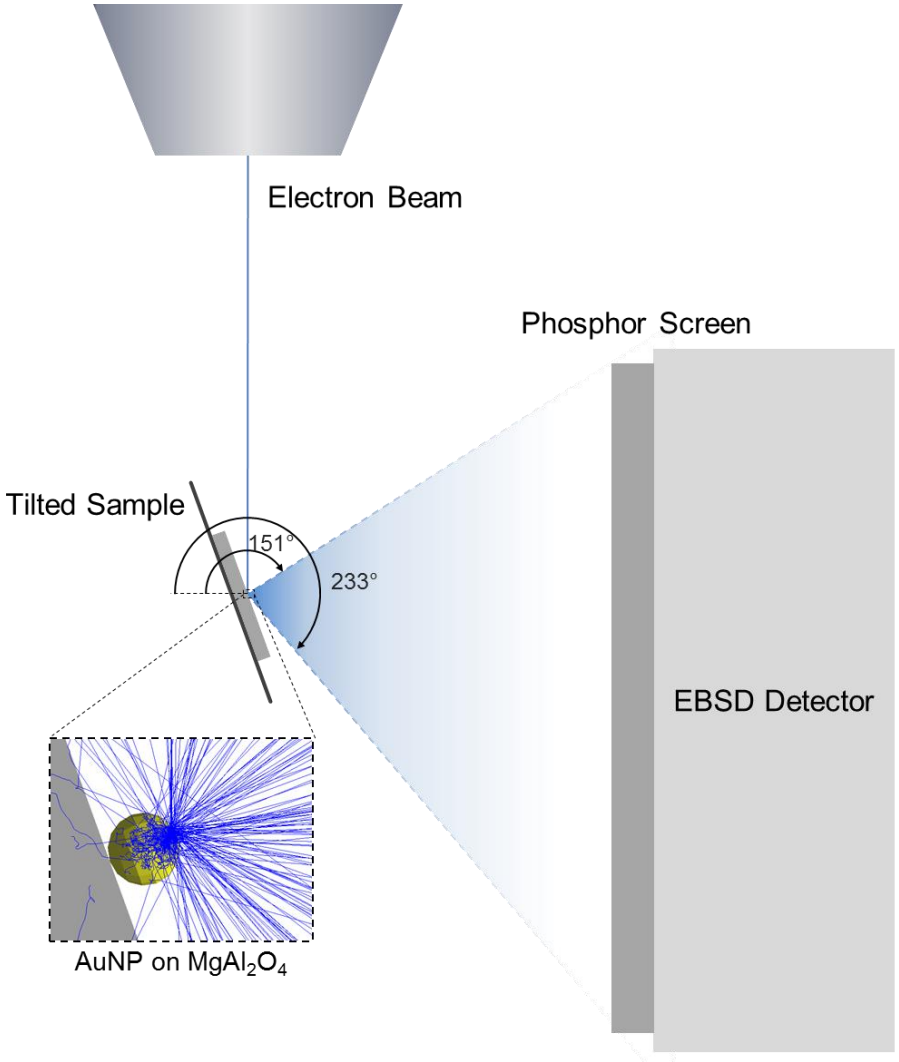

Figure 3.9: Schematic displaying the EBSD setup used in the CASINO model where the solid angle of the detector is labeled from 151° to 233°.

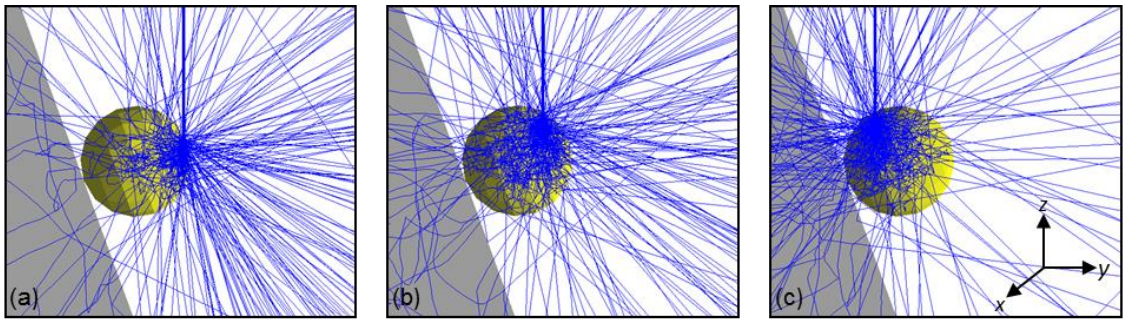

Figure 3.10: Monte Carlo simulations of 200 electron trajectories, shown in blue, from the (a) top, (b) middle, and (c) bottom of a 280nm spherical AuNP.

The data from these simulations is sorted and filtered in a spreadsheet. First, only 'region type' collisions are selected with energies below the beam energy (15 keV), ensuring that only the electrons that are escaping are kept for further analysis. Subsequently, all positions of trajectories that are outside of the range: -140<x<140, -140<y<140, and -140<z<140 are eliminated from the analysis as these represent electrons originating from elsewhere, such as the substrate, while only the signal originating from the nanoparticle is of interest. For example, from the simulation of 1000 electrons at y = 120nm, 845 are scattered back out from the nanoparticle.

In the experiment, since the x-axis is kept constant at the center where x = 0 and the nanoparticle can be approximated to be symmetric about the x-axis, x-values are not taken into consideration for the analysis. In other words, no limitations are set in solid angle of the detector in the x direction, and the comparisons will only be relative. The directional vectors in the y- and z-direction will determine whether the trajectories are in the solid angle of the camera. These values are analyzed and through simple trigonometric relationships, the angle of the trajectory is determined. Solid angle of the detector in the y-direction is determined from the geometry inside the chamber. Measuring the angle such that the beam is at 90° and the detector is at 180°, simple trigonometric relationships can be used to determine that the angular coverage of the camera is from 151° to 233° (Figure 3.9).

Data from the simulation of 1000 electrons from the three set points (top, middle, and bottom) is plotted in Figure 3.11. The scatter plot is a frequency distribution with a bin size of 10° and represents the number of electrons backscattering in a particular angular range. The data has been fit to a Gaussian distribution, which is represented by the solid curves on the graph. The area highlighted in yellow depicts the solid angle of the detector (from 151° to 233°). It is important to realize that the Monte Carlo simulations are simulating scattering of electrons from an amorphous AuNP. Thus no diffraction processes can be included. However, for the purpose of this analysis, it is sufficient to provide the description for the number of scattered electrons produced from these locations rather than focusing on the modulation caused by diffraction.

The red curve in the graph of angular distribution of backscattered electrons (BSE) in Figure 3.11 shows the angular direction of electrons when the beam is located in the top range of the

nanoparticle. The detector captures only the electrons that are scattered between 151° to 233° (highlighted in yellow). Therefore, to maximize the signal, it is necessary that a large number of electrons are backscattered in the solid angle of the detector. The peak of the red curve falls in this range. However, the number of backscattered electrons in the solid angle of the detector decreases when the beam is moved to the lower parts of the nanoparticle (shown by the blue and the green curve).

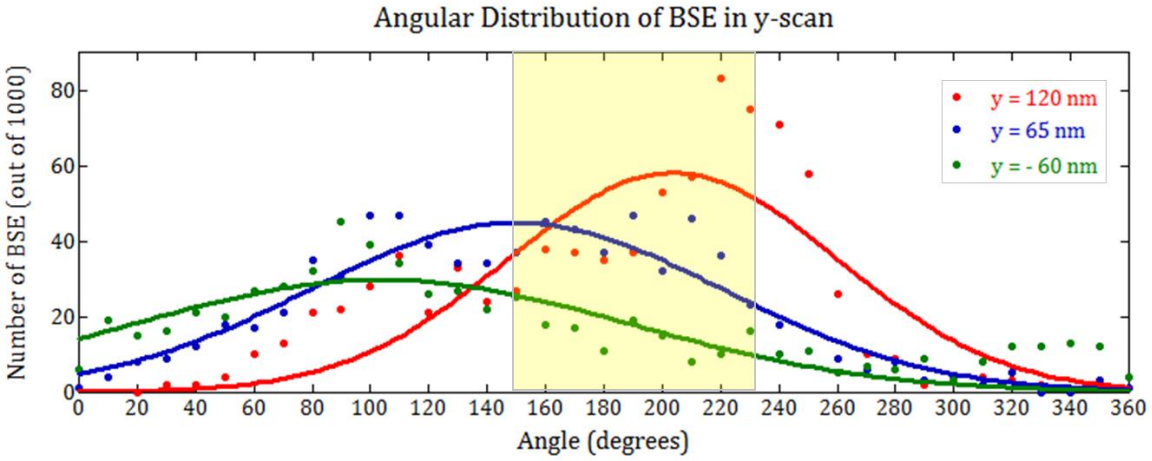

Figure 3.11: Angular distribution of electrons escaping the nanoparticle if the beam strikes at y = 100nm, y = 65nm, y = -60nm

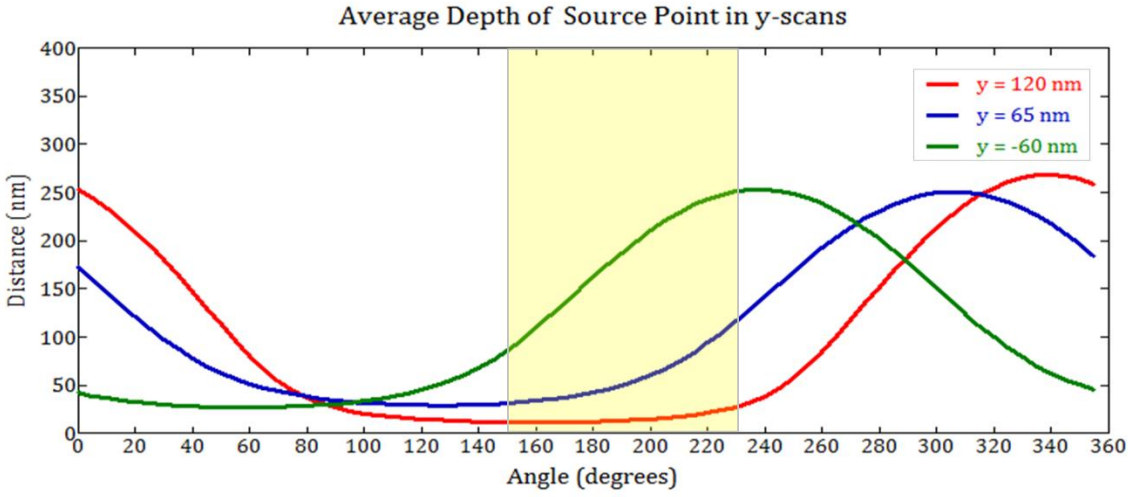

Figure 3.12: These curves represent the average depth of the source point from the surface of the nanoparticle. It effectively represents the depth from which the diffraction pattern originates

From this graph, it can be observed that the number of electrons scattered in the solid angle of the camera correspond directly with the quality (high intensity and high contrast) of the EBSP. When the beam is located at y = 120 nm, the EBSP is of high quality such that the bands can easily be detected, as shown in Figure 3.4e. The red Gaussian curve in the highlighted region of Figure 3.11 shows that in the solid angle of the camera, highest number of BSEs are produced when the beam is located in the top range at y = 120 nm. Similarly, with the beam located at y = 65 nm, the Gaussian distribution shows that a lower number of BSEs are produced in the solid angle of the detector. Correspondingly, Figure 3.5e shows that the image quality and contrast of the EBSP has depreciated. Finally, in the bottom range of y = -65 nm, Figure 3.6e shows the low contrast EBSP which corresponds to the lowest Gaussian curve in Figure 3.11, indicating a low number of BSEs in the solid angle of the detector. From these results, it can be concluded that a direct correlation between the production of BSEs in the solid angle of the detector and the intensity of the EBSPs exists. This method of calculating number of BSEs, however, does not directly relate to the contrast features of the EBSP as the electrons that are coherently diffracting and the electrons that are contributing to the background cannot be differentiated from this analysis directly. Thus this representation simply shows all the electrons with varying energies that would be backscattered from an amorphous spherical AuNP. Further analysis is necessary to understand the variation in contrast of the diffraction patterns, which is better depicted on the processed EBSPs. In addition, contrast reversal that occurs in some EBSPs is explained through the dynamic theory of diffraction, and thus cannot be directly obtained from the simple Monte Carlo simulations. However, since contrast reversal occurs due to anomalous absorption, which is dependent on thickness, a deeper understanding can be gained from calculating thicknesses.

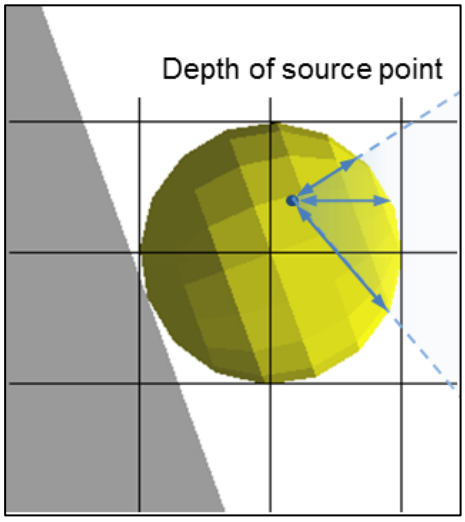

Figure 3.13: Schematic showing the depth of the source point, which is equivalent to thickness in EBSD, inside an AuNP at exactly 90° to the electron beam[3].

The thickness in this case is the average distance of the source point of BSE from the surface of the nanoparticle (shown in Figure 3.13), which can be calculated from the simulations. This distance indicates the depth of the source point which gives rise to the diffraction pattern. Since the quality of the pattern and the contrast fluctuate significantly as the location of the beam is altered, it is expected that it is the variation in thickness which contributes to the variation in pattern quality. Thus trends in these thicknesses can lead to the reasons for variation in the quality and contrast of the EBSPs. To calculate the average distance of the source point from the surface of the nanoparticle, mathematically, the problem is to simply calculate the length of a vector that connects the average initial position of the source to the surface of a sphere with radius of 140 nm in all directions. Thus the first step is to determine the initial position of the source point.

The diffraction pattern is produced from the interactions taking place inside the interaction volume. Since, of interest, is the average thickness, an average position can be approximated to one point (referred to as the source point) even though electrons are produced throughout the

[3] The thickness in EBSD is equivalent to average distance the electron travels inside the sample after it has been scattered. This is also referred to as the depth of the source point in this work. Note that this value is different from the penetration depth of flat samples which measures how far inside the sample the incident beam penetrates.

interaction volume. For the coordinates of the source point, the x- and y-coordinates are simply given by the location of the beam, or scan points in CASINO. To determine the position along the z-direction of the AuNP, average of the initial z-coordinate at the point of impact and an average of the final z-coordinate before the electron escapes the NP are calculated to define a range of depth. The midpoint of this range is chosen to represent the z-coordinate of the source point. Since the beam is kept constant at x = 0 amongst all the cases, the directional vector is sampled from 0° to 360° in the y-z plane to evaluate the variation in distances over the entire range. Due to the spherical symmetry of the particle, the graph of the thickness versus its angular direction forms a sinusoidal-like curve. These curves are graphed directly below the frequency graphs in Figure 3.12. The highlighted region in yellow illustrating the solid angle of the detector in Figure 3.12 corresponds to the blue shaded region in Figure 3.13. It can be observed from the graphs that an inverse correlation exists between the quality of the EBSP and depth of source point (or thickness of AuNP). At y = 120 nm, with a high-contrast EBSP, the curve shows a minimum thickness in the solid angle of the detector (10 nm to 30 nm) since the source point is located near the surface of the NP that is closest to the detector. Whereas, beam location of y = -65 nm results in a low contrast EBSP with the curve indicating a thickness range of 100 nm to 250 nm in the solid angle of the detector.

When the two graphs in Figure 3.11 and Figure 3.12 are compared, it can be seen that at angles where the source point is at a minimal distance from the surface (minimum thickness), the number of BSEs is high. Similarly, as the depth increases, the number of BSEs decreases. This is an expected outcome since the probability of absorption increases with increasing depth inside the material. These graphs not only show the amount of signal and thicknesses in the solid angle of the detector, but also the amount of scattered electrons and thicknesses in all other directions. This can be useful in determining the optimal placement of the detector.

For a more detailed comparison between the average depth of source point and the contrast of the EBSPs, in Figure 3.14, the average depths of the source point are graphed against the processed EBSPs for each location individually. It is expected that the depth of the source point is related to the diffracted signal on the EBSP which gives rise to the contrast of a diffraction pattern. By comparing these results, it can be seen that the number of electrons escaping from a

particular angle is related to the average thickness the diffracted signal must travel from the source point to escape, and consequently determines the amount of signal that reaches the detector. When these distances are short, a higher number can escape without being absorbed. However, as the depth increases, a higher number of electrons will get absorbed and as a result, fewer electrons escape and contribute to the diffraction pattern.

When the beam strikes the top of the nanoparticle (y = 120 nm), the interaction volume is near the top surface of the nanoparticle, which is closest to the detector and falls within its solid angle. Thus a high number of electrons are backscattered towards the camera as shown in the frequency distribution (red curve in Figure 3.11) obtained through the simulation. In addition, since these electrons are produced near the surface, the source point of the signal is close to the surface and diffracted electrons can escape easily. From the top graph in Figure 3.14, it can be concluded that short distances, in the range of 10 nm to 30 nm, produce the high contrast in EBSPs from top of the nanoparticle (Figure 3.4e).

In the mid-range (y = 65 nm), the beam creates an interaction volume that is farther from the top surface of the nanoparticle. This increases the depth of the source points. As this thickness increases, fewer electrons are expected to reach the detector since the probability of absorption increases. In addition to a lower number of backscattered electrons in the solid angle of the detector (blue curve in Figure 3.11), because the diffraction pattern is created deeper inside the nanoparticle, it will be largely attenuated before escaping the nanoparticle. Most of the Kikuchi bands with expected contrast are clearly visible until about 60 nm (see Figure 3.14), however, if the source point is any deeper, Kikuchi pattern of reversed contrasts are observed. The reverse contrast is apparent in the bottom of the EBSP in Figure 3.14.

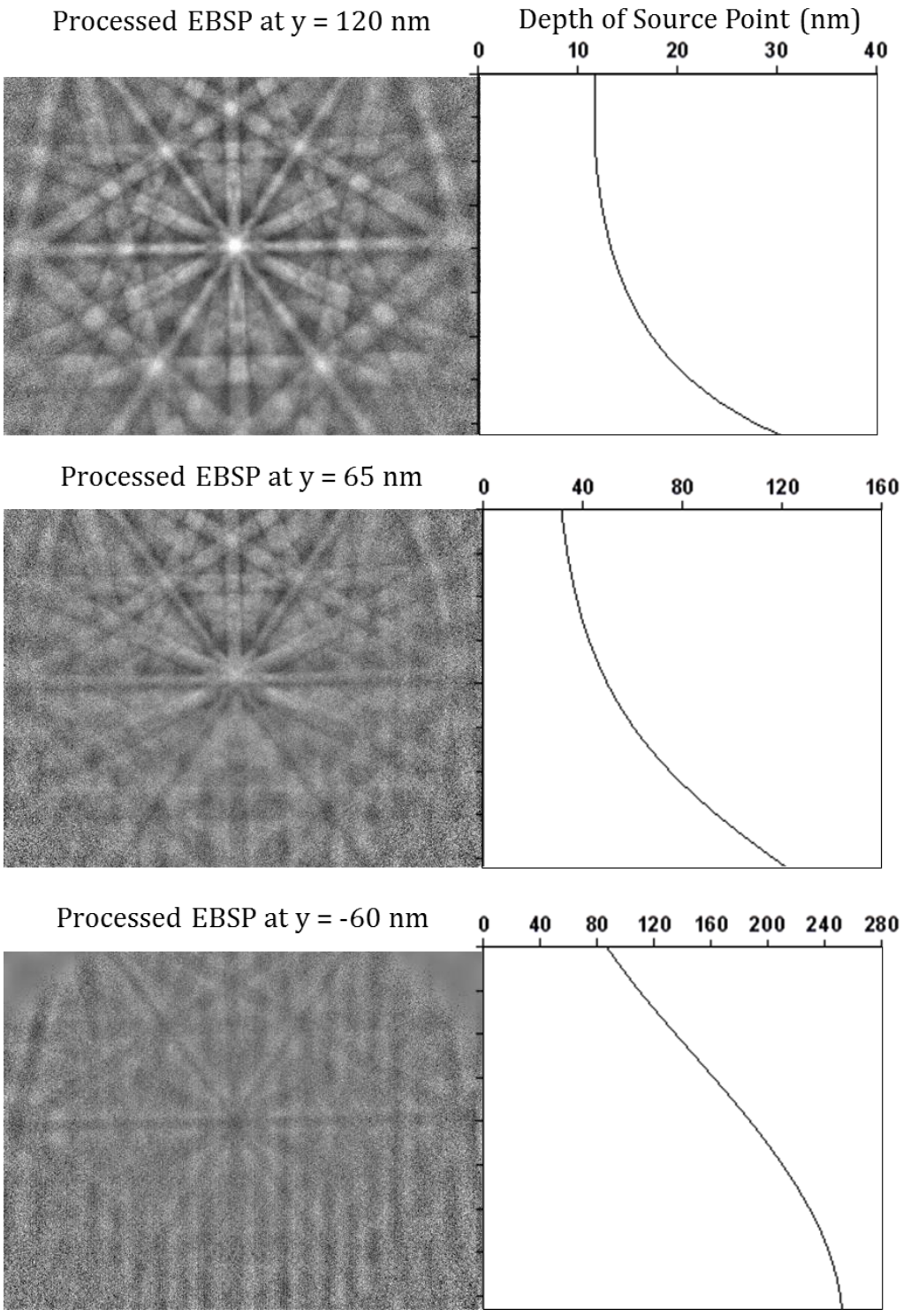

Figure 3.14: Processed EBSPs from the top, middle, and bottom of Au-NP marked according to the graph showing the average depth of the source point in each angular direction. The graph represents the changes in the diffracted signal on the EBSPs.

Finally, when the location of the beam is near the bottom of the nanoparticle (y = -60 nm), the number of electrons backscattered towards the camera is expected to be minimal, this is displayed by the green curve in Figure 3.11. The interaction volume is much farther from the top surface of the nanoparticle and most of the diffracted electrons will get absorbed before reaching the detector as they have to traverse the largest amount of material. With the geometrical relationship between the bottom of the nanoparticle and the incident beam, a high number of electrons will backscatter from the bottom of the nanoparticle; however, they will backscatter towards the substrate instead of backscattering towards the detector, and thus, will be absorbed by the substrate. Even though the source point is much deeper in the nanoparticle, EBSPs in Figure 3.6 show that most of the Kikuchi bands are still visible with reversed contrast. This signal is created by electrons that channel between the atomic planes and are not absorbed as much as the electrons travelling at the planes (discussed earlier in Section 1.5.4). From about 70nm to 200nm (see middle and bottom graphs in Figure 3.14), a reversed contrast Kikuchi pattern exists, however, after about 250 nm, majority of the bands disappear.

Graph in Figure 3.15 shows the percent of total electrons backscattered in the solid angle of the detector as the location of the beam is varied. This simulation result calculates electron trajectories for 1000 electrons from each scan point and percentage on the graph represents the percent of electrons scattered in the solid angle (151° - 233°) of the detector. The bottom of the nanoparticle that is in contact with the substrate is at y = -140 nm, the center is at 0 nm, and the top of the nanoparticle is at y = 140 nm. Best fit for the data is given by the Gaussian distribution, which is the curve superimposed on the graph. The trend here reiterates the fact that the number of backscattered electrons increases as the beam probes near the surface that is closest to the detector (the top surface). The amount of signal continues to decrease as the scan point moves further away from the top of the nanoparticle. The points located beyond y = 120nm do not follow this trend, however. From the Monte Carlo simulation, it is observed that due to the small interaction volume at these locations, not as many electrons are backscattered in the solid angle of the detector, instead they are forward scattered and exit at angles below the detector. This may also be the reason for the slight decrease is pattern quality in the EBSP from y = 130 nm, shown in Figure 3.4a.

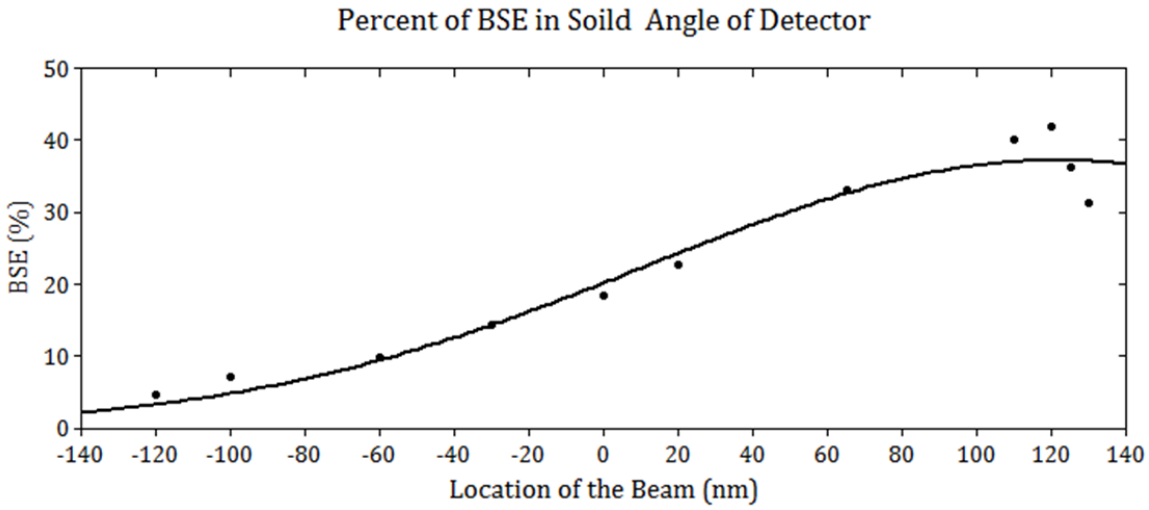

Figure 3.15: Percent of backscattered electrons in the solid angle of the detector versus the location of the beam on a 280nm spherical Au-NP. The quantities are obtained from Monte Carlo simulation of 1000 electrons in CASINO.

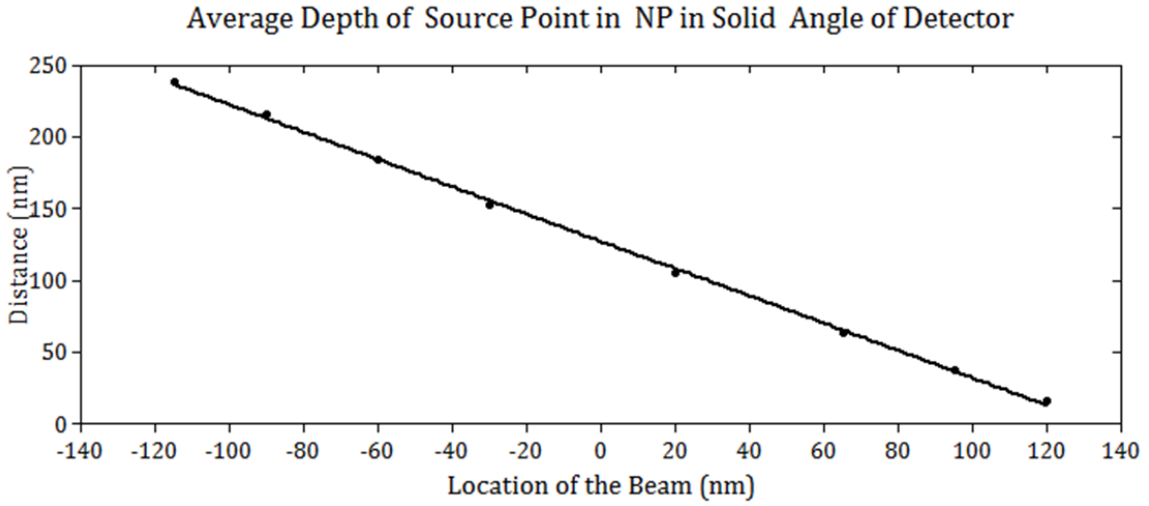

Figure 3.16: Average of the depths of source points in the solid angle of the detector versus location of the beam on a 280nm spherical Au-NP.

Figure 3.16 graphically displays the depth of the source point from the surface of the nanoparticle averaged over the angular range of the detector (151° - 233°) for each scan point. As expected from earlier results, the depth of the source point of the diffraction pattern in the solid angle of the camera is the lowest near the top of the nanoparticle. As the beam is moved lower, the interaction volume moves deeper inside the nanoparticle and farther away from the

surface from which it can escape to reach the detector. When the interaction volume is near the surface closest to the detector, the probability of electrons backscattering out of the surface is also the greatest and thus, from the comparison of the two graphs in Figure 3.15 and Figure 3.16, it can be seen that a beam located to produce lowest depths will generally correspond to highest number of backscattered electrons. From the experimental results, it can be concluded that this is the condition required to produce the highest quality of EBSPs – an overall high number of backscattered electrons with minimum thickness produces a high-contrast diffraction pattern.

3.1.2 Scans along the x-axis

Just as the beam was scanned in the y-direction while keeping the x-direction constant, EBSPs can also be studied in the x-direction while keeping the y-direction constant. The geometry and the chosen points are labelled below in Figure 3.20, with the SEM image of the nanoparticle shown in Figure 3.17. For x-scans, if y is set to 0 nm for symmetry and consistency, the diffraction pattern will resemble the EBSP shown in Figure 3.6d. At this low contrast, the changes in pattern quality and intensities are very difficult to observe. Instead y is set to a value that is expected to produce a higher contrast. From the previous experiment it was determined that high quality EBSPs are obtained when the beam is probing less than 70nm from the top surface of a nanoparticle. The location cannot be too close to the top of the nanoparticle as the radius in the x-direction will be too low. According to these parameters, y is chosen to be at y = 65 nm ± 5 nm. Four points are selected, two on either side of the nanoparticle:

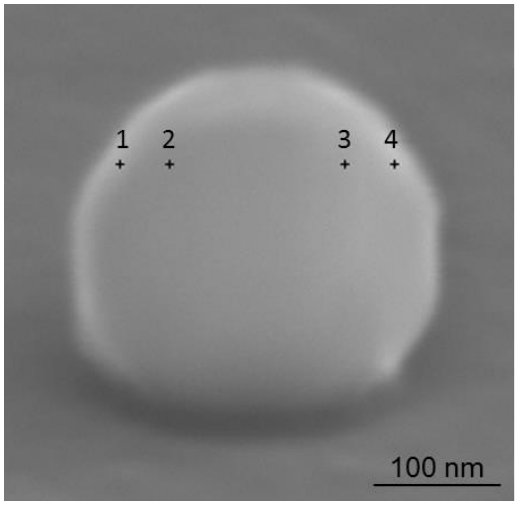

1. x = -115 nm ± 5 nm
2. x = -75 nm ± 5 nm
3. x = 75 nm ± 5 nm
4. x = 115 nm ± 5 nm

Figure 3.17: SEM image of Au-NP at 70° tilt with location of the beam marked for x-scans. On the right, the points are labeled according to the coordinate system described in Figure 3.2.

Unprocessed and the corresponding processed EBSPs are shown in Figure 3.18 below. The processed EBSPs use a dynamic automatic background correction only while static correction is not applied to save time. The image quality factors BC and BS are listed directly on each EBSP.

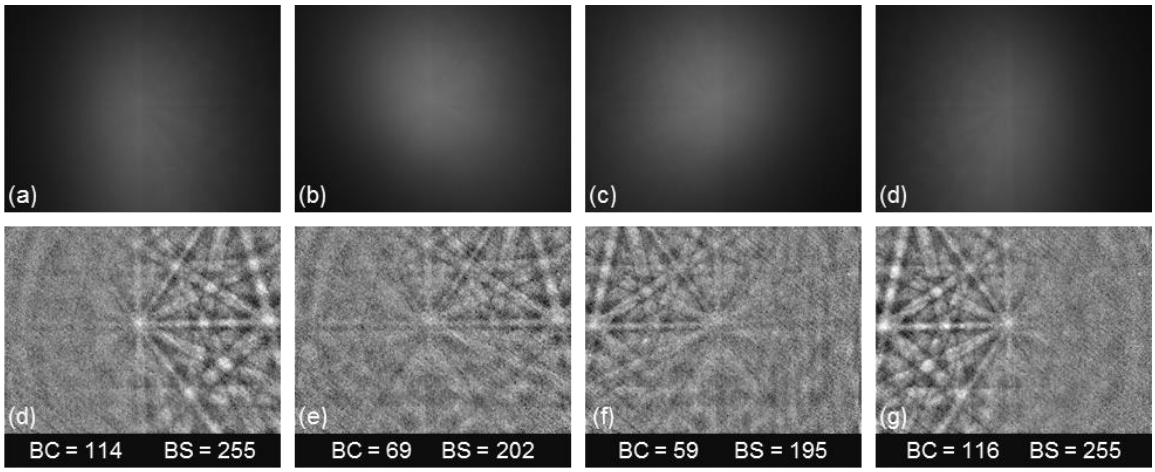

Figure 3.18: EBSPs from the x-scan of the nanoparticle at y = 65 nm. Raw EBSPs obtained at a) x = -115 nm, b) x = -75 nm, c) x = 75 nm and d) x = 115 nm are shown with the corresponding EBSPs in d), e), f), and g), respectively

When the beam is scanned in the x-direction, the results seem odd at first. However, after taking a closer look, all of the basic features can be understood. Once again the geometry of the Kikuchi bands remains the same, that is, basic orientation information can be attained easily. Intensity

distribution, on the other hand, of these patterns is very distinct. While one side of the pattern displays Kikuchi patterns, the other side is dark with no signal. The intermediate region once again shows reversed contrast of Kikuchi bands. When inspecting the other side of the nanoparticle, the intensities from left to right are generally reversed from right to left.

The overall intensity distribution can be understood through very simple observations. First of all, EBSPs are recorded on a screen, where the signal is parity inverted. This is to say that the orientation of the EBSP is upright; however, the image has been inverted left-to-right. The reason for the left-right inversion is due to the fact that the CCD camera is displaying the image as it is viewed from behind the screen. Thus in Figure 3.19, all the EBSPs are simply flipped about the vertical axis and displayed for a better understanding of the processes that are giving rise to such intensity distributions.

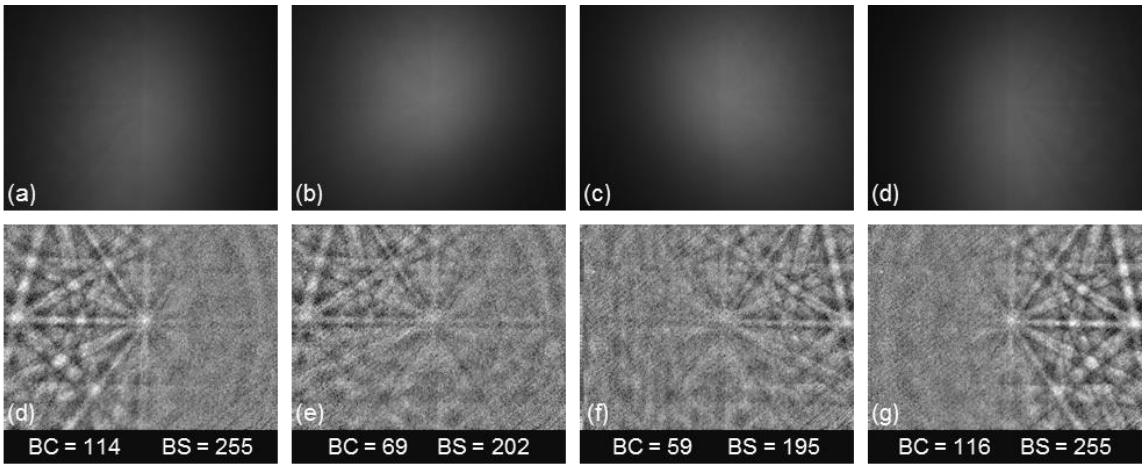

Figure 3.19: Vertically flipped EBSPs from the x-scan of the nanoparticle at x = 65 nm. Raw EBSPs obtained at a) x = -115 nm, b) x = -75 nm, c) x = 75 nm and d) x = 115 nm, flipped about the vertical axis are shown with the corresponding flipped EBSPs in d), e), f), and g), respectively

At this point, the signal begins to reflect the situation that resembles the y-scans, where at regions when the location of the beam results is a shallow depth of the source point, a high quality pattern is acquired. As the depth of the scan point is increased, the quality of the pattern depreciates. Once again, Monte Carlo simulations of these experimental parameters can be used to study the expected outcomes. Only two points, shown in Figure 3.20, (x = -115 nm and x = 115 nm) are analyzed, as one point from each side is sufficient to recognize the trends.

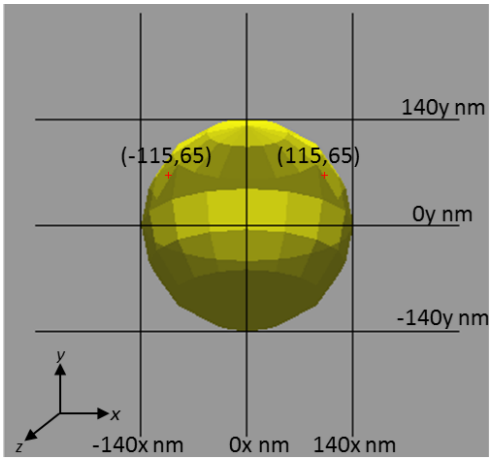

Figure 3.20: Location of the beam for x-scans shown in the CASINO model

Following the same procedure outlined above for y-scans, frequency distributions, shown in Figure 3.21, can be produced displaying the variation in the signal in the x-direction. Depth of source point in Figure 3.22 can also be obtained where variations in the x-direction are now included for the analysis. The position is determined using the same method as described in Section 3.1.1 and graphed against all possible angular directions of the trajectory.

Distributions in Figure 3.21 and Figure 3.22 echo the same trends obtained from the y-scans. Once again, not only the amount of signal in the solid angle of the detector is shown, but also the amount of signal expected in the other directions. The highlighted region in yellow depicts the angular range of the detector. The experimental results correspond with the results from the simulation, as expected from the previous section. From the left side of the nanoparticle (x = -115 nm), the EBSP in Figure 3.19d shows a high contrast on the left side of the EBSP but very low contrast of the right side. The red curves in Figure 3.21 and Figure 3.22 from 130° to 180° corresponds to the left side of the EBSP while the angular range from 180° to 230° matches the right side of the EBSP. From 130° to 180°, the red curve not only shows a high production of backscattered electrons, but a low depth of the source point, resulting in the high contrast on the left side of the EBSP in Figure 3.19d. In the angular range of 180° to 230°, the red curve shows a decreased production of backscattered electrons along with an increased depth of source point. This result corresponds to the low contrast seen on the right side of the EBSP in Figure 3.19d. The blue curves in Figure 3.21 and Figure 3.22 are related to the EBSP in Figure 3.19g. The blue curves are behaving in a method opposite to the red curves, which correctly

simulates the flipped intensities in the EBSP. Overall, in this geomtery, it is seen that the electrons scattering closer to the surface can escape and contribute to a signal on the screen. Electrons in the direction of the opposite side of the screen would have to traverse a larger thickness; however, since signals are attenuated at such lengths, as seen in y-scans, signal on the screen will be very low.

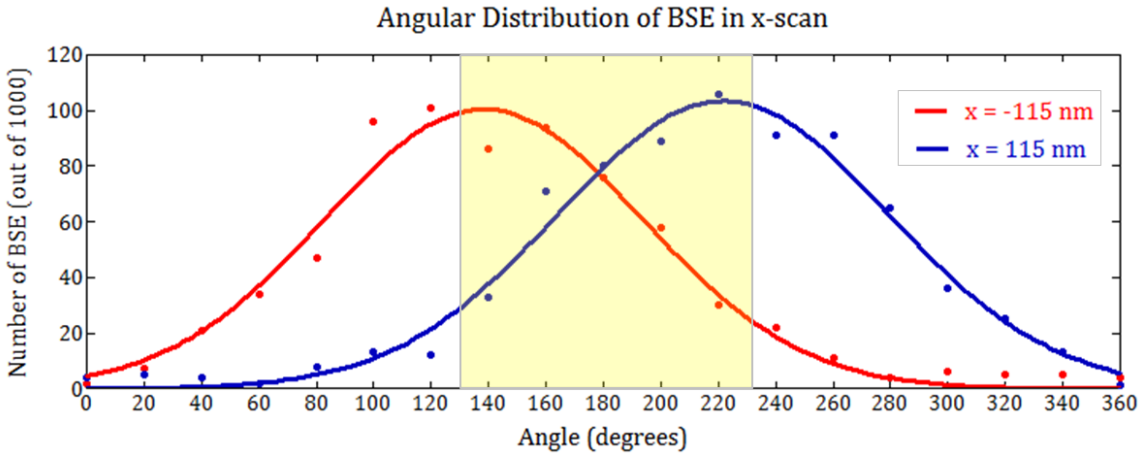

Figure 3.21: Angular Distribution of BSE in x-scans

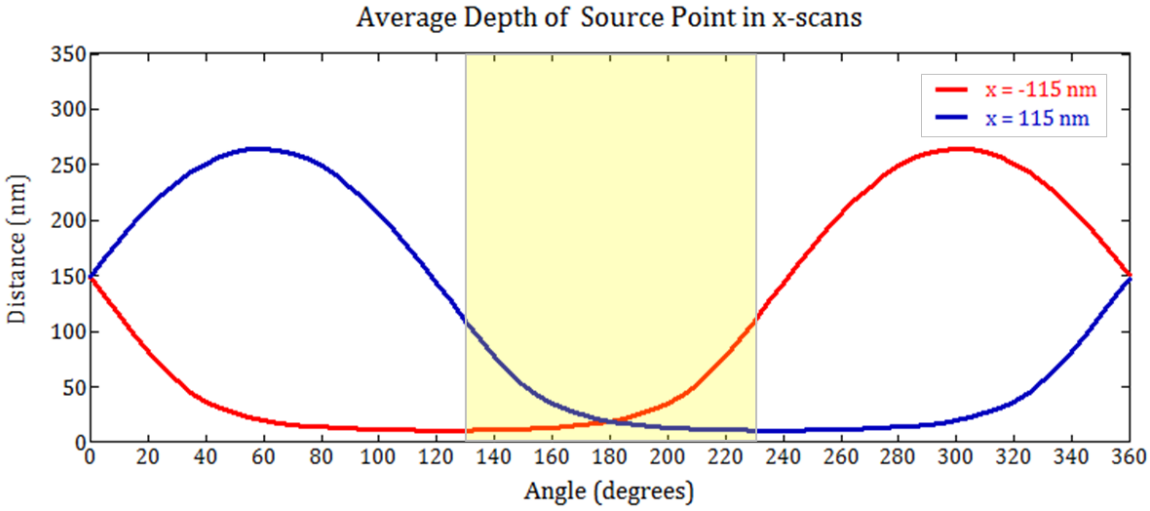

Figure 3.22: Average Depth of Source Point in NP

Processed EBSPs can once again be individually compared with the highlighted region of the average depth of source point. These representations are shown in Figure 3.23 for each side of the nanoparticle. As predicted, when the scan point is on the left side of the nanoparticle (x = -

115nm), the depth of the source point is at its minimum. These distributions shift to the other end as the other side of the nanoparticle is probed (x = 115nm).

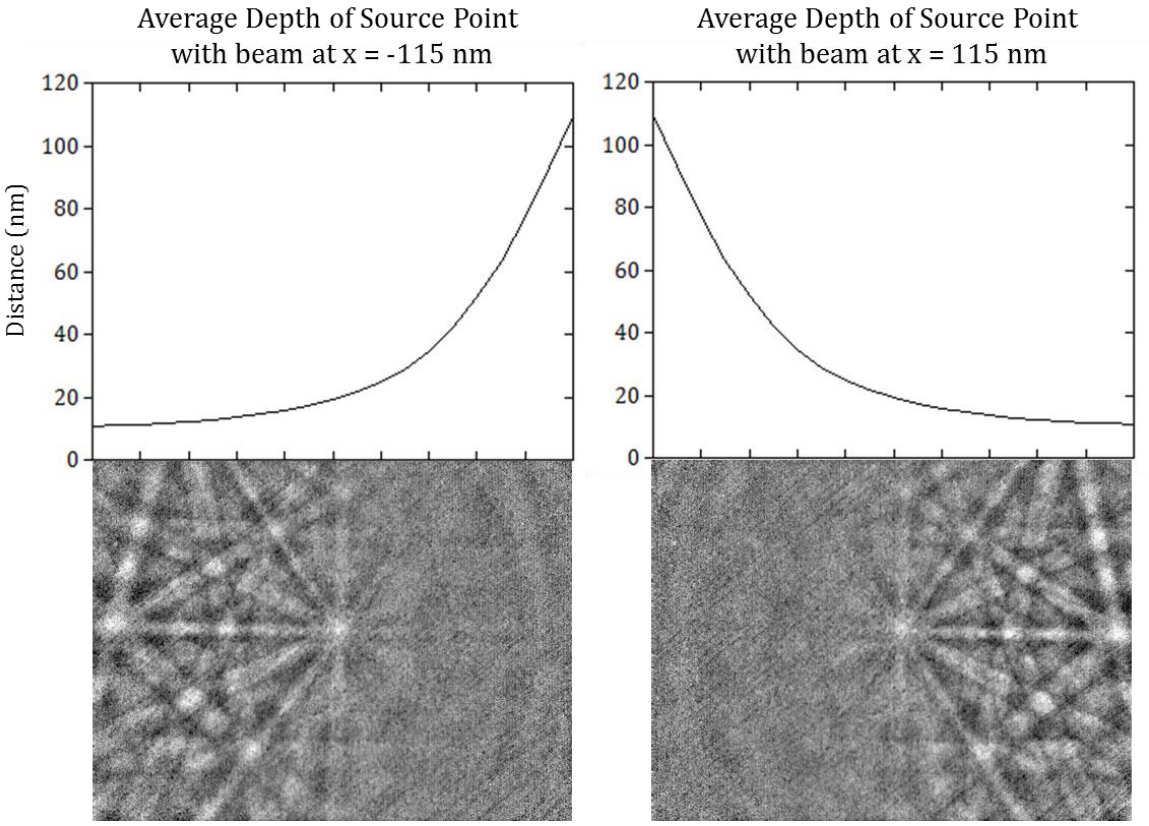

Figure 3.23: Processed EBSPs from the left and right side of Au-NP marked with the graph of average depth of the source point

From x-scans, it was seen that in the processed EBSP, bands are detectable on the side where the beam is close to the surface but not detectable on the opposite side. Although it can be observed from Figure 3.23 that on the opposite side when the depth of source point is between 40 nm and 120 nm, which is expected to produce a diffraction pattern, no bands are apparent on the EBSP. The reason for this disparity is revealed by the Monte Carlo simulation of angular distribution of BSE. In Figure 3.21, it can be observed that out of 1000 trajectories, less than 40 are scattered towards the opposite side of EBSP. With such a low number of electrons backscattering in the direction of the detector, raw EBSPs appeared dark (right side of Figure 3.19a). Thus the fact that no Kikuchi pattern is present on the opposite end of the EBSPs is not

due to the depth of the source point but instead it is the lack of backscattered electrons produced in those directions. Therefore it can be concluded from this discussion that short distances combined with high number of backscattered electrons produces the highest quality of EBSP, while large depths combined with low production of backscattered electrons results in little to no Kikuchi patterns.

3.1.3 Scan Through of a Small Nanoparticle

To bring the two types of scans together and present a complete scan-through, a small nanoparticle is probed. A 70nm high and 90 nm wide AuNP is chosen to be investigated since even if the beam is probing the bottom of the nanoparticle, the thickness will not exceed the limit at which Kikuchi bands are not visible. The beam is scanned through 12 points on the nanoparticle which are shown in Figure 3.24 and the corresponding EBSPs in Figure 3.25.

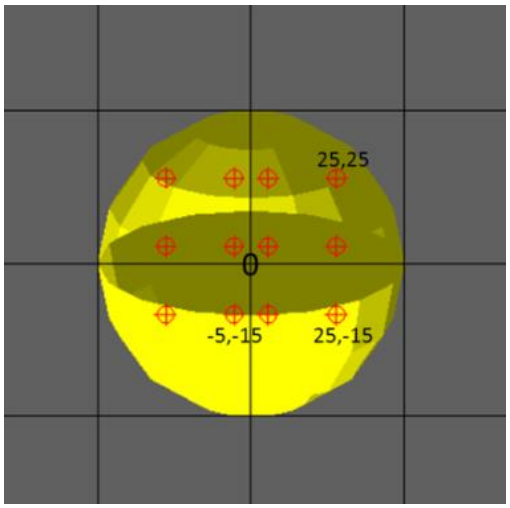

Figure 3.24: Schematic showing position of the beam, marked in red, on a spherical AuNP with a diameter of 90nm. Only the origin and three points are labeled with the coordinates as these will be analyzed later.

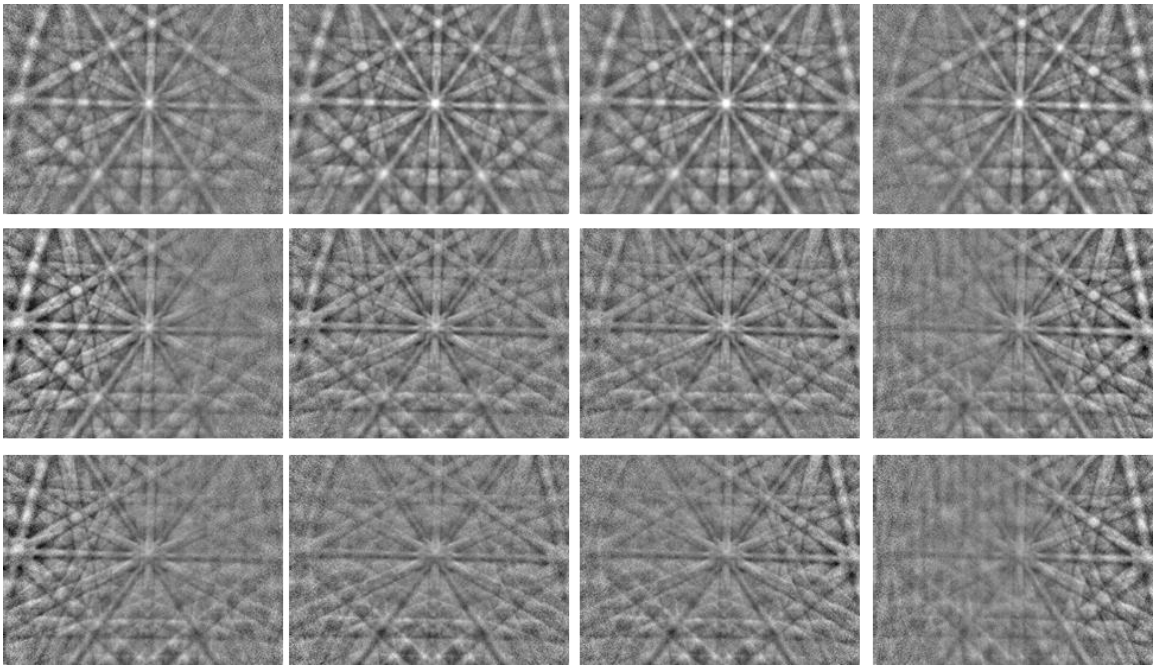

Figure 3.25: Processed EBSPs from the scan through of the small AuNP. The EBSPs have been vertically flipped according to the reasoning in Section 3.1.2. EBSP in the top left corresponds to the top left point in Figure 3.24 and the rest of EBSPs are aligned accordingly with the points marked in Figure 3.24.

In earlier scans, Monte Carlo simulations were used to determine the depth of the source point along only one direction, since the other direction was always kept constant. In this case, both of the x- and y-directions are varied along the nanoparticle and this variation is visible in the non-symmetric variation in intensity in the EBSPs in Figure 3.25. Therefore, instead of determining the depth of the source point along one direction only, the depth variation along all the angular directions over the EBSP is analyzed. This analysis is performed by first collecting the data from the simulation into a spreadsheet and then by graphing the results in a 3D graph in Prism.

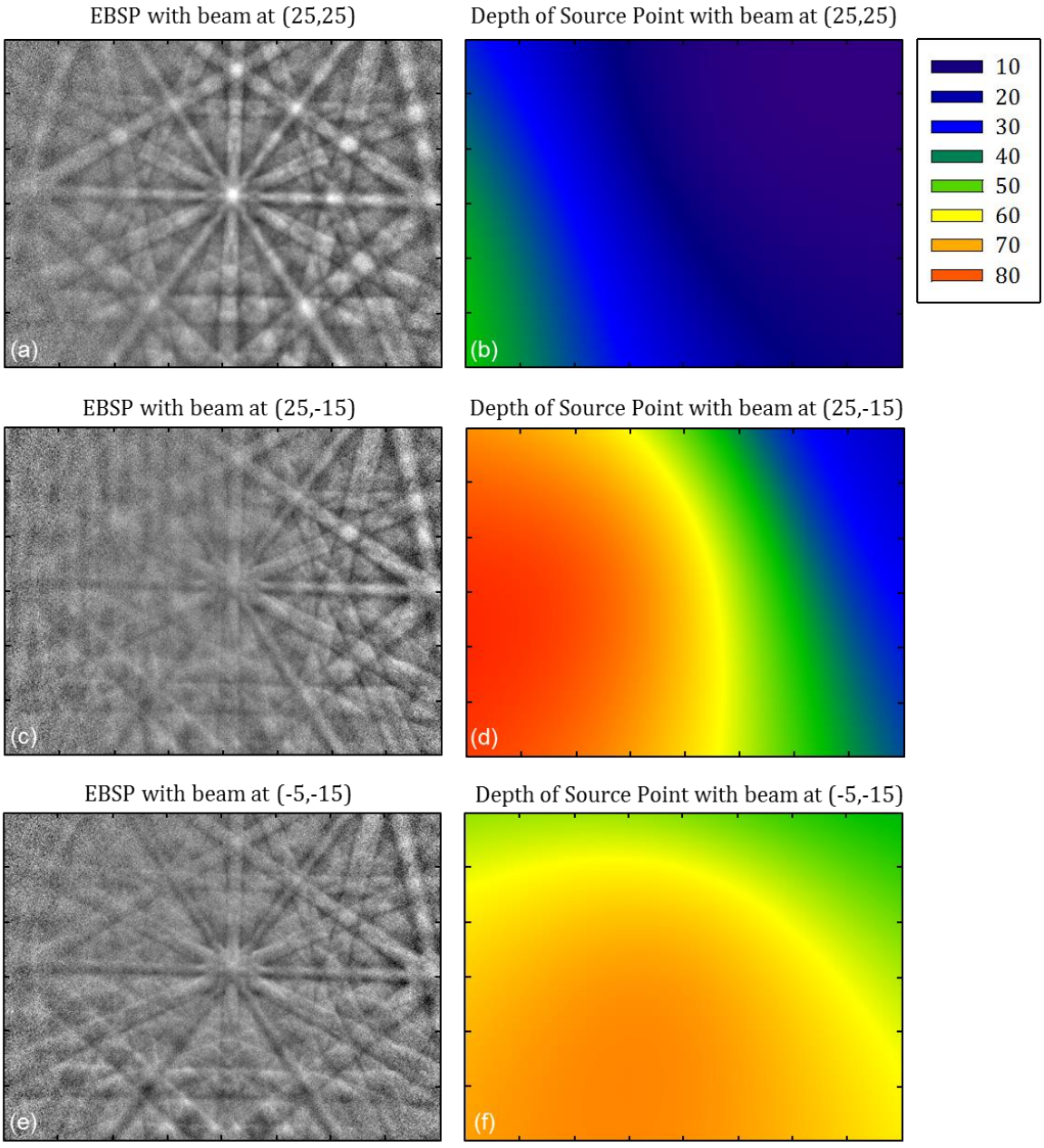

Figure 3.26: a), c) and e) display processed EBSPs from three different locations on a small AuNP while graphs in b), d), and f) shows the average depth of the source points in a 3D graph where the x- and y- axis correspond to the x- and y-axis of the EBSP and the color represents the depth, whose legend is shown on the top right.

Amongst all the evaluated points, three points that represent the different variations in intensity are chosen, where one is from the top corner, one from the bottom corner, and one from the

center. The EBSPs from the three points are shown in Figure 3.26a, c, and e while the 3D graphs of the average depth of source point from the simulation are displayed in Figure 3.26b, d, and f, respectively. The graph is scaled to match the size of the EBSP with each corner of the EBSP matching with each corner of the graph; however, the scale along the graph is arbitrary. The blue color on the graph depicts the regions where the depth is between 10 nm and 30 nm and at corresponding locations, the EBSPs are observed to have a high-contrast diffraction pattern. The green and yellow colors on the graph (40nm - 60nm) correspond to lower contrast of the diffraction pattern, while the dark orange and red (70nm – 80nm) correspond to the reversed contrast portion of the EBSP, especially apparent on the left corner of Figure 3.26c and Figure 3.26e. These values of depth match the values obtained in x- and y-scans of the 280 nm AuNP, and will be summarized later in Table 1.

Another interesting aspect of these 3D graphs is the formation of curves as the source of depth changes from one range to another. These transitions form curves as the nanoparticle is assumed to be spherical in the simulations due to the limitation of the software. The nanoparticle, however, is well faceted and has sharper edges. Thus if the contrast changes in an EBSP obtained can be quantified over the EBSP, the variation in contrast may be able to indicate the depth of the source. Graphing this distribution may result in information regarding the shape of the nanoparticle.

3.1.4 Intensity variation of EBSP and Depth Resolution

From the three types of scans, the range of thickness of AuNP that produces a certain type of intensity on the EBSP is listed in Table 1 below. In addition, the experiment is repeated with incident beam energy of 10 keV and 20 keV also and the thicknesses of AuNP at which all the major changes occur are also summarized in Table 1. Although absorption of electrons will vary according to each plane (e.g. with atomic density and d-spacing of the planes), the values above describe an approximate average with most of the bands having a particular type of intensity. In the first range, the volume of the NP interacting with the beam is so small that most of the electrons may scatter in a forward direction rather than backscattering towards the camera. The following range (10 nm – 30 nm for 15 keV) results in the highest quality of EBSP, because not

only does this volume produce a high number of backscattered electrons in the solid angle of the detector, the interaction volume is very close to the surface and the diffracted electrons can escape easily. As the beam probes farther down the NP, such that the thickness is approximately 30 nm – 70 nm for 15 keV, the contrast and quality of the EBSP depreciates. The interaction volume where the diffraction pattern is created is deeper inside the nanoparticle and thus some of the signal is attenuated before reaching the detector. From 70 nm to 200 nm for 15 keV, the interaction volume is so deep that Bloch wave 1 is completely attenuated; however, Bloch wave 2 electrons can still reach the detector, producing a reversed contrast EBSP. The Kikuchi pattern is still visible and detectable manually, since the software is not programmed to automatically detect reversed contrast EBSP. Beyond a thickness of 250 nm for 15 keV, most of the diffraction signal is absorbed resulting in almost no Kikuchi bands on the EBSP.

Table 1: The variation in EBSPs from AuNPs as the depth of the source varies. The approximate thickness at which all the major changes occur are listed for incident beam energy of 10keV, 15keV, and 20keV

Description of EBSP contrast	**Thickness (average depth of source point)**		
Energy of Incident Beam	**10 keV**	**15 keV**	**20 keV**
Volume is too low to produce a high number of BSE towards the detector	<5 nm	<10 nm	<10 nm
Highest quality EBSPs since interaction volume is close to the surface	5 nm - 20 nm	10 nm - 30 nm	10 nm - 40 nm
Quality of EBSP depreciates with thickness but easily detectable by the software	20 nm – 50 nm	30 nm – 70 nm	40 nm – 90 nm
EBSPs of reversed contrast	50 nm – 120 nm	70 nm – 200 nm	90 nm – 250 nm
Most bands disappear beyond this range	>180 nm	>250 nm	>280 nm

The trend as the incident beam energy is varied is apparent from the value listed in Table 1. At lower energy, 10 keV, the electrons will get absorbed more easily in a lower thickness. Thus the

range at which each intensity change takes place occurs at a lower thickness as compared to 15 keV. On the other hand, at higher energy of the beam, in this case 20 keV, electrons will be able to escape from even greater thicknesses. Therefore the ranges at which the intensity changes take place are higher than 15 keV. Although this result suggests that higher incident beam energy would produce a high quality of EBSP for a larger range, not only does the resolution of the beam decreases, but the sample may experience charging effects or get damaged by the beam. For AuNPs, 15 keV is determined to produce optimal results, as not only does it provide a sufficient range of thickness that produces high quality EBSPs, at this energy, the charging effects and beam damage are minimal.

Determining the depth resolution or in general determining the depth at which the diffraction pattern is assumed has been studied by multiple groups. Such work can not only lead to a better understanding of EBSD but eventually lead to more accurate models of EBSD. Alam et al. [**38**] in 1954 measured the changes in the Kikuchi patterns while changing the angle of incidence of the primary electron beam on the sample [**37**]. Changes in contrast were observed and linked to the fact that different depths are being probed at different angles. Winkelmann et al. [**37**] repeated a similar experiment with one small incidence angle (52°) and one large incidence angle (72°) on silicon at 20 keV. Similar observations in changes in contrast were directly linked to the fact that smaller angles cause the beam to penetrate deeper and thus the electron traverse a larger amount of material before exiting. At grazing angles, backscattered electrons are produced closer to the surface, thus the diffraction pattern is produced from a smaller effective thickness. To model the EBSPs from the two experiments, Winkelmann et al. assumed a depth from 0 nm to 40 nm for 72° and 45 nm to 60 nm for 52°. These depths resulted in good agreement with the experimental observations where contributions from the surface to a depth of 40 nm produced a high contrast Kikuchi pattern with excess bands and depths from 45 nm to 60 nm produced a Kikuchi pattern of reversed contrast. When comparing these results with the results obtained from AuNPs, there are two major differences that need to be considered. Since Winkelmann et al. experimented with a Si sample while the samples studied here are Au samples, the difference in the Z number [**13**], density [**13**], electron mean free path [**37**], and extinction lengths [**12**] will play a role in determining the depths which produce a change in contrast of EBSPs. The details of these parameters are not discussed here, however, it should be noted that due to these reasons

a direct comparison between the results would be an incorrect approach. Instead generally, it can be seen that the values obtained by Winkelmann et al. for Si at 20 keV that produce a high quality of EBSP (72°) are produced from electrons backscattered from the surface to a thickness of 40 nm while for AuNPs at 20 keV, the thicknesses that produce high quality also have an upper limit of 40 nm.

In 2010, Winkelmann [**28**] designed an EBSD model using the dynamical theory of electron diffraction to simulate diffraction patterns from molybdenum samples. To simulate the Kikuchi pattern, the contributions from sources at different depths need to be taken into account since backscattered electrons are produced in a range of depth. To account for this, Winkelmann assigned weights to each depth according to the relative number of electrons it scatters [**28**]. The results from the simulation of a total depth of 50 nm show that 80% of the total diffracted intensity is obtained from only the first 10 nm. This result is once again in agreement with the estimate of thicknesses in this work. It was observed in Figure 3.14a that the highest quality is produced when the thickness is near 10 nm and depreciates as the thickness increases. Once again, Mo and AuNPs cannot be compared directly, however, it can be seen that both of Winkelmann's experiments are in general agreement as they show that the pattern is mostly obtained from the first 40 nm of the sample (Si at 20 keV) where the first 10 nm produce 80% of the intensity in EBSP (Mo at 20 keV). While the range of thickness in Table 1 also indicates that the highest quality of EBSP is obtained within the first 40 nm of the sample and Figure 3.14a shows that EBSPs of high contrast are obtained when the thickness is near 10 nm.

Another method of approximating the thickness in EBSD (distance that diffracted electrons travel inside the material before exiting) was used by Dingley in 2004 [**50**]. According to Bragg's law, a Kikuchi line would be sharp and have a unit thickness if the energy of the incident wave is exact. However, the incident wave has a range of energy, thus the diffracted line will have a proportional width. Dingley [**50**] measured the width of a line in a high quality diffraction pattern and assumed that the line broadening is produced only due to the energy spread, where the line width was equivalent to an energy spread of 250eV. The distance that the electrons must travel in Si before losing more than 250eV is less than 40 nm [**50**]. Therefore Dingley also concluded that the EBSPs originate from a small volume that is 10 nm to 40 nm from the surface of the

specimen [**50**]. These values, once again, are in agreement with the thicknesses estimated in this work.

Finally, Zaefferer in 2007 [**36**] studied depth resolution of EBSD through deposition of amorphous layers of chromium on a Si sample and observing the EBSPs at 15 keV. The results show that with Cr layer thickness of 8 nm, no bands appear on the diffraction pattern. Zaefferer determined that only half of the original intensity is left with Cr layer thickness of 2 nm while only 10% of the original intensity is left with thickness of 5.5 nm [**36**]. These values, defined as the depth resolution, are considerably lower than the depths obtained from this work. The flaw with the method used by Zaefferer is that the amorphous Cr layer would first of all reduce the penetration of the beam inside the sample as Cr has a Z number of 24, a density of 7.14g/cm^3 and the layer is amorphous rather than crystalline. The high Z number of Cr (24) compared to Si (14) and the high density of Cr (7.14 g/cm^3) versus Si (2.33 g/cm^3) means that the beam will not be able to penetrate as deep in Cr as it would in Si [**13**]. Also, in a crystalline material, the beams propagate as Bloch waves and can cover longer distances; however, this affect will not take place in an amorphous layer. In addition, not only does the beam penetration of the incoming beam reduce, the outgoing diffracted beam will be attenuated due to the same reasons. Thus predicting depth resolution or the depth in the sample which produces the signal through deposition of amorphous layers may not be a very accurate method. It can be seen that the values obtained by Zaefferer may be much lower than the actual depth of the source. Instead, when studying the depth of the source with AuNPs, there are no such challenges, thus the values can be predicted to be closer to the actual depths.

3.2 EBSD Analysis of Nanoparticles

In the previous section, only the intensity of the EBSPs was explored, without any consideration towards the geometry of the resultant patterns. The intensity is an important component since high contrast is needed to automatically detect Kikuchi bands, but it is the geometry of the pattern that contains the most significant information about the sample. The geometry of a Kikuchi pattern includes the width of the bands and the angles between the bands. As discussed earlier in Section 1.5.2, the width of the bands and the angular relationships between them are

measured to determine the orientation of the crystalline structure, a process known as indexing. The EBSD software automatically detects the bands and indexes the pattern.

3.2.1 EBSD of individual AuNPs

The goal of this section is to study individual nanoparticles to determine whether AuNPs are single crystalline or polycrystalline. To conduct this experiment, the beam voltage is set to 15 keV and other parameters are adjusted to produce a high quality EBSP such that it can be indexed automatically. Few nanoparticles of varying sizes are chosen on the sample for this experiment. To determine the crystalline structure of an individual AuNP, the beam needs to probe its entire surface. To accomplish this, the beam is scanned from the top of the nanoparticle to the bottom of the nanoparticle as seen in the y-scan in Section 3.1.1 and from side to side as shown in the x-scans in Section 3.1.2. This allows the entire surface on one side of the nanoparticle to be indexed. To probe the other sides, the sample is rotated 90° clockwise about the tilted z-axis (Figure 3.27) and scanned in a similar fashion. The sample is rotated 90° clockwise about the tilted z-axis again and the beam is scanned similarly. One final equivalent rotation ensures the entire surface on all sides of AuNP has been probed. This method of studying the crystalline structure of individual nanoparticles is repeated for a set of AuNPs.

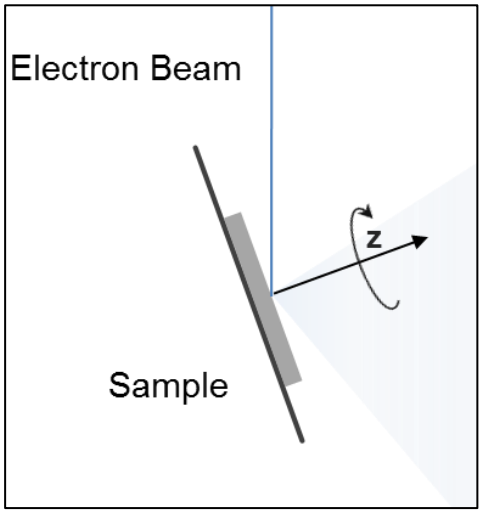

Figure 3.27: Rotation of the sample about the titled z-axis.

The resulting pattern is indexed, which reveals the crystalline structure from the surface of the interaction volume. To quantify the variation in the crystalline structure, a misorientation angle, which describes the orientation of the gold nanoparticle with respect to the orientation of spinel, is used. This angle is calculated by the software between the substrate and the gold nanoparticle about the common crystallographic axis. If the misorientation angle between spinel and gold nanoparticle remains the same, it would indicate that the crystalline structure of the nanoparticle is same over all of its probed surfaces and the nanoparticle is single crystalline. If it varies, the variation would indicate that the AuNPs may be polycrystalline.

At the first location (0° rotation), the first nanoparticle that is probed is the one studied in Section 3.1 (Figure 3.3) and it can be observed in EBSPs in Figure 3.4, Figure 3.5, Figure 3.6, and Figure 3.18 that although the intensity of the EBSPs varies significantly, the geometry remains constant. The high contrast in EBSP's from top of the nanoparticle allowed for the computer to detect the bands automatically, whereas the intensities from the bottom of AuNP were too low for automatic detection of Kikuchi bands. Instead, the user manually selected the band edges as they are visible to the naked eye, which then enabled the computer to index the pattern. For quantitative analysis, the EBSPs are indexed and the misorientation angles relative to spinel are calculated through the EBSD software. The average misorientation angles from all the data points on one side (0° rotation) of the nanoparticle along with the error from the standard deviation are shown in Table 2 below. For example, with (111) spinel orientation, AuNP (labelled "1" in the table) is also (111)-oriented but with an approximately 60° in-plane rotation. From indexing of EBSPs, the average misorientation angle is calculated to be 59.3° with a standard deviation of 0.2°. When the sample is rotated 90° clockwise about the z-axis to inspect another side of the nanoparticle, the misorientation angle relative to the substrate is 59.4° ± 0.2°. The sample is rotated two more times and the misorientation angles (listed in Table 2) from all the rotations are observed to have a deviation of less than ±1°. From these results, it can be seen that all the surfaces that were probed have the same crystalline structure and thus it can be concluded that the surface of the nanoparticle must be single crystalline. The same experiment is repeated for several nanoparticles over the sample and the results in Table 2 show that the orientation of the AuNPs with respect to the substrate remains the same over the entire surface of the nanoparticle and consequently all these faceted nanoparticles are single crystalline.

It was assumed in Section 3.1 that the crystalline structure of the nanoparticles is not the reason behind the variation in the quality of EBSPs. If the AuNPs were polycrystalline, overlapping pattern from multiple grains would produce a low quality pattern. In addition, slight shifts in crystalline structure would produce low quality EBSPs. It is shown here that these nanoparticles are single crystalline along the whole surface with less than 1° variation. Thus the assumption that factors affecting the intensity and contrast of the EBSP are related to the location of the beam on the nanoparticle and not the crystalline structure of the nanoparticle in Section 3.1 is justified.

Table 2: Misorientation angles of nanoparticles with respect to the substrate at four different rotations

Nanoparticle	0° rotation	90° rotation	180° rotation	270° rotation	Average
1	59.3 ± 0.2	59.4 ± 0.2	59.3 ± 0.1	59.2 ± 0.2	59.3 ± 0.7
2	0.3 ± 0.1	0.3 ± 0.1	0.3 ± 0.2	0.4 ± 0.2	0.4 ± 0.6
3	59.5 ± 0.4	59.2 ± 0.2	59.4 ± 0.1	59.0 ± 0.2	59.3 ± 0.9
4	59.5 ± 0.2	59.5 ± 0.1	59.0 ± 0.3	59.6 ± 0.3	59.4 ± 0.9
5	59.1 ± 0.2	59.4 ± 0.2	58.2 ± 0.2	59.6 ± 0.2	59.1 ± 0.8

3.2.2 EBSD analysis of the whole Sample

Since it is recognized from Section 3.2.1 that AuNPs of the high temperature sample are single crystalline, only one point on each nanoparticle needs to be indexed to obtain its crystal orientation. This allows many nanoparticles to be studied at once while still being able to distinguish them individually. From the previous set of experiments (Section 3.1), it was determined that the highest quality of EBSP was obtained when the beam is scanning the top of the nanoparticle where the local geometry between the nanoparticle and the beam is similar to that of a flat sample (near 70°) and a high number of diffracted backscattered electrons can escape the sample towards the detector. Since only one point is required to be indexed and a high quality pattern provides the quickest and most accurate result, one point near the top of each nanoparticle is indexed.

In 2DXRD, an average of the crystal orientation of the whole sample is produced. In TEM, on the other hand, even after meticulous sample preparation, minimum number of nanoparticles can be studied at a time. EBSD provides a method of studying individual nanoparticles on the substrate and with its speed and ease of sample preparation; the whole sample can be studied at once. This is very useful as not only can the orientations of the whole sample be studied to see the preferred orientations, but also, orientation of individual nanoparticles can be studied to see how the orientation varies from one nanoparticle to another. Distribution, shape, and size can be related to the crystallographic orientation of the nanoparticle.

The first sample for the EBSD analysis is the sample that was annealed at high temperature with well faceted nanoparticles and has been the focus of study throughout this work. 2DXRD analysis from Majdi's work [**1**] is used to compare the data acquired from the EBSD analysis. The results from the 2DXRD analysis of the whole sample are plotted on a (111) pole figure in Figure 3.28b along with the pole figure from only the substrate in Figure 3.28a [**1**].

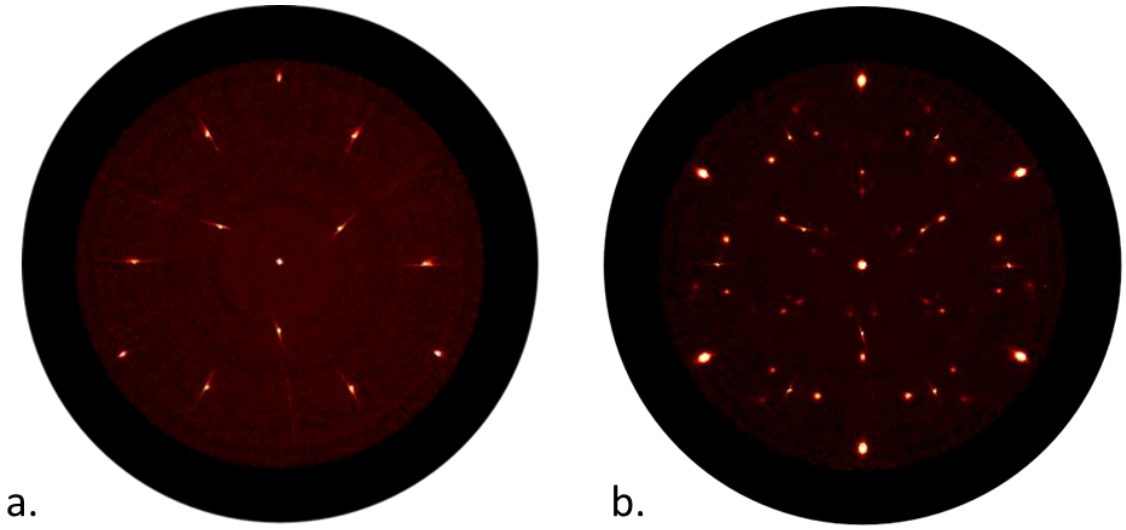

Figure 3.28: (111) pole figures from 2DXRD analysis of a) only Spinel and b) Sample 1 with well faceted AuNPs overlapped with the poles from spinel [**1**]

The pole figure of the whole sample expectedly includes peaks from spinel along with an average crystal orientation of all the gold nanoparticles. Pole figure in Figure 3.28a. which displays peaks only from a spinel sample is shown so that the similar peaks in Figure 3.28b can be identified as peaks from the substrate and not the AuNPs. All other peaks in Figure 3.28b can

then be contributed to the nanoparticles. For details on the orientations that produce all of the peaks, refer to [**1**]. Only the most important details will be discussed here. The brightest six outer peaks and the central peak are produced by the (111)-oriented spinel; AuNPs aligned in (111) orientation with spinel, and AuNPs aligned in (111) orientation with 60° in-plane rotation to spinel. The other bright peaks are produced majorly from nanoparticles with orientations of (115) and (113) with multiple in-plane orientations. As it can be seen, it is not possible to associate particular peaks to specific nanoparticles or to separate overlapping peaks of the substrate and nanoparticles.

The same sample is studied through EBSD as it is expected to provide a more detailed description of the orientation distribution. Multiple areas of the sample were studied, one of which is shown below in Figure 3.29. It includes 31 nanoparticles that produced high contrast automatically indexed EBSPs.

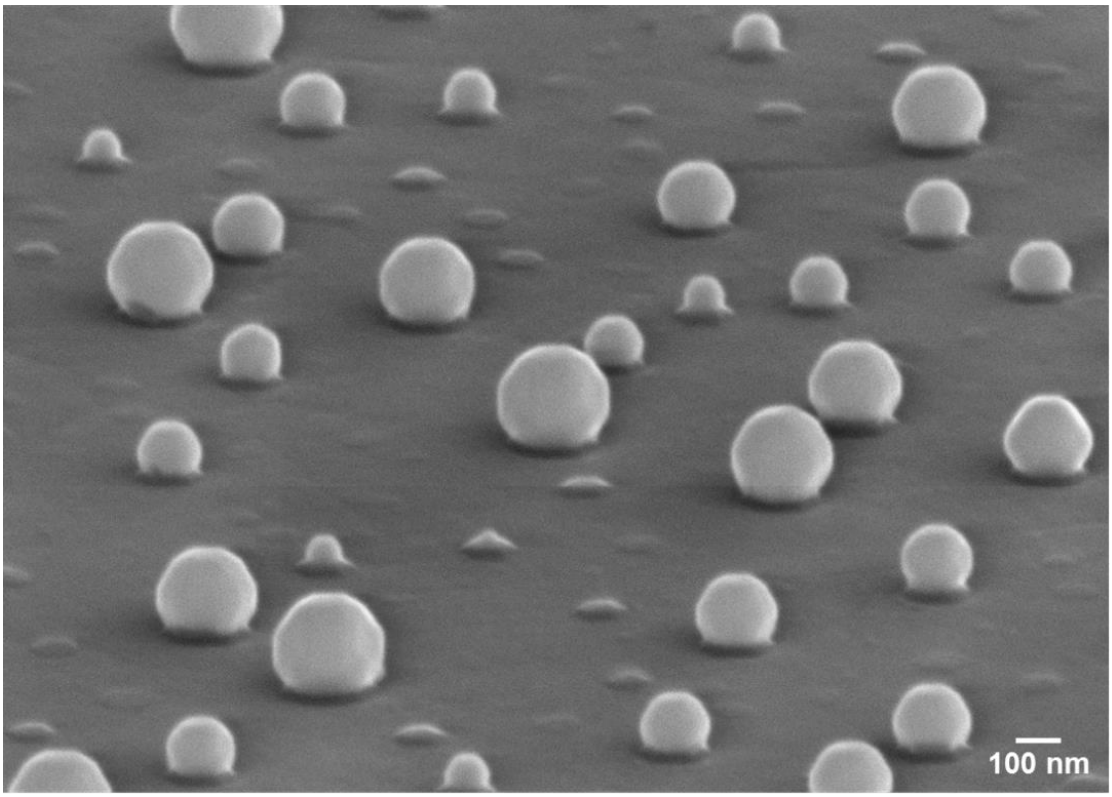

Figure 3.29: SEM image of an area Sample 1 at 70° tilt displaying the faceted spheres which produced the 2DXRD pole figures in Figure 3.28 and now, for comparison, its crystal structure will be investigated through EBSD.

The EBSD experiment is set up with beam at 15 keV and all other parameters chosen for fast measurements. Only one point per nanoparticle needed to be indexed as it was shown in Section 3.2.1 that AuNPs of this sample are single crystalline. From indexing results, in Figure 3.30, the orientation of each nanoparticle is labelled with a schematic showing the orientation of the unit cell. The green unit cell in the top right corner is a schematic displaying the (111) orientation of spinel. All the orientations in red are the nanoparticles that have the same (111) orientation as the substrate while those in orange also have the same (111) orientation but with a 60° in-plane rotation with respect to the substrate. The blue schematic represents the unit cell of (115) orientations rotated according to the in-plane rotations of the nanoparticle. Finally, the green cube represents the (113) orientation of the nanoparticles. These results are also potted on a pole figure for comparison with 2DXRD results.

The pole figure with 31 points is shown in Figure 3.31 and coloured according to the orientation of the nanoparticle. The red poles indicate the orientation of the 19 (111) nanoparticles, which is also the orientation of the substrate. The orange poles are from the nine (111)-oriented nanoparticles with 60° in-plane rotation. These set of points correspond with the six outer points of the pole figure from the 2DXRD analysis (Figure 3.28). Blue points show the two nanoparticles in the sample area that are (115)-oriented with one at 0° and the other with 60° in-plane rotation with respect to spinel. Finally the green poles indicate the orientation of one (113) nanoparticle present in the sample area.

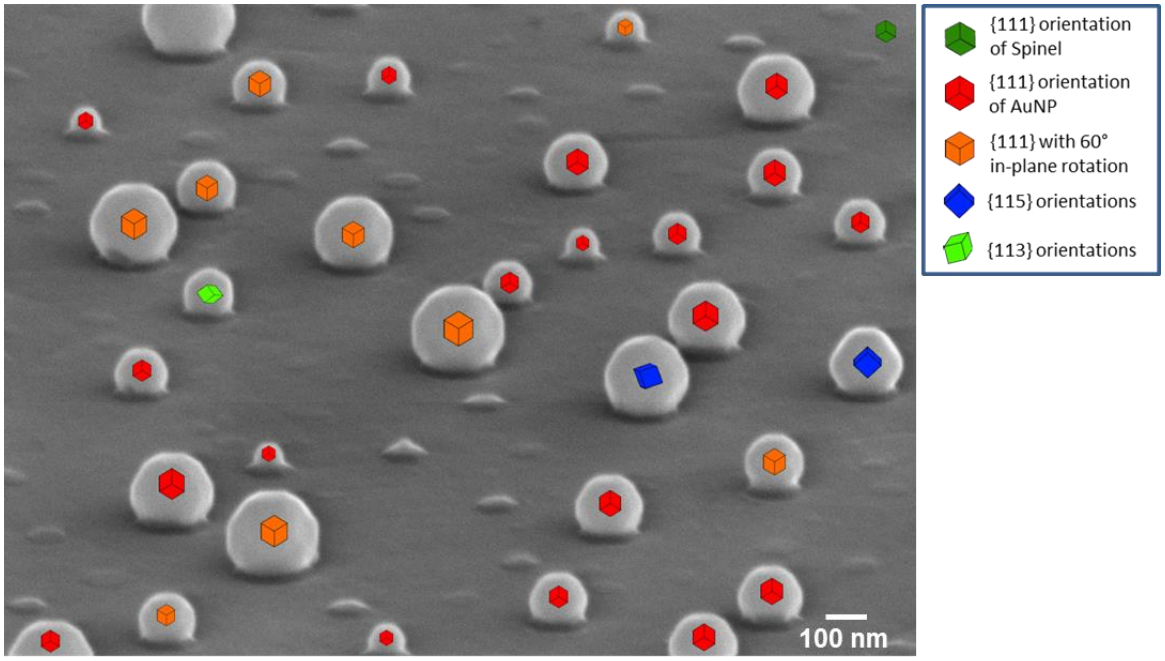

Figure 3.30: Orientation of AuNPs obtained from the EBSD analysis. The legend in the top right corner shows the orientations that each schematic represents, which are rotated according to the in-plane rotations with respect to the substrate

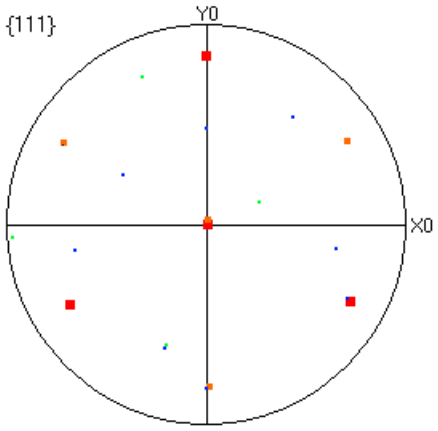

Figure 3.31: (111) pole figure obtained from the EBSD analysis of the nanoparticles shown in Figure 3.30. The poles are coloured according to the unit cell schematics in Figure 3.30.

Another area on the same sample is studied and the results, following the same convention as above, are shown in Figure 3.32.

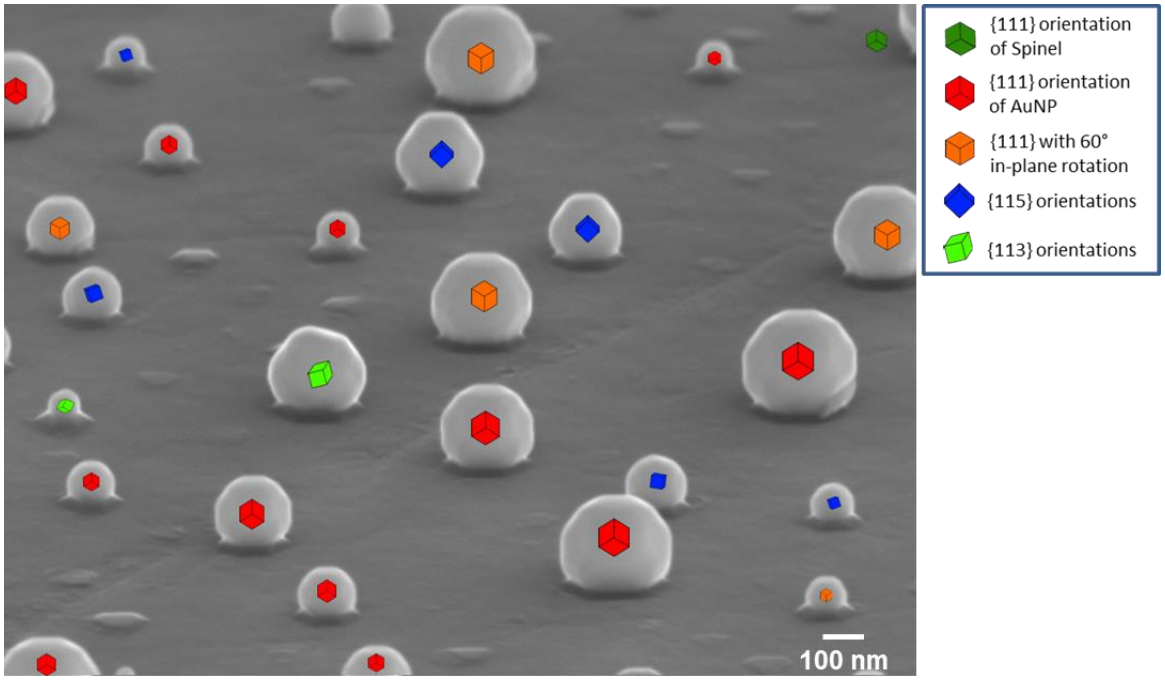

Figure 3.32: Another area of Sample 1 indexed through an EBSD experiment with the legend in the top right corner indicating the orientation each schematic represents.

This sample area is shown as it better depicts the presence of the (115) and (113) orientations. EBSD analysis in this fashion is repeated several times in different areas of the sample, another example of which is shown in Figure 3.33 and the data from 481 random nanoparticles in total is plotted in a pole figure and a contour pole figure in Figure 3.34.

As it can be seen, the contour pole figure in Figure 3.34b matches the peaks from the 2DXRD analysis in Figure 3.28b. The brightest peaks are the six outer peaks and the central peak corresponding to the (111)-oriented AuNPs and those with an orientation of (111) with 60° in-plane rotation. The other peaks mainly consist of (115) orientations and (113) orientations with several in-plane rotations. This comparison between the pole figure from 2DXRD and EBSD shows that not only can EBSD reproduce the results acquired from 2DXRD, but it also presents a huge advantage of being able link each peak and orientation to its respective nanoparticle. For example, from figures such as Figure 3.33, a relationship can be discovered between the orientation of a nanoparticle and its size or shape.

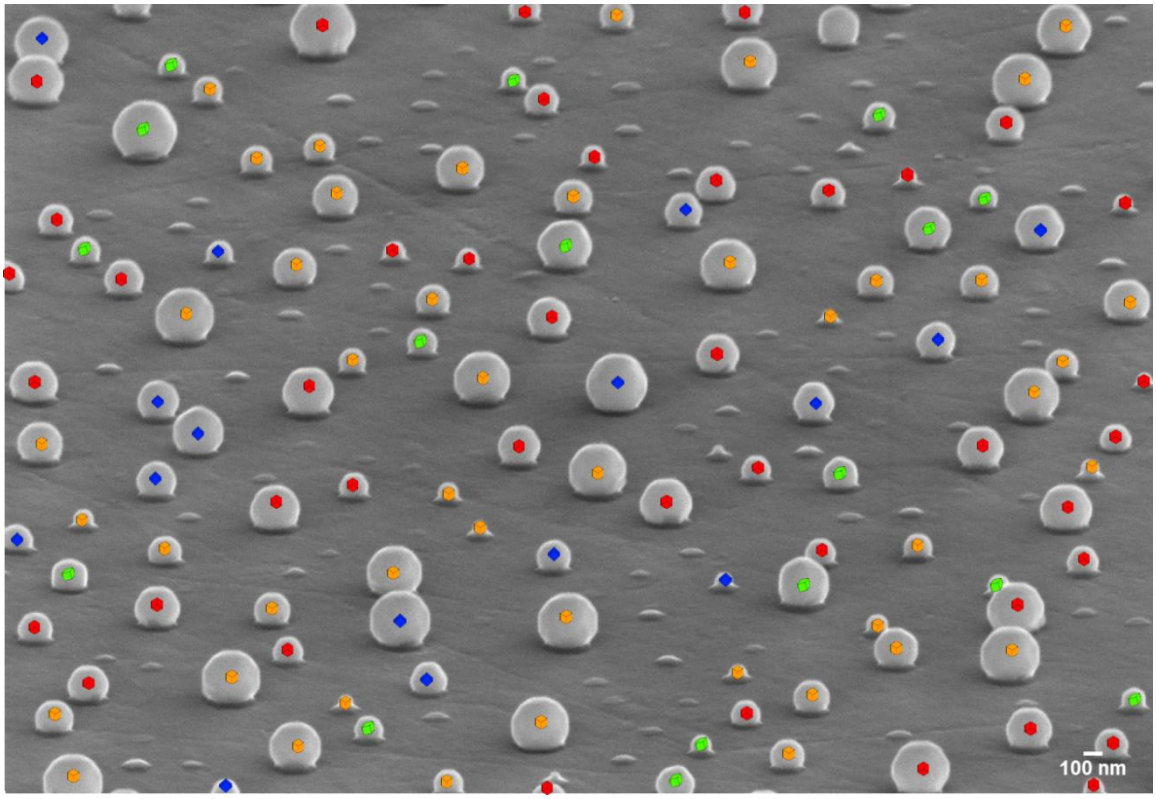

Figure 3.33: A large sample area is shown following the same convention for the schematics described in the legend of Figure 3.32. In this particular figure the unit cells of (115) and (113) are not rotated according to the in-plane rotations.

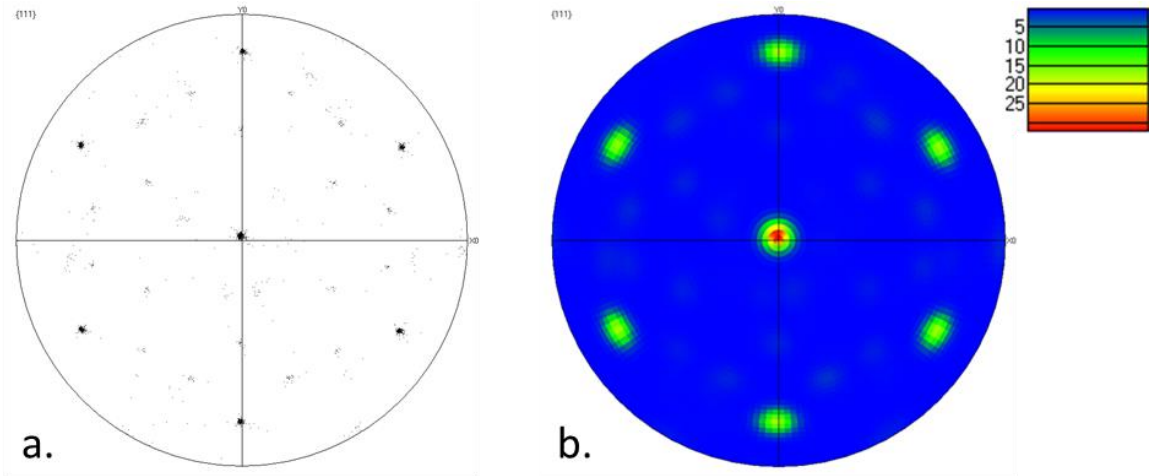

Figure 3.34: a) (111) pole figure and b) (111) contour pole figure displaying the preferred orientations from EBSD analysis of 481 nanoparticles from various areas of the sample

From semi-quantitative analysis of the 2DXRD (111) pole figure, Majdi [**1**] determined the percentage that each orientation contributes to the final (111) pole figure. These results are compared with the results acquired from 481 nanoparticles located in various parts of the sample. The results from both of the analyses are listed in Table 2. Although with EBSD all rotations of the orientations can be differentiated and analyzed separately, for comparison with 2DXRD data, all in-plane rotations are grouped together except for (111). For example, this sample contains (115)-oriented AuNPs with 0°, 60°, 120°, 180°, 240°, and 360° in-plane rotations, however, instead of calculating these individually, which is easily accomplished from the EBSD data, all the rotations are grouped and listed as (115) AuNPs.

Table 3: Percent crystal orientations of AuNPs acquired from semi-quantitative analysis of 2DXRD measurements [**1**] compared with those acquired from the EBSD analysis of 481 AuNPs

Orientation	**2DXRD** [**1**]	**EBSD**
<111> AuNP || <111> Spinel	49%	37% ± 3%
<111> AuNP || <111> Spinel 60° in-plane rotation	34%	36% ± 2%
<115> AuNP || <111> Spinel all in-plane rotations	12%	15% ± 4%
<113> AuNP || <111> Spinel all in-plane rotations (±10°)	5%	11% ± 3%
Others		2% ± 1%

In the 2DXRD analysis, orientations are determined from the intensity of the diffraction peaks through a semi-quantitative analysis. The possibility of errors, such as overlapping peaks is very high in a method such as this. With EBSD, on the other hand, due to the intrinsically greater resolution of the electron beam, the orientation of nanoparticles is determined individually and the pole figure is plotted from the resultant data. It can be seen in Table 3 that there are a few discrepancies amongst the two analyses. From the 2DXRD experiment, it is calculated that (111)-oriented AuNPs make up 49% of all the nanoparticles and (111) AuNPs with 60° in-plane rotations are 34% of all the nanoparticles. Whereas the EBSD analysis shows that in fact only 37% ± 3% of the nanoparticles are (111)-oriented and almost the same number have (111) orientation with 60° in-plane rotations. One of the reasons for the high percentage obtained for the (111) AuNPs from the 2DXRD analysis may be the fact that some of the peaks from (115)-

oriented AuNPs in fact overlap with (111) peaks on the pole figure. It may not be possible to differentiate between the two, resulting in an overestimation in the number of (111)-oriented AuNPs. Peaks from (113)-oriented nanoparticles also overlap other peaks in the pole figure and once again may be the reason for the disagreement amongst the number of nanoparticles that are in "other" orientations. The only cause of error in EBSD may be that only 481 nanoparticles are studied whereas 2DXRD covers the whole sample. This is however an unlikely cause of error as the nanoparticles are indexed from various areas of the sample and the error obtained from the standard deviation shows the percentages vary minimally from one area to another.

Another interesting sample that is studied in a similar method is the low temperature sample described in Section 2.1. This sample is prepared in the exact same method as the sample above; however, the annealing temperature is kept at only 650°C. From the SEM image of the sample below, it can be seen that this can be classified as an intermediate stage where the nanoparticles have drop like shapes instead of the well faceted spherical structures of the sample investigated earlier. For details on the concepts of dewetting and faceting, refer to [**1**,**15**].

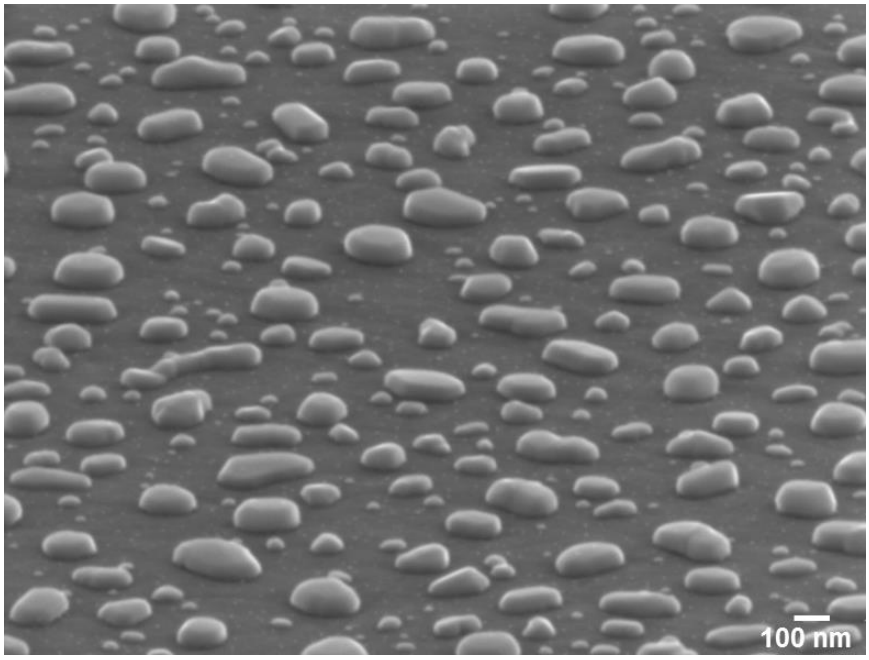

Figure 3.35: SEM image of an area of Sample 2 at 70° tilt displaying drop-like shapes of AuNPs resulting from the low annealing temperatures

Once again the pole figure from 2DXRD from Majdi's work [**1**] is compared with the results from EBSD. The pole figure from the substrate (Figure 3.36a) is presented yet again to show the peaks in the final pole figure (Figure 3.36b) that are present only due to the substrate. 2DXRD analysis shows that on average, the nanoparticles have a preferred orientation of (111) but with all the in-plane rotations. This is concluded from the broad outer ring of the pole figure in Figure 3.36b.

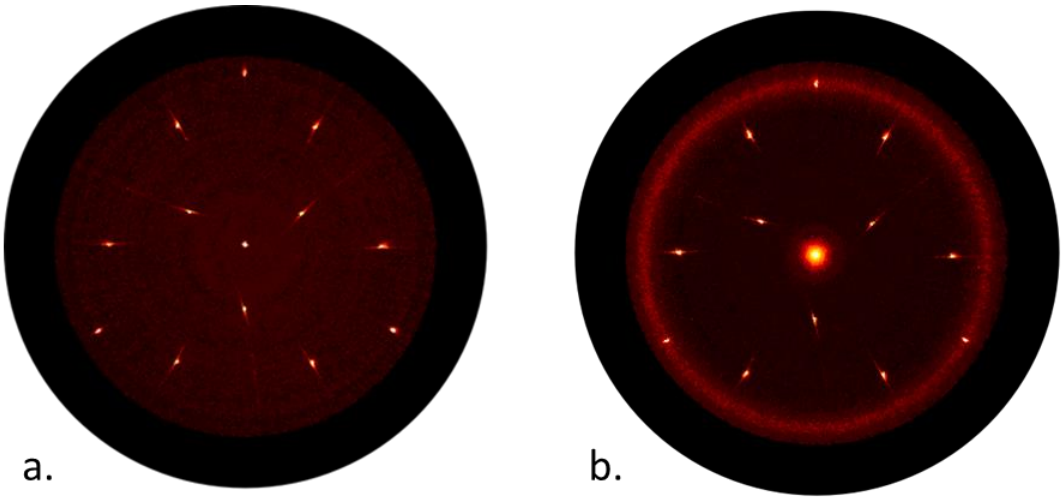

Figure 3.36: (111) pole figures from 2DXRD analysis of a) only Spinel and b) Sample 2 with drop-like shaped AuNPs overlapped with the poles from spinel [**1**]

EBSD experiment is once again performed with a 15 keV beam and all other parameters are adjusted to produce high contrast EBSPs in a short amount of time. It is observed during the experiment that AuNPs are once again single crystalline except when there is a well-defined change in the shape of the nanoparticle. In that case, two points are indexed; however, for most of the nanoparticles, one point is sufficient to determine its complete crystalline structure.

This result alone is very revealing when studying the nature of the growth process of these nanoparticles. From the fact that these drop-like shapes are single crystalline, the evolution of the crystal structure can be understood to a greater depth. Once the nanoparticles dewet, each one of the particles have their own defined crystal structure. That is, even in this early stage of growth, the particles have formed single crystalline particles, which is an interesting aspect that X-ray would not be able to reveal. 2DXRD analysis showed that the sample had a preferred orientation of (111) with all in-plane rotations according to the outer ring in Figure 3.36b. This could mean that the nanoparticles are either polycrystalline with multiple in-plane rotations of

the (111) orientation or that the nanoparticles are single crystalline but with varying in-plane rotations of the (111) orientation. Since X-ray is an averaging technique that would determine the overall orientation of the sample, it would not be able to differentiate between the two cases. However, EBSD results clearly show that the particles are not polycrystalline with (111) random in-plane orientations, however, individually the particles are single crystalline but each one of them have a random in-plane orientation.

In the schematic presented in Figure 3.37, the green cube in the top right corner displays the (111)-oriented spinel. The red unit cells, rotated in various directions, represent the (111)-oriented nanoparticles with varying in-plane rotations. The orange schematic represents the nanoparticles that are not exactly at (111) but with a misorientation angle of less than 10° from the (111) orientation. The orientation of the orange schematic is not related to any in-plane rotations. Finally the dark grey square represents all other orientations where the schematic does not signify any specific shape or rotation.

The data from 88 nanoparticles from various parts of the sample is once again plotted on a (111) pole figure and a (111) contour pole figure in Figure 3.38. The outer ring represents the nanoparticles that are (111)-oriented and it is broad due to the presence of nanoparticles that are (111)-oriented with misorientation angles of ± 10°.

Once again, EBSD analysis not only successfully reproduces the results from 2DXRD experiments, but it also provides details such as those present in Figure 3.37, where orientation of each nanoparticle is acquired individually. One advantage, for example, of studying a sample such as this with EBSD is due to its intermediate stage; it can be analyzed to determine how the growth process takes place. Particularly, with EBSD combined with SE images, shapes and crystal orientations can be linked and the process of how the crystal orientations change while the drop-like shapes transform into faceted spheres can be closely observed.

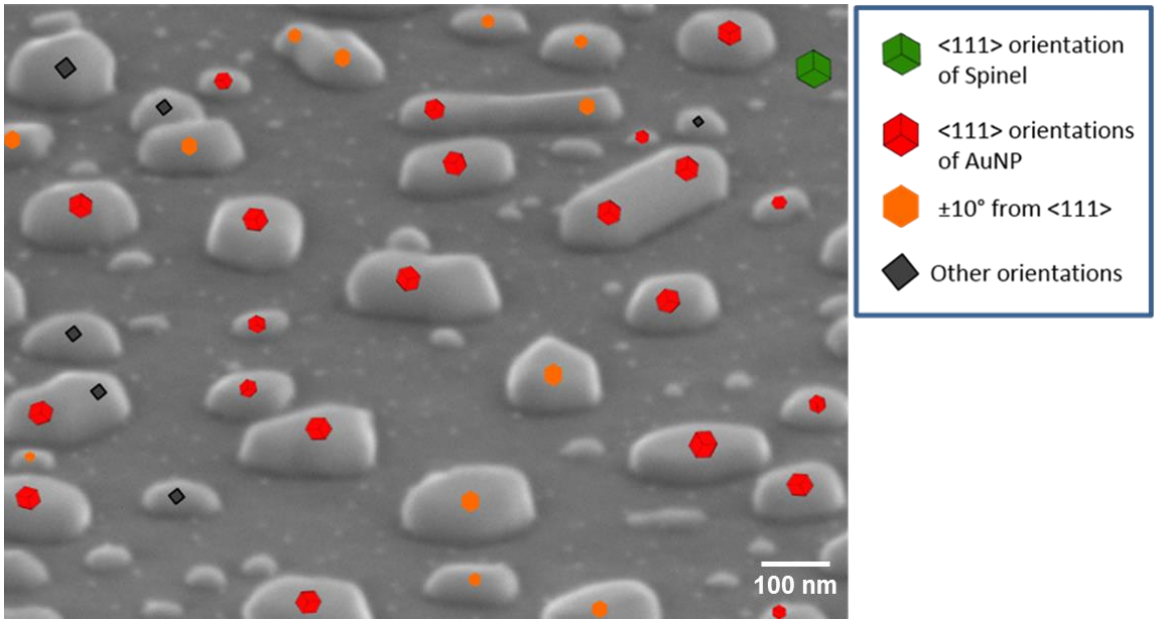

Figure 3.37: Orientation of AuNPs from the EBSD analysis. The legend in the top right corner shows the orientations that each schematic represents. The red unit cells are rotated according to the in-plane rotations with respect to the substrate

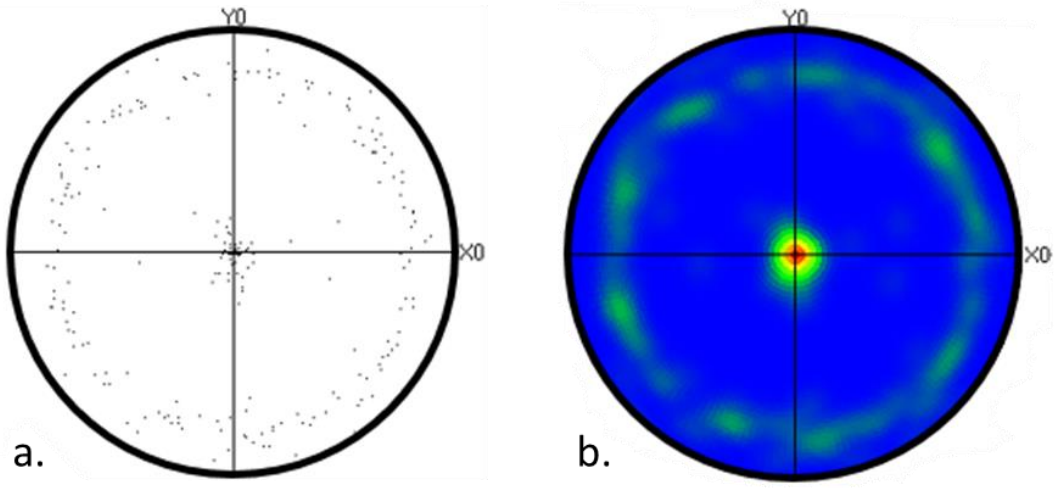

Figure 3.38: a) (111) pole figure and b) (111) contour pole figure displaying the preferred orientations from EBSD analysis of 88 nanoparticles from various areas of Sample 2

4. CONCLUSION

4.1 Summary

In the first set of experiments, an electron beam is scanned on one individual nanoparticle and the changes in the quality of the EBSP are observed. Varying the location of the beam in these experiments along with the Monte Carlo simulations reveal some of the mechanisms behind the intensity variations of EBSPs. First the beam was scanned from top to the bottom of the nanoparticle (y-direction) to observe the trends in intensity of EBSPs. Next, while keeping y constant, the beam probes from one side of the nanoparticle to the other (x-direction). This scan uncovers more details about the dependence of EBSP on the location of the beam. Finally all directions on a small nanoparticle are scanned and the EBSPs together provide a complete representation of the changing intensities. These experiments will eventually not only lead to determining the limitations of employing EBSD for studying nanostructures but may also provide a greater understanding of the EBSD technique itself.

Overall, from these scans of the nanoparticle, it was seen that the highest quality of EBSP was obtained when the beam was probing an area of the nanoparticle closest to the detector. Backscattered electrons are produced throughout the interaction volume and consequently diffraction occurs throughout this volume also. Since these diffracted electrons will undergo collisions with the atoms of the nanoparticle, typically only a percent of the electrons will escape. Generally, electrons that diffract near the surface will have a greater probability of escaping, while those deeper in the bulk of the material will lose all their energy through multiple scattering from atoms. However, if the dynamical theory of diffraction is applied, it is known that diffracted electrons, which propagate as Bloch waves through the sample, are attenuated at different rates. This means, that although majority of the diffracted signal will be from the interaction volume near the surface, it is also possible for electrons that have diffracted at greater depths to contribute to the signal.

From the three types of scans, the range of thickness of AuNP that produces a certain type of intensity on the EBSP was listed in Table 1 for 10 keV, 15 keV and 20 keV. Although these values are only an estimate obtained through visual comparison of EBSPs with the Monte Carlo simulation of a spherical nanoparticle, it provides a method to gain deeper understanding into the mechanisms of EBSD. In addition, it can be seen that the highest quality of EBSPs are obtained in the range of 10 nm to 30 nm for a gold nanoparticle with beam energy of 15 keV. Winkelmann [**28**] and Dingley [**50**] have also quoted similar values of thicknesses. Compared to the experiments performed by Winkelmann [**28**], Dingley [**50**], and Zaefferer [**36**], studying AuNPs provides a much simpler method of determining depth resolution. With flat samples, the beam has to penetrate a certain thickness which obviously cannot go beyond a certain thickness and thus patterns from greater depths cannot be observed. With AuNPs, or nanostructures in general, there is a possibility of positioning the beam such that many different thicknesses can be studied without having the limitation of the depth penetration of the beam. Current models would not predict the presence on a diffraction pattern from depths as great as 250 nm; however, it is apparent that in fact some contrast is still visible at such great depths. With this method, the depth dependence of Kikuchi patterns can be understood in more detail along with improvements in the models that simulate EBSPs.

The second set of experiments (Section 3.2) demonstrated how EBSD provides a simple and robust method to study the crystal structure of nanostructures. First, it was shown that the nanoparticles can be studied individually and it was determined that AuNPs are single crystalline by probing the surface of the nanoparticle from all sides. With this known, only one point on the nanoparticle is needed to be studied to determine the complete crystal structure of the nanoparticle. From the first set of experiments (Section 3.1), it was determined that the highest quality of EBSP was obtained when the beam was probing the top of the nanoparticle where a high number of diffracted backscattered electrons can escape the sample towards the detector. Thus to index each nanoparticle on the sample, one point near the top of each nanoparticle was indexed. The results from this experiment were presented through a schematic displaying the crystalline structure of each nanoparticle on a sample area (Figure 3.33) and through plotting the orientations in (111) pole figures. The pole figures were used to compare the results with the previous results obtained by Majdi [**1**] through 2DXRD measurements and an agreement was

seen amongst the pole figures. However, the added benefits of EBSD are shown in Figure 3.33 and Figure 3.37 where the crystalline structure of each nanoparticle can be seen individually. In addition, the overall distribution of the orientation, along with the size and shape of the nanoparticle can be observes through EBSD analysis of AuNPs.

In addition, a sample which was prepared at low annealing temperature was studied in a similar fashion through EBSD. It contained AuNPs that have dewet but have drop-like shapes rather than well-formed polyhedrons. Such a stage can be considered an intermediate stage and studying a sample in this stage reveals some of the processes taking place during the growth of the AuNP samples. Once again the results from this sample match the results from 2DXRD through comparison of pole figures. However, it cannot be determined through 2DXRD that these nanostructures are single crystalline, which is shown by EBSD. The most common orientation of the nanoparticles was found to be (111) with random in-plane rotations. This result shows that at some temperature after Au dewets, it forms drop-like shapes with (111) orientations and random in-plane rotations, but as the temperature is increased further, the nanoparticles lock into either (111) aligned with (111) direction of spinel or (111) with a 60° in-plane rotation with respect to spinel. This shows how EBSD opens up the door to the possibility of studying the evolution of crystal structure and understanding the growth processes of nanostructures in much greater detail.

4.2 Future Work

There are two fields that can benefit from the study of nanostructures through EBSD. One is of course the field of electron microscopy as this work presents a method which can be used to obtain a greater understanding of the intricacies of pattern formation in EBSD which are still not well known. The other field is the field of materials science where details of growth processes, shape and structure can be well understood in terms of the crystallographic nature of nanostructures. Some of the future research that can exist in both of these fields after this work is presented below.

4.2.1 Electron Backscatter Diffraction

There are two major areas in EBSD where there is room for growth. One is to have greater theoretical understanding of the processes which would open up the door to more applications of EBSD and second is an improvement in the EBSD equipment and software. Changes in intensity of EBSPs according to the depth of the source and contrast reversal are two areas discussed in this work that can lead to a deeper understanding of EBSD.

Depth Dependency of EBSPs: Determining the thickness in EBSD, or the depth where the diffraction pattern is produced is related to identifying the depth resolution in EBSD. As it was discussed in Section 3.1.4, the methods for determining the depth are all indirect and begin with certain assumptions. Change of incidence angle by Winkelmann [**28**], addition of amorphous layers by Zaefferer [**36**], and Dingley's [**50**] method of determining the thickness according to the line broadening in a Kikuchi pattern all contain certain set of assumptions – some which may be more accurate than others. With studying nanostructures, a new method is available for determining the effective thicknesses in EBSD. In fact, with a flat sample, the beam can only penetrate a certain depth and changing this depth can only be indirectly controlled by changing the angle of incidence. Even then, the penetration of the beam will reach a certain limit for flat bulk samples. However, with nanostructures, depth penetration is not a problem since the thickness is not only dependant on how deep the beam penetrates. Instead, the source point can be created at many different locations inside the nanoparticle depending on the position of the beam, and thus the changes in Kikuchi pattern according to the effective thickness can be studied in a much greater detail. This combined with Monte Carlo simulations to study the trajectories would lead to a greater understanding of the processes taking place at the atomic scale and quantification of these effects would lead to more accurate knowledge of the depth resolutions. The depths and consequent changes in EBSPs would eventually lead to better models of EBSD.

Contrast Reversal: Since the effective thickness can be varied as desired in nanostructures, contrast reversal can also be studied in much greater detail. Although it is a well understood concept in TEM [**12**], it has rarely been observed in EBSD [**10**] and thus the complexity of EBSP contrast reversal is not fully studied. In Section 3.1, it was observed that a reversed contrast

Kikuchi pattern is visible even beyond a thickness of 200 nm, which has not been reported elsewhere. In Winkelmann's model of EBSD [**28**], the highest depth which contributes a very small percent of the pattern is limited to 50 nm. In the context of that work, since greater depths contribute a very small percentage to the pattern, that is an adequate limiting thickness. However, it was observed from this work that Block wave 2 can travel great distances within a crystalline structure and also contain a wealth of information that has not yet been a subject of research. Thus, through studying nanostructures with EBSD, contrast reversal is another phenomenon that can be understood in greater deal which may also open up the door to more applications of EBSD.

EBSD equipment: Currently, the detectors are only mobile in one direction, which is the insertion direction towards the sample. The detectors are not able to move laterally (x and y directions of the EBSP). Although moving the detector back and forth changes its angular coverage, in some cases, moving it in the x- and y-direction will produce an optimal location for the detector to capture the greatest number of diffracted backscattered electrons. For example, for AuNPs from Section 3.1.2, it was observed that a high number of backscattered electrons are produced from a shallow depth (conditions required for a high quality EBSP in AuNPs) at some angles which may not be within the solid angle of the detector. This is especially apparent in the graphs in Figure 3.21 and Figure 3.22 which show that the solid angle of the detector (the region highlighted in yellow) is in fact not at the optimal location. It can be seen that when studying the right side of the nanoparticle (x = 115, shown by the blue curve), the highest amount of backscattered electrons with the smallest thickness are not produced in the current solid angle of the detector (130° to 230°, highlighted in yellow) but from 180° to 280°. Similarly, when the beam is probing the left side of the nanoparticle, the optimal location of the camera should be such that its solid angle is from 80° to 180°. Thus, a modification to the current setup of EBSD can include a detector that is mobile such that it can be positioned according to the locations where highest amount of signal is present.

EBSD software: The software that was used in this work was AZtec 2.4 (Oxford Instruments 2014). Although this software is currently one of the latest and very powerful, the work of AuNPs has shown the need for additional features. First of all, EBSD experiments of nanoparticles is only semi-automated, such that the user is required to select the position of the

beam on the sample while the rest of the indexing steps are automated. If it is known already that the nanostructures are single crystalline and that the highest quality of the pattern is achieved near the top end of the nanoparticle, the software can be modified such that it can detect the shapes of the nanoparticles from the contrast in the SEM images and automatically position the beam to probe the appropriate region of the nanoparticle followed by automated indexing. This addition to the software, where sampling points are selected automatically, would make the EBSD experiment on nanoparticles completely automated and comparable to experiments on flat samples.

Another excellent feature that can be added to the software is the ability to automatically create schematics like the ones shown in Figure 3.33 and Figure 3.37. Currently, the software outputs the three Euler angles describing the orientation of the nanoparticles, and to create the schematic such as the one in Figure 3.33, the user needs to convert those Euler angles into a diagram that represents the orientation of the unit cell described by the Euler angles, which are then superimposed on the SEM image of the nanoparticles. Thus, a feature is the post-processing steps can be programmed such that the software automatically generates a schematic, such as that of a cube, and rotate it according to the Euler angle orientation given by automated indexing. This rotated cube can be assigned according to the point where the beam was positioned to obtain the EBSP and then superimposed automatically onto the SEM image of the sample. Both of these additions would allow both the EBSD experiments and post-processing steps to be completely automated and allow for a lot more experiments on nanostructures to be undertaken. Large samples can be studied in a short amount of time and with minimum inputs from the user. Such additional features would make studying nanostructures comparable to the ease of studying flat samples through EBSD.

A final additional feature that needs to be added to the current EBSD software is the ability to automatically detect reversed contrast Kikuchi bands. Currently, the software is not programmed to detect dark deficit bands as they are not commonly observed in EBSD experiments. However, it is seen that if the beam is positioned near the bottom of the nanoparticle where source of the diffraction pattern is created deep inside the material, a reversed contrast EBSP is always observed. Even though the pattern does not have a high signal, it contains information related to the crystal structure of the source point. Currently, since the

bands are visible to the naked eye, the user manually selects the band edges for the computer to then index the pattern. However, the program should automatically be able to detect the bands based on the contrast differences.

4.2.2 Nanostructures

Crystal structure of nanostructures is typically studied with TEM or through X-ray diffraction. Studying nanostructures through EBSD opens up the possibility to a whole new method that can be used to study many different types of nanostructures on top of the substrate and throughout the growth process. The technique can not only be used towards studying nanostructures individually but can also be used to study the orientation distribution of large samples. In this work, it was shown how EBSD can be used to study AuNPs however, further research can take place to determine the relationship between the crystal orientation and shape and size of nanoparticles. Growth conditions can be varied and the change in preferred orientation can be studied easily also. Finally, EBSD can be combined with energy dispersive X-ray spectroscopy (EDS) to identify not only the crystal structure but also the phase and composition of the nanostructures.

In addition, it was observed in Section 3.1.3 that when a spherical model of AuNP is used, the 3D graphs in Figure 3.26 of the depth of the source have curved transition areas. It would be interesting to simulate nanoparticles with polyhedron shapes and studying the transitions in the range of depth. Since the contrast is related to the depth of the source, it may be possible to extract the shape of a nanoparticle directly from the variation in contrast of an EBSP.

Finally, any crystalline sample that is stable in SEM and does not readily oxidize (creating an amorphous layer) can be studied through EBSD. For nanostructures, it is also important that the nanostructures are not too densely packed such that a direct path between the beam and the detector is present and not blocked by other particles as described in Section 3.1. If these simple conditions are met, for example, this technique can be used to study nanowires and the growth direction of the nanowires can be acquired very easily. Additionally, other factors such as changes in EBSP according to the Z number, density, and size of nanostructures can be studied in detail. Other than the brief study by Small et al. [**13**,**14**] in 2001 and 2002, since this is one of the

first works that explores some of the uses and limitations of EBSD of nanostructures, this opens up the door to much further research into the technique itself, models of EBSD and the its applications on nanostructures.

REFERENCES

[1] T. Majdi, "Novel Self-assembly of Crystalline MgAl2O4 Nanostructures Promoted by Annealing a Gold Overlayer on a (111) MgAl2O4 Substrate," McMaster University, 2013.

[2] V. Jarvis, J. F. Britten, and R. R. LaPierre, "Texture analysis of GaAs nanowires," *Semiconductor Science and Technology*, vol. 26, no. 2, 2011.

[3] M. Kirkham, X. Wang, Z. L. Wang, and R. L. Snyder, "Solid Au nanoparticles as a catalyst for growing aligned ZnO nanowires: a new understanding of the vapour–liquid–solid process," *Nanotechnology*, vol. 18, 2007.

[4] A. M. M. a. C. M. Lieber, "A Laser Ablation Method for the Synthesis of Crystalline Semiconductor Nanowires," *Science*, vol. 279, pp. 208-211, 1998.

[5] S. Wang, S. Yang, Z. R. Daib, and Z. L. Wang, "The crystal structure and growth direction of nanowire arrays Cu2S fabricated on a copper surface," *Physical Chemistry Chemical Physics*, vol. 3, no. 17, pp. 3750-3753, 2001.

[6] K. S. Cho, D. V. Talapin, W. Gaschler, and C. B. Murray, "Designing PbSe Nanowires and Nanorings through Oriented Attachment of Nanoparticles," *Journal of the American Chemical Society*, vol. 127, no. 19, p. 7140–7147, 2005.

[7] M. E. Messing, K. A. Dick, L. R. Wallenberg, and K. Deppert, "Generation of size-selected gold nanoparticles by spark discharge - for growth of epitaxial nanowires," *Gold Bulletin*, vol. 20, no. 1, pp. 20-26, 2009.

[8] C. P. Li, et al., "Growth Direction and Cross-Sectional Study of Silicon Nanowires," *Advanced Materials*, vol. 15, no. 7-8, pp. 607-609, 2003.

[9] X. D. a. C. M. Lieber, "Laser-assisted catalytic growth of single crystal GaN nanowires," *Journal of the American Chemical Society*, vol. 122, pp. 188-189, 2000.

[10] A. Schwartz, M. Kumar, B. Adams, and D. Field, *Electron Backscatter Diffraction in Materials*,

2nd ed. New York: Springer, 2000.

[11] J. Cocle, "Development of the EBSD Intensity Response for Quantitative Strain Analyses of Materials," Master's Thesis, McGill University, Montreal, 2008.

[12] D. B. Williams and C. B. Carter, *Transmission Electron Microscopy: A Textbook for Materials Science*. New York: Springer, 2009.

[13] J. A. Small and J. R. Michael, "Phase identification of individual crystalline particles by electron backscatter diffraction," *Journal of Microscopy*, vol. 201, no. 1, pp. 59-69, 2001.

[14] J. A. Small, J. R. Michael, and D. S. Bright*, "Improving the quality of electron backscatter diffraction (EBSD) patterns from nanoparticles," *Journal of Microscopy*, vol. 206, no. 2, pp. 170-178, 2002.

[15] G. Devenyi, "An Investigation into the Role of Energy and Symmetry at Epitaxial Interfaces," Ph.D. Thesis, McMaster University, Hamilton, 2013.

[16] R. S. Wagner and W. C. Ellis, "The Vapor-Liquid-Solid Mechanism of Crystal Growth and its Application to Silicon," *Applied Physics Letters*, vol. 4, no. 5, pp. 89-90, 1964.

[17] L. Reimer, *Scanning Electron Microscopy: Physics of Image Formation and Microanalysis*. Berlin, Heidelberg, New York: Springer, 1998.

[18] M. von Laue, W. Friedrich, and P. Knipping, "Interferenzerscheinungen bei Röntgenstrahlen," *Annalen der Physik*, vol. 346, no. 10, pp. 971-988, 1912.

[19] M. von Laue, "Kritische Bemerkungen zu den Deutungen der Photoframme von Friedrich und Knipping," *Physikalische Zeitschrift*, vol. 14, no. 10, pp. 421-423, 1913.

[20] W. Bragg and W. Bragg, "The Reflection of X-rays by Crystals," *Proceedings of the Royal Society of London*, vol. 88, no. 605, p. 428–438, 1913.

[21] P. B. Hirsch, A. Howie, R. B. Nicholson, D. W. Pashley, and M. J. Whelan, *Electron Microscopy of Thin Crystals*. Malabar, Florida: Rebert E. Krieger , 1977.

[22] E. M. Schulson, "Electron channelling patterns in scanning electron microscopy," *Journal of Materials Science*, vol. 12, pp. 1071-1087, 1977.

[23] B. Fultz and J. Howe, *Transmission Electron Microscopy and Diffractometry of Materials*. Berlin, Heidelberg, New York: Springer, 2012.

[24] L. Reimer and H. Kohl, *Transmission Electron Microscopy: Physics of Image Formation*, 5th ed. New York: Springer-Verlag , 2008.

[25] C. J. Humphreys, "The scattering of fast electrons by crystals," *Reports on Progress in Physics*, vol. 42, pp. 1825-1887, 1979.

[26] J. C. H. Spence and J. M. Zuo, *Electron Microdiffraction*. New York: Plenum Press, 1992.

[27] H. A. Bethe, "Theorie der Beugung von Elektronen an Kristallen," *Annalen der Physik*, vol. 392, no. 17, pp. 55-129, 1928.

[28] A. Winkelmann, "Principles of depth-resolved Kikuchi pattern simulation for electron backscatter diffraction," *Journal of Microscopy*, vol. 239, no. 1, pp. 32-45, 2010.

[29] F. Bloch, "Über die Quantenmechanik der Elektronen in Kristallgittern," *Zeitschrift für Physik* , vol. 52, no. 7-8, pp. 555-600, 1928.

[30] A. Winkelmann, C. Trager-Cowan, F. Sweeney, A. P. Day, and P. Parbrook, "Many-beam dynamical simulation of electron backscatter differaction patterns," *Ultramicroscopy*, vol. 107, pp. 414-421, 2007.

[31] S. Kikuchi, "Diffraction of Cathode Rays by Mica," *Japanese Journal of Physics* , vol. 5, p. 83–96, 1928.

[32] L. M. Peng, S. L. Dudarev, and M. J. Whelan, *High Energy Electron Diffraction and Microscopy*. New York: Oxford University Press, 2004.

[33] J. M. Cowley, *Diffraction Physics*, 3rd ed. North-Holland, Amsterdam: Elsevier Science, 1995.

[34] A. P. Pogany and P. S. Turner, "Reciprocity in electron diffraction and microscopy," *Acta Crystallographica*, vol. 24, pp. 103-109, 1968.

[35] D. C. Joy, "Channeling in and channeling out: The ongms of electron backscattering and electron channeling contrast," *Proceedings of EMSA*, pp. 592-593, 1994.

[36] S. Zaefferer, "On the formation mechanisms, spatial resolution and intensity of backscatter Kikuchi patterns," *Ultramicroscopy*, vol. 107, p. 254–266, 2007.

[37] A. Winkelmann and G. Nolze, "Analysis of Kikuchi band contrast reversal in electron backscatter diffraction patterns of silicon," *Ultramicroscopy*, vol. 110, pp. 190-194, 2010.

[38] M. N. Alam, M. Blackman, and D. W. Pashley, "High-Angle Kikuchi Patterns," *Proceedings Royal Society London* , vol. 471, no. 2176, pp. 224-242, 1954.

[39] L. Sawyer, D. Grubb, and G. Meyers, *Polymer Microscopy*, 3rd ed. New York: Springer, 2008.

[40] "SEM Q&A," JEOL Ltd.

[41] "Reference Manual and 3D-EBSD," HKL Technology, 2004.

[42] "Channel 5," HKL Technology Manual, 2006.

[43] S. Sitzman, "Introduction to EBSD analysis of micro- to nanoscale microstructures in metals and ceramics," *SPIE proceedings*, vol. 5392, pp. 78-90, 2004.

[44] D. Carpenter, J. Pugh, G. Richardson, and L. Mooney, "Determination of pattern centre in EBSD using the moving-screen technique," *Journal of Microscopy*, vol. 227, no. 3, pp. 246-247, 2007.

[45] O. Engler and V. Randle, *Introduction to Texture Analysis: Macrotexture, Microtexture, and Orientation Mapping*, 2nd ed. Amsterdam: CRC Press, 2009.

[46] N. C. Krieger Lassen, D. Juul Jensen, and K. Conradsen, "Image processing procedures for analysis of electron back scattering patterns," *Scanning Microscopy*, vol. 6, pp. 115-121, 1992.

[47] K. Ratter, "Surface Preparation for Electron Backscatter Diffraction Investigation using Low Energy Argon and High Energy Focused Gallium Ion Beams," Master's Thesis, EÖTVÖS LORÁND UNIVERSITY, 2012.

[48] A. Kamp, "Investigation of Titanium a Plates by EBSD Analysis," Master's Thesis, Delft University of Technology , 2007.

[49] S. L. Dudarev, P. Rex, and M. J. Whelan, "Theory of Electron Backscattering from Crytals," *Physical Review B*, vol. 51, no. 6, pp. 3397-3412, 1995.

[50] D. Dingley, "Progressive steps in the development of electron backscatter diffraction and orientation imaging microscopy," *Journal of Microscopy*, vol. 213, no. 3, p. 214–224, 2004.

[51] S. A. Speakman, "Basics of X-ray Diffraction - Self-User Training for the X-Ray Diffraction ," MIT.